DNA electrophoresis in microfabricated devices

Kevin D. Dorfman*

Department of Chemical Engineering and Materials Science, University of Minnesota–Twin Cities, Minneapolis, Minnesota 55455, USA

(Published 6 October 2010)

Picking up at the conclusion of Viovy's review of the physics of gel electrophoresis [J.-L. Viovy, Rev. Mod. Phys. **72**, 813 (2000)], this review synthesizes the experimental data, theoretical models, and simulation results for DNA electrophoresis in microfabricated and nanofabricated devices appearing since the seminal paper by Volkmuth and Austin [Nature (London) **358**, 600 (1992)]. Prototype versions of these devices separate DNA by molecular weight at a rate far superior to gel electrophoresis. After providing an overview of the requisite background material in polymer physics, electrophoresis, and microfluidic device fabrication, the focus is on the following three generic problems: (i) collision with an isolated post, (ii) transport in an array of posts, and (iii) entropic trapping and filtration in the slit-well motif. The transport phenomena are examined here in the context of the length and time scales characterizing the DNA, the device, and the applied electric field.

DOI: 10.1103/RevModPhys.82.2903 PACS number(s): 87.15.Tt

CONTENTS

*dorfman@umn.edu

I. INTRODUCTION

Electrophoretically separating DNA by size is unquestionably one of the most important tools in the molecular biology toolbox. Indeed, the term "DNA electrophoresis" is often synonymous with "DNA separation." Unfortunately, early free-solution electrophoresis experiments by Olivera *et al.* (1964) established that the free-solution electrophoretic mobility of a nucleic acid is independent of its molecular weight. As a result, agarose

and polyacrylamide gels are commonly used to separate DNA by size, a process known as gel electrophoresis. Double-stranded DNA up to several tens of thousands of base pairs (bp) can be resolved in a manner of hours using a steady dc electric field in the range of 0.1–10 V/cm and an easily handled 1% agarose gel. Agarose gels tend to have pore sizes in the range of 200–500 nm, although the exact value is controversial (Viovy, 2000). Polyacrylamide gels, with their smaller 5–100 nm pores (Viovy, 2000), are often used to separate the more flexible single-stranded DNA.

For many years, the biology community was stymied by the inability to resolve chromosome-size DNA by gel electrophoresis because the electrophoretic mobility in agarose becomes independent of size above a critical molecular weight. This critical size depends on the electric field and the gel concentration; for example, a size-dependent electrophoretic mobility persists up to at least 750 kilobase pairs (kbp) in dilute agarose gels (Fangman, 1978; Serwer, 1981). For the gels normally used in the laboratory, the upper limit is around 20 000 base pairs. In what follows, DNA that exceeds this limit and thus cannot easily be separated under a steady dc field in an agarose gel will be called "long DNA." Separating long DNA is important for a number of applications, such as sizing chromosomes and DNA fingerprinting.

The introduction of pulsed-field gel electrophoresis by Schwartz and Cantor (1984) and subsequent landmark advances in the technique (Carle *et al.*, 1986; Chu *et al.*, 1986; Clark *et al.*, 1988) raised the resolving power of gel electrophoresis into the megabase pair range, allowing the direct sizing of chromosomes. In pulsed-field gel electrophoresis, the electric field periodically alternates between two directions. The separation arises from the size-dependent time for the DNA to reorient in the new electric field. Today, long DNA is separated by size over the course of approximately one day using commercial pulsed-field gel electrophoresis devices.

What was the role of physics in this story? Although experiments such as those by Flint and Harrington (1972) established the loss of resolution for high molecular weights, it took the extension of the biased-reptation model of Lerman and Frisch (1982) by Lumpkin and Zimm (1982) to explain the origin of the loss of resolution at high molecular weights, namely, the orientation of the reptating chain in the field direction. The development of pulsed-field gel electrophoresis built upon these physical principles. Indeed, Schwartz and Cantor (1984) directly referred to fundamental observations on the relaxation of DNA in solution by Klotz and Zimm (1972) as a possible mechanism underlying separations by pulsed-field gel electrophoresis. The complexity of the various modes of pulsed-field electrophoresis and the surprising experimental result thus obtained, in particular for field-inversion gel electrophoresis (Carle *et al.*, 1986), led to an onslaught of theories and simulation approaches from the physics community (Deutsch, 1987; Lalande *et al.*, 1987; Southern *et al.*, 1987; Viovy, 1987, 1988, 1989; Zimm, 1988, 1991; Deutsch and Madden, 1989; Noolandi *et al.*, 1989; Slater and Noolandi, 1989; Duke, 1990; Duke and Viovy, 1992a).

Our goal is not to discuss gel electrophoresis at length; this topic was reviewed comprehensively by Viovy (2000). Rather, we devote our time to considering the physics underpinning the bevy of experimental systems introduced since the maturation of pulsed-field gel electrophoresis. A notable development during this time was the infusion of microfabricated devices into academic research in analytical chemistry along with the hope that miniaturized systems would eventually replace their macroscopic counterparts, such as gel electrophoresis. The earliest "lab-on-a-chip" systems focused on capillary electrophoresis of small charged molecules (Manz *et al.*, 1992). Later research moved onto the challenging problem of separating long DNA and led to a host of new devices, such as post arrays (Volkmuth and Austin, 1992) and entropic traps (Han and Craighead, 2000), which form the subject of this review. As we will see, the story of physics in pulsed-field gel electrophoresis was repeated in the context of microfabricated devices—new separation methods predicated on physical principles produced sometimes surprising experimental results, piquing the interest of theoreticians and leading to intense modeling efforts and further experimental studies.

Although the engineering of DNA electrophoresis has had an enormous impact, for example, in the completion of the human genome project (Davies, 2001), it remains unclear whether microfluidic devices will ever achieve the practical utility of their macroscopic counterparts (Mukhopadhyay, 2009). That being said, it is clear that these new devices constitute an excellent platform for studying basic problems in polyelectrolyte electrophoresis and polymer physics in general. The precision of microfabrication allows for perfectly periodic pore geometries that contrast strongly with the disordered pore spaces in gels. Likewise, the micrometer-scale features in microfabricated systems are ideally suited for manipulating long DNA. Apart from these geometrical advantages, experiments in microfabricated systems benefit from commercially available bright intercalating dyes for DNA and sensitive cameras. As a result, numerous laboratories routinely observe the dynamics of long DNA by videomicroscopy at the single-molecule level. These same experimental systems can provide ensemble-averaged data by injecting a plug of DNA into the device, taking advantage of electrokinetic injection methods developed for on-chip capillary electrophoresis (Jacobson *et al.*, 1994) and then measuring the fluorescence intensity at fixed points in space or time. Thus, virtually all of the experimental data required to understand DNA electrophoresis in microfabricated devices are available, at least in principle, in well-defined microstructures that are amenable to theoretical modeling.

Our aim here is to synthesize the experimental, computational, and theoretical studies of DNA electrophoresis that appeared since the seminal paper on electrophoresis in microfabricated post arrays by Volkmuth and Austin (1992). We commence in Sec. II with a dis-

cussion of the structural and electrostatic properties of DNA, its free-solution electrophoresis, biased-reptation theory, and microfabrication. These sections are by no means comprehensive and pertinent references are provided in context. Rather, they provide a foundation for the subsequent discussion of electrophoresis in microfabricated systems. After completing our tour of the relevant background information, we begin the core elements of the review by first sorting microfabricated separation devices into one of two generic architectures: (i) a post array or (ii) a slit-well motif. We consider the post systems first, building upon our knowledge of the collision with an isolated post in Sec. III to understand the dynamics of DNA in obstacle arrays in Sec. IV. The slit-well motif is discussed in Sec. V, where the pertinent length scales give rise to behavior ranging from entropic trapping to filtration. Our exposition concludes in Sec. VI with some perspectives on the likely subjects of the next review of DNA electrophoresis. As this is a maturing field, we also discuss its transition from a topic in physics to one in engineering.

II. BACKGROUND

A. Properties of DNA—Without the matrix

1. Characteristic length scales

Double-stranded DNA is a semiflexible polymer whose structure is characterized by a cascade of length scales. The structural biology of DNA is remarkably complex; readers interested in a detailed discussion should see Calladine and Drew (1997) and Bloomfield *et al.* (2000). In what follows, we restrict our attention to B-form DNA, the most common double-helical structure. For the moment, we also limit our spatial resolution to the length scale characterizing the spacing between the bases, $l_{\mathrm{bp}}=0.34$ nm. DNA viewed at this length scale is a heteropolymer consisting of four monomers, the bases adenine, guanine, thymine, and cytosine, connected by phosphodiester bonds. The bases are located inside the helix and thus screened from the external chemical environment. This static structure is not completely accurate as thermal motion, the action of enzymes, or mispaired bases lead to the formation of "bubbles" in the backbone.

DNA is an acid and adopts a negative charge in aqueous solution due the dissociation of H^+ from the phosphate backbone. As a first approximation, the total charge of the DNA would be $2eN_{\mathrm{bp}}$, where e is the charge of an electron and N_{bp} is the number of base pairs. However, Manning (1969) showed that this leads to a singularity when the charges on the backbone interact very strongly. He proposed that counterions "condense" back onto the chain such that the effective charge spacing along the chain l_c is equal to the length scale over which the electrostatic energy between two like charges is equal to thermal energy. These condensed counterions can be H^+ or any other cation in the solution, such as Na^+. The effective charge spacing is equal to the Bjerrum length,

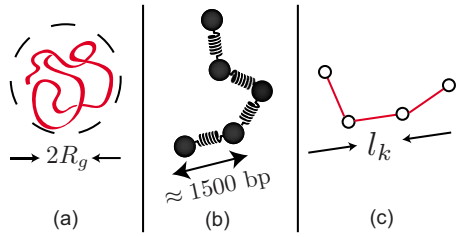

FIG. 1. (Color online) Coarse-grained picture of DNA in free solution. Depending on the length scale of interest, we treat the DNA as (a) a coil of radius of gyration R_g at the largest scale, (b) a collection of beads connected by springs at intermediate scales, or (c) a connection of N_k rigid segments of Kuhn length $l_k \approx 300$ bp at the smallest scale. In order for the bead-spring description to be valid, each bead-spring pair must consist of a number of Kuhn segments.

$$l_B = \frac{e^2}{4\pi\epsilon_0\epsilon_b k_B T}, \tag{1}$$

where ϵ_0 is the permittivity of free space, ϵ_b is the bulk permittivity of the medium, and k_BT is the Boltzmann factor. This phenomenon, known as Manning condensation, leads to the effective charge of double-stranded DNA being considerably less than would be expected if all of the phosphate groups dissociated completely. For example, the saturated charge fraction of DNA in aqueous Na^+ is 0.24 (Manning, 1978).

While an understanding of DNA at the nucleotide level is critical for many biophysical studies, we can capture much of the physics underlying DNA electrophoresis using the simpler models shown in Fig. 1. Rather than model the chain as hundreds (or thousands) of bases, we adopt a coarser approach and treat the chain instead as a homopolymer consisting of N_k Kuhn segments of Kuhn length l_k. For the remainder of this review, we focus exclusively on this homopolymer model, neglecting any effects of sequence. If the DNA is confined to a length scale smaller than the Kuhn length, then a finer-scale model is needed (Odijk, 1983, 2008).

The stiffness of the chain is captured by the persistence length $l_p=l_k/2$, which characterizes the decay of correlations in the tangent vector to the backbone of the chain due to thermal energy (Doi and Edwards, 1988). DNA electrophoresis (and virtually all biology) occurs in ionic solutions. As a result, the apparent persistence length l_p consists of two contributions,

$$l_p = l_{p'} + l_{\mathrm{OSF}}. \tag{2}$$

The first term $l_{p'}$ is the intrinsic persistence length arising from correlations in the backbone vector caused by steric hindrances to rotation around bonds and bending the bonds. The second term l_{OSF} is the so-called Odijk-

TABLE I. Properties of λ-DNA. The various physical parameters are discussed in Sec. II.

Property	Symbol	Value	Reference
Number of base pairs	N_{bp}	48 502	New England Biolabs
Persistence length	l_p	53 nm	(Bustamante *et al.*, 1994; Smith *et al.*, 1992)
Radius of gyration	R_g	0.73 μm	(Smith *et al.*, 1996)
Diffusion coefficient	D	0.47 $\mu m^2/s$	(Smith *et al.*, 1996)
Electrophoretic mobility[a]	μ_0	1.8×10^{-4} $cm^2/V\,s$	(Ou *et al.*, 2009; Randall and Doyle, 2006)

[a]The electrophoretic mobility corresponds to a polydimethylsiloxane (PDMS) channel and tris-borate-EDTA (TBE) 2.2× buffer with 0.07 wt% polyvinylpyrrolidone (PVP). Other materials, buffers, and additives will affect the free-solution mobility.

Skolnick-Fixman (OSF) length (Odijk, 1977; Skolnick and Fixman, 1977),[1]

$$l_{OSF} = \frac{l_B}{4\kappa^2 l_c^2}. \tag{3}$$

The OSF length is an additional contribution to the persistence length arising from electrostatic repulsion by the charges on the backbone of the chain. The screening length for electrostatic interactions in a salt solution is the Debye length,

$$\kappa^{-1} = \sqrt{\frac{\epsilon_0 \epsilon_b k_B T}{2e^2 I}}, \tag{4}$$

where

$$I = \frac{1}{2}\sum_i z_i^2 c_i \tag{5}$$

is the ionic strength of a medium containing a concentration c_i of species with valence z_i.

As a result of electrostatic interactions, the persistence length of DNA can be tuned by changing the salt concentration (Baumann *et al.*, 1997). In typical electrophoresis buffers, the Debye length is between 1 and 10 nm (Viovy, 2000). When modeling DNA electrophoresis, the persistence length is often taken as 53 nm, a value obtained from fitting the force extension curve for DNA in 5 mM Na_2HPO_3 (Smith *et al.*, 1992) to a wormlike chain model (Bustamante *et al.*, 1994). With the latter choice, the standard coarse-grained DNA model consists of approximately 300 bp per Kuhn segment.

With the exception of a discussion of DNA nanofilters in Sec. V.B, we will generally be concerned with long DNA. As we noted in Sec. I, a practical definition of "long" DNA is DNA that cannot be separated easily by size using dc gel electrophoresis. While we will be more precise about this point in Sec. II.B, a good rule of thumb is that long DNA is at least several tens of kilobase pairs in size.

Owing to its ready availability, λ-phage DNA (48.5 kbp) is the canonical example of long DNA and the species we encounter most frequently in our review of the literature. The physical and electrophoretic properties of λ-DNA have been studied extensively. These properties are summarized in Table I along with representative references. Note that the diffusion coefficient and radius of gyration of other sized DNA molecules can be estimated using the experimental data for λ-DNA and the scaling laws in this section. The other large DNA that we encounter frequently is T4-DNA (169 kbp), which serves as a convenient standard for high molecular-weight experiments.

In free solution, the configurational entropy of the chain is maximized by the random coil configuration shown in Fig. 1(a). The DNA we consider here is generally long enough so that excluded volume interactions are important, whereupon the radius of gyration of the coil scales as

$$R_g \sim l_k N_k^{\nu}, \tag{6}$$

where ν is the Flory exponent (Doi, 1996). For a swollen chain in a good solvent, $\nu=3/5$, while an ideal chain (no excluded volume interactions) has the exponent $\nu=1/2$. The radius of gyration of λ-DNA, extracted from single-molecule diffusion measurements, is 0.73 μm (Smith *et al.*, 1996). The latter experiments also obtained a scaling exponent $\nu=0.611\pm0.016$, demonstrating good solvent scaling.

Before we move on to the dynamic properties of DNA, we conclude this section with some practical remarks about the role of intercalating dyes on the structure of DNA. In most of the experiments reviewed here, the DNA is dyed with an intercalating molecule such as YOYO or TOTO (Rye *et al.*, 1992). The fluorescence enhancement of these dyes ranges from 460 to 1400 (Gurrieri *et al.*, 1997), providing sufficient intensity to visualize single DNA molecules at video frame rates via fluorescence microscopy. These dyes also bind DNA very strongly, with binding constants of size $10^8 M^{-1}$

[1]The calculation leading to Eq. (3) assumes that the bonds are not allowed to rotate. With rotation the scaling becomes $l_{OSF} \sim \kappa^{-1}$ (Dobrynin, 2005).

(Gurrieri *et al.*, 1997; Gunther *et al.*, 2010). While visualization is one of the key tools used to understand DNA electrophoresis, it is important to keep in mind that the dye itself causes significant changes in the molecule. Importantly, intercalating dyes increase the contour length. Visualization experiments report an increase by a factor of close to 30% (Perkins *et al.*, 1995; Bakajin *et al.*, 1998; Randall and Doyle, 2005a). For λ-DNA, this implies that the contour length increases from its bare value of 16.5 to 20–21 μm upon binding with TOTO-1 (Randall and Doyle, 2005a). Systematic magnetic tweezer experiments indicate that the intercalation of YOYO-1 elongates DNA by a factor of 1.6±0.4 bp/dye molecule up to a saturation limit of 0.31 dye molecules per base pair, leading to an elongation of 47±2% at saturation. The intercalation may also change the persistence length of DNA, although this remains controversial (Sischka *et al.*, 2005; Gunther *et al.*, 2010) and could depend on the ionic strength of the solution. One also needs to be careful in the quantity of dye and DNA used in a given experiment (Zhu *et al.*, 1994). In our experience, deleterious concentration effects are easily recognized by smeared bands in the electropherograms and DNA aggregates in the videomicroscopy, analogous to what has been observed in capillary electrophoresis (Mitnik *et al.*, 1995).

2. Free solution electrophoresis

A natural question to ask is why we need a sieving medium in the first place. The answer lies in the physics governing the free-solution electrophoresis of long DNA. We begin here with the so-called "local force" model, which is frequently invoked in the DNA electrophoresis literature. The scaling produced by the local force model [Eq. (12)] agrees with experiments, at least for long DNA. However, the model itself has a number of problems, which are discussed in Sec. II.A.3.

In the local force model, the electrical force acting on the DNA molecule is

$$F_{\text{elec}} = q_k N_k E, \tag{7}$$

where q_k is the charge per Kuhn segment and E is the magnitude of the electric field. Recall that, as a result of Manning condensation, the charge per Kuhn segment is not the same as would be expected if all of the phosphate groups had lost a proton, $q_k \neq 2el_k/l_{\text{bp}}$. Volkmuth *et al.* (1994) used free-solution mobility data for single DNA molecules to obtain an effective charge of 0.3 electron/Å. This value for the effective charge is not consistent with Manning condensation (Volkmuth *et al.*, 1994) but leads to the correct free-solution mobility when the friction of the chain is equivalent to a connected series of noninteracting rods. The electrical force is opposed by a friction force

$$F_{\text{fric}} = -v\xi_c, \tag{8}$$

where v and ξ_c are the velocity and friction coefficient of the chain. Balancing these two forces, we find that

$$v = \mu_0 E, \tag{9}$$

where μ_0 is the free-solution electrophoretic mobility of the DNA,

$$\mu_0 = \frac{q_k N_k}{\xi_c}. \tag{10}$$

In order to evaluate μ_0, we need to know the friction coefficient ξ_c, which in general depends on the interactions between the segments of the chain as they move through the fluid. In contrast to hydrodynamic interactions, electrostatic interactions are often assumed to decay exponentially fast over the Debye length κ^{-1} (Manning, 1981); the r_{ij}^{-1} decay arising from hydrodynamic interactions is replaced by $e^{-\kappa r_{ij}}$. Inasmuch as a typical Debye length is a few nanometers and a typical Kuhn length is 100 nm, the electrophoretic motion of one segment of the chain would not influence the motion if its neighbors. Long and Ajdari (2001) called into question this commonly held assumption about the screening length. Using a Green's function analysis, they found that the hydrodynamic interactions actually decay as $1/r^3$, where r is the distance from a point force. One only arrives at an exponential decay after averaging over all orientations for an isotropically distributed particle (Long and Ajdari, 2001).

Regardless of the details of the hydrodynamic interactions for DNA, which remain a subject of debate, experiments (Olivera *et al.*, 1964; Nkodo *et al.*, 2001; Stellwagen *et al.*, 2003) definitely showed that DNA electrophoresis is effectively "freely draining"—in a hydrodynamic sense, the fluid appears to penetrate the coil and interact with each segment in the chain. As pointed out by Manning (1981), the electrostatic interactions leading to the electrophoretic mobility are screened on the Debye length κ^{-1}. Since $\kappa l_k \gg 1$, the electrostatic interactions between different Kuhn segments are small. The resulting friction coefficient, valid for DNA containing many Kuhn segments, is

$$\xi_c^{\text{Rouse}} = N_k \xi_k. \tag{11}$$

The latter friction coefficient, equivalent to that appearing in the Rouse model of polymer dynamics (Rouse, 1953), is the sum of the friction ξ_k arising from each of the N_k Kuhn segments. Using the Rouse friction in Eq. (10) reveals that the free-solution mobility is independent of size for long DNA,

$$\mu_0 \sim N_k^0. \tag{12}$$

A more detailed analysis (Manning, 1981) reveals that the electrostatic interactions make a logarithmic contribution, $\mu_0 \sim \ln(\kappa l_k)$.

While we have focused thus far on long DNA (with an eye toward the devices to be discussed shortly), it is worthwhile to note that the free-solution mobility of short DNA is a function of molecular weight (Stellwagen *et al.*, 1997; Stellwagen and Stellwagen, 2002). The experimental data of Stellwagen *et al.* (1997), reproduced in Fig. 2, indicate that the free-solution mobility is

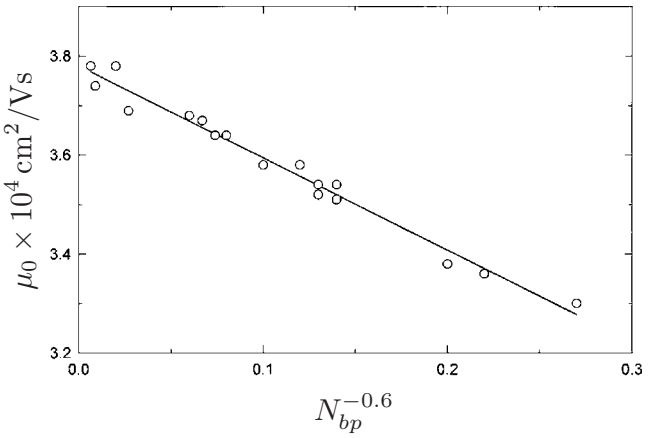

FIG. 2. Free solution velocity as a function of $N_{\mathrm{bp}}^{-0.6}$, where N_{bp} is the number of base pairs. Adapted from Stellwagen *et al.*, 1997.

well captured by the scaling law $\mu_0 \sim N_{\mathrm{bp}}^{-0.6}$. The crossover to the scaling $\mu_0 \sim N_{\mathrm{bp}}^{0}$ occurs around 400 base pairs (Stellwagen *et al.*, 1997, 2003).

Reported values of the electrophoretic mobility are often the combination of a contribution due to the electrophoretic motion and an additional electro-osmotic velocity arising from the ζ potential of the surface of the capillary or microchannel (Russell *et al.*, 1989),

$$\mu_{\mathrm{eof}} = \frac{\epsilon_0 \epsilon_b \zeta}{\eta}. \tag{13}$$

The ζ potential is a function of both the chemical properties of the surface and the solvent conditions (Kirby and Hasselbrink, 2004a, 2004b). Thus, we find a range of reported free-solution mobilities depending on the experimental apparatus and the buffer. For example, zone electrophoresis (Olivera *et al.*, 1964) and capillary electrophoresis (Stellwagen *et al.*, 1997) experiments using the common tris base, boric acid, and ethylenediaminetetraacetic acid (TBE) buffer both found $\mu_0 = 4.5 \times 10^{-4}$ cm^2/V s. Similar experiments in polydimethylsiloxane (PDMS) microchannels reported lower mobilities of 1.8×10^{-4} cm^2/V s (Randall and Doyle, 2006; Ou *et al.*, 2009) presumably due a change in electro-osmosis.

While the electro-osmotic component of the mobility can be measured in a separate experiment to isolate the electrophoretic component μ_{ele} (Stellwagen *et al.*, 1997), in most cases we are interested in the net velocity of the DNA, which includes both electro-osmotic and electrophoretic components. Provided that the electro-osmosis is uniform (implying a constant ζ potential on the surface), then simply adding the two mobilities is an acceptable and useful approach. The full set of assumptions underlying this approximation is outlined in the context of the so-called similitude condition for electro-osmotic flow (Cummings *et al.*, 2000). Thus, when we refer to the free-solution mobility μ_0 for an experiment, we generally mean

$$\mu_0 = \mu_{\mathrm{ele}} + \mu_{\mathrm{eof}}. \tag{14}$$

This additive approach is incorrect when the ζ potential of the surface is not constant. Even for the simple model of a point defect in the surface ζ potential, the ensuing recirculating flow needs to be included in any analysis (Long *et al.*, 1999). From a separation standpoint, recirculating flows often lead to catastrophic band broadening. These deleterious flows can be eliminated using a channel with a uniform surface ζ potential, most often through the use of surface modifications.

3. Criticism of the local force model

The local force model that leads to Eq. (12) is frequently invoked in the DNA electrophoresis literature. In particular, the bead-spring Brownian dynamics simulation models that we encounter later in this review all use the local force model. These simulations require integrating a stochastic ordinary differential equation for the forces acting on each of the beads (Deutsch, 1988). The electric force is a local force, and the charge per bead is adjusted to furnish the desired electrophoretic mobility.

While the local force model is attractive at first glance, the electric field does not simply exert a force on the DNA. Rather, the electric field exerts a force on both the DNA and the counterions in the double layer proximate to the DNA, leading to relative motion between the DNA and the fluid. Indeed, the entire concept of phoretic motion is that there is no net force (or torque) acting on the particle (Anderson, 1989).

The standard analysis of the electrophoresis of colloidal particles takes a boundary-layer approach that, in contrast to the local force picture, correctly accounts for the action of the electric field on both the particle and its double layer through the introduction of an effective slip velocity at the surface of the particle. In the thin Debye layer limit, the particle surface is effectively flat with respect to the Debye layer and the local slip velocity is given by the Smoluchowski result (Anderson, 1989),

$$\mathbf{v}_{\mathrm{slip}} = \frac{\epsilon_0 \epsilon_b \zeta}{\eta} \mathbf{E}_t, \tag{15}$$

where $\mathbf{E}_t$ is the tangential electric field vector at the surface of the particle. The similarity between Eq. (15) and the electro-osmotic mobility in Eq. (13) is not a coincidence; they represent the same phenomenon but use a different frame of reference. Once the slip velocity at each point on the particle surface is known, the bulk fluid flow is computed from the Navier-Stokes equations and the electrophoretic velocity is obtained by enforcing zero net force on the system consisting of the particle and its double layer (Anderson, 1989). This fluid-mechanical approach has yielded a number of nontrivial results. For example, a particle possessing a constant ζ potential and thin Debye layer in a macroscopic electric field E moves with the electrophoretic velocity

$$v = \frac{\epsilon_0 \epsilon_b \zeta}{\eta} E, \tag{16}$$

independent of the particle size or shape (Morrison, 1970). Moreover, if a number of such particles are separated by a distance larger than the Debye layer, they do not interact (Anderson, 1989). The derivation of the latter results is certainly aided by the fact that colloidal particles are treated as rigid materials.

While most of the DNA electrophoresis literature uses the local force picture, there is one important exception that will play a role in our later discussion. Long *et al.* (1996) noted that the free-draining behavior of polyelectrolyte electrophoresis, embodied in Eq. (12), is not valid under the simultaneous action of electric and nonelectric forces. While the electric field acts on both the DNA and the counterions in the Debye layer, the nonelectric forces only act on the DNA. We frequently encounter such nonelectric forces, for example, during the collision with a post, and take advantage of this so-called electrohydrodynamic equivalence principle (Long *et al.*, 1996) in our analysis. For applications of the electrohydrodynamic equivalence principle to gel electrophoresis, consult the review by Viovy (2000).

While the local force model has some obvious problems, it does appear to capture a number of experimental data on DNA electrophoresis. This agreement may be a fortuitous combination of (i) hydrodynamic screening in gels (Viovy, 2000), which should also be the case in the small slits that we will see here (Bakajin *et al.*, 1998; Chen *et al.*, 2004) and (ii) the frequent use of scaling laws that neglect numerical prefactors (Viovy, 2000). Moreover, Brownian dynamics simulations based on the local force picture compare favorably with experiments on DNA electrophoresis in microfabricated devices (Kim and Doyle, 2007; Ou *et al.*, 2009). We note that more sophisticated simulation methods that incorporate counterion electrostatics are required to capture the length dependence of Fig. 2 (Frank and Winkler, 2009; Grass and Holm, 2010). With the continued development of mesoscale solvent models (Slater *et al.*, 2009) and the persistent increase in computational power, the shortcomings of local force picture of DNA electrophoresis will hopefully become more apparent in the coming years.

4. Diffusion

For transport driven by hydrodynamics (such as occurs in pressure-driven flow or molecular diffusion), the interactions decay as r_{ij}^{-1}, where r_{ij} is the distance between segment i and $j \neq i$. Such long-ranged interactions lead to the so-called Zimm friction (Zimm, 1956),

$$\xi_c^{\text{Zimm}} \sim \eta R_g. \tag{17}$$

In other words, the friction of a chain of radius R_g is equivalent to a rigid spherical particle of the same radius. The fluid inside the chain is trapped and the coil thus appears impermeable to the external fluid, a phenomenon which is well illustrated by molecular-

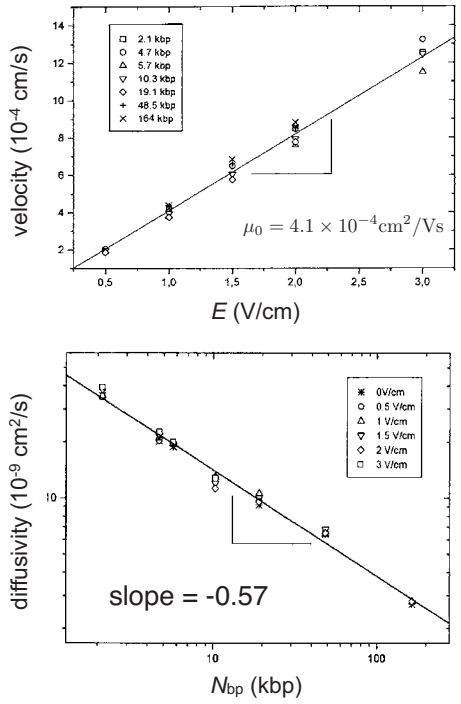

FIG. 3. Experimental measurements of the free-solution electrophoresis of DNA during capillary electrophoresis. (Top) Free solution velocity as a function of the electric field for different sized DNA. (Bottom) Diffusion coefficient as a function of DNA length for different electric fields. From Nkodo *et al.*, 2001.

dynamics simulations (Kenward and Slater, 2004). The Zimm friction correctly predicts the scaling for the diffusivity of long DNA in both single-molecule measurements (Smith *et al.*, 1996) and during free-solution electrophoresis (Nkodo *et al.*, 2001),

$$D \approx \frac{k_B T}{\eta R_g} \sim N_k^{-\nu}. \tag{18}$$

Indeed, measuring the diffusion coefficient is a standard method to infer the radius of gyration of the chain [see, for example, Smith *et al.* (1996)].

Comparing Eqs. (18) and (12), it is apparent that no Stokes-Einstein exists between the electrophoretic mobility and molecular diffusivity (Nkodo *et al.*, 2001; Stellwagen *et al.*, 2003). Molecular diffusion arises from *hydrodynamic* interactions with the solvent and obeys the fluctuation-dissipation theorem. In contrast, the electrophoretic mobility arises from *electrostatic* interactions with the applied electric field. Indeed, the molecular-weight dependencies of μ_0 and D lie at the heart of the ratchet separations of DNA that we will encounter in Sec. IV.B.1 (Duke and Austin, 1998; Ertas, 1998; Chou *et al.*, 1999; Huang, Silberzan, *et al.*, 2002; Huang *et al.*, 2003).

To clarify this point, Fig. 3 reproduces data obtained by Nkodo *et al.* (2001) for the velocity and diffusion coefficient of a wide range of DNA during free-solution capillary electrophoresis. These experiments were performed under relatively weak electric fields where the

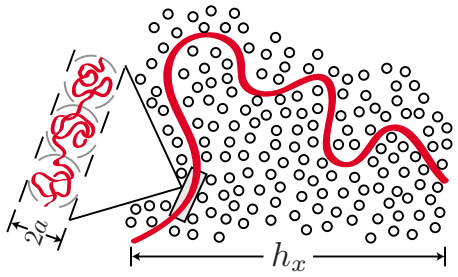

FIG. 4. (Color online) Schematic illustration of biased reptation during gel electrophoresis of DNA. The gel fibers confine the DNA of contour length $\mathcal{L}$ to a tube of radius a and length L_{tube}. The projection of this tube in the direction of the electric field is h_x. The blowup shows the blobs of DNA present in the shaded region of the chain. Each blob contains $(a/l_k)^2$ Kuhn segments.

diffusion is sensible over the experimental time scale. The velocity is independent of N_k and increases linearly with the electric field, consistent with Eq. (12). Likewise, the scaling exponent for the diffusion coefficient during electrophoresis, $\nu=-0.57$, is consistent with Eq. (18) in a good solvent and quite close to that cited earlier from single-molecule measurements (Smith *et al.*, 1996). Stellwagen *et al.* (2003) obtained similar scaling results, summarizing their data by the relationship

$$\mu_0 = cN_{\text{bp}}^{\nu} D, \tag{19}$$

where $c=40\pm2$ V^{-1} is an empirically determined constant.

We conclude this section by recalling that the absence of a Stokes-Einstein equation is well known in the colloid electrophoresis literature. As noted above, the electrophoretic velocity of the particle is proportional to the ζ potential, independent of particle size or shape (Morrison, 1970). In contrast, the diffusivity of a colloidal particle depends on both its size and its shape. The contrast between electrophoresis and diffusion is most striking for asymmetric colloidal particles since the electrophoretic mobility is a scalar while the diffusivity is a tensor.

B. Why is it hard to separate long DNA in a gel?

1. Biased reptation

Although DNA cannot be separated in general in free solution, it is possible to separate the DNA in a gel via the biased-reptation mechanism shown in Fig. 4. The basic principle of biased reptation is remarkably simple—the seminal publications by Lerman and Frisch (1982) and Lumpkin and Zimm (1982) each contains only two pages of text. As shown in Fig. 4, a DNA of contour length $\mathcal{L}=N_k l_k$ is modeled as a succession of blobs whose radii are equal to the pore radius, a. The gel is modeled by steric interactions that confine the DNA motion to a tube, analogous to the reptation model of de Gennes (1971) for diffusion of a chain in a polymer melt. In order for the chain to remain in the tube, the electric field needs to be weak enough so that the reduced electric field is small (Slater, 2009),

$$\frac{q_k E a^3}{2k_B T l_k^2} < 1. \tag{20}$$

While this is the criteria appearing in early publications on biased reptation, its form (Viovy, 2000) and validity (Semenov and Joanny, 1997) have been called into question.

Assuming that the portion of the DNA molecule inside a pore forms a Gaussian chain therein, then each pore contains $(a/l_k)^2$ Kuhn segments and the length of the tube containing this "chain of blobs" is less than the contour length, $L_{\text{tube}}=\mathcal{L}(l_k/a)$. At some point in time, imagine that the chain of blobs adopts a conformation characterized by a projection h_x in the direction of the electric field. The electrical force acting on this chain of blobs,

$$F_{\text{elec}} = \frac{q_k E h_x}{l_k}, \tag{21}$$

is opposed by a frictional force,

$$F_{\text{fric}} \approx -\eta \mathcal{L} v_{\text{tube}}, \tag{22}$$

where v_{tube} is the curvilinear velocity of the DNA inside the tube formed by the pores of the gel. The frictional force in Eq. (22) is linear in molecular weight from the freely draining approximation. With Eqs. (10) and (11), the resulting curvilinear velocity in the tube is

$$v_{\text{tube}} = \frac{\mu_0 E h_x}{\mathcal{L}}. \tag{23}$$

Upon escaping from the tube, the DNA will have moved a distance h_x downfield and formed a new tube. The net velocity is thus

$$v = \frac{\Delta x}{\Delta t} = \frac{h_x}{L_{\text{tube}}/v_{\text{tube}}} = \mu_0 E\left(\frac{h_x^2}{\mathcal{L}L_{\text{tube}}}\right). \tag{24}$$

After moving through many tubes, the effective mobility of the chain μ is the average over the mobility through each individual tube,

$$\frac{\mu}{\mu_0} = \left\langle \frac{h_x^2}{\mathcal{L}L_{\text{tube}}} \right\rangle. \tag{25}$$

The latter result, which is somewhat different from the standard result $\mu/\mu_0=\langle h_x^2/\mathcal{L}^2\rangle$, was derived by Zimm (1991) and appropriate for the relatively loose confinement in an agarose gel. If the chain of blobs itself forms a random walk in the gel, then $\langle h_x^2\rangle \approx aL_{\text{tube}}$ and the mobility is a function of molecular weight, $\mu\sim N_k^{-1}$. Conversely, if the chain is oriented in the electric field, then $h_x \approx L_{\text{tube}}$ and the mobility is independent of molecular weight, $\mu\sim N_k^0$.

While we only needed a few lines of math to obtain these basic scaling laws, considerably more work went into developing the complete theory of biased reptation

appearing in the reviews by Viovy (2000) and Slater (2009). The initial work by Lumpkin *et al.* (1985), Slater and Noolandi (1985a, 1985b, 1986), and Slater *et al.* (1987) fleshed out the implications of the original biased-reptation models, most notably the prediction that

$$\mu \sim N_k^0 E^2 \tag{26}$$

when the DNA is oriented in the direction of the electric field. One of the most interesting results to come out of these models (and subsequent experiments) is the existence of a mobility minimum caused by backward motion in the tube, which can lead to self-trapping of the chain in a long-lived relatively immobile state (Noolandi *et al.*, 1987; Doi *et al.*, 1988; Lalande *et al.*, 1988). These U- and J-shaped states are qualitatively similar to those occurring in microfabricated systems (see Fig. 10).

In evaluating the potential to separate DNA by gel electrophoresis, it is important to determine the crossover point N_k^* between the oriented and unoriented regimes. The original biased-reptation model result in Eq. (26) predicts that $N_k^* \sim E^{-2}$. Unfortunately, this prediction turns out to be incorrect due to fluctuations of the end of the chain. A modified version of the model, known as biased reptation with fluctuations (Duke *et al.*, 1992, 1994; Semenov *et al.*, 1995), predicts that the mobility in the oriented regime scales as

$$\mu \sim N_k^0 E, \tag{27}$$

leading to a crossover at $N_k^* \sim E^{-1}$. This model, spurred by prior simulation data by Duke and Viovy (1992b), agrees remarkably well with experimental data in agarose gels (Heller *et al.*, 1994).

The scaling for the crossover regime has dire implications for separating long DNA by dc gel electrophoresis—as the size of the DNA increases, the electric field needs to decrease in order to retain a size-dependent mobility. Alternatively, the gel concentration can be reduced (Fangman, 1978; Serwer, 1981) to increase the pore radius a and thus reduce the number of blobs. As shown in Fig. 5, λ-DNA only remains in the unoriented regime up to 0.1 V/cm, with a corresponding velocity of around 1 mm/week. As a result, it is hardly practical to separate large DNA by dc gel electrophoresis, especially when we also take into account the band broadening due to molecular diffusion during such a lengthy experiment.

2. Pulsed field gel electrophoresis

Long DNA can be separated in a gel by periodically changing the direction of the electric field, a method known as pulsed-field electrophoresis (Schwartz and Cantor, 1984; Carle *et al.*, 1986; Chu *et al.*, 1986; Clark *et al.*, 1988). The literature on pulsed-field electrophoresis is vast and thoroughly reviewed by Viovy (2000). At a qualitative level, we can understand both the power and the shortcomings of pulsed-field electrophoresis by considering the orientation of the DNA. At the end of a particular pulse of the electric field, all of the DNA will be oriented in the direction of the electric field. According to the biased-reptation theory, these oriented DNA will all move at the same velocity. When the direction of the electric field changes, the DNA needs to reorient itself with the new electric field direction. The reorientation time is a function of molecular weight; if we resort to the simplest model of turning the corner (Southern *et al.*, 1987), it is clear that a longer DNA will take more time to reorient than its shorter counterpart. After reorientation, the DNA will move again with a size-independent velocity until the direction of the electric field changes once more. While the mobility in pulsed-field electrophoresis is a function of molecular weight, the separation is generally very slow. Not only is the reorientation time long, but there is minimal center-of-mass motion in the direction of the average electric field during reorientation. As a result, a typical pulsed-field separation requires hours to days. This motivated the development of most of the methods discussed in this review.

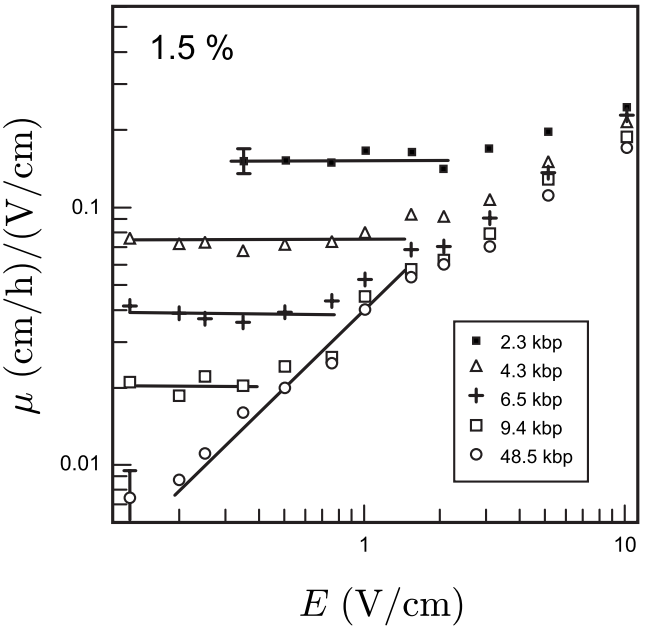

FIG. 5. Electrophoretic mobility of different sized DNA in a 1.5% agarose gel as a function of the electric field. From Heller *et al.*, 1994.

3. Entropic trapping in gels

A fundamental assumption of the biased-reptation model is that the DNA is sufficiently long so that it can form a number of blobs in the gel, $N_{\mathrm{blob}} \gg 1$. This occurs when the pore size is small compared to the radius of gyration, $a \ll R_g$. If the pore size is large compared with the radius of gyration of the DNA ($a \gg R_g$), then we are in the Ogston sieving regime. The dynamics are described by the Ogston-Morris-Rodbard-Chrambach model (Ogston, 1958; Morris, 1967; Rodbard and Chrambach, 1970), which was reviewed previously by Viovy (2000).

A third regime, known as entropic trapping, exists when the pore size is commensurate with the radius of

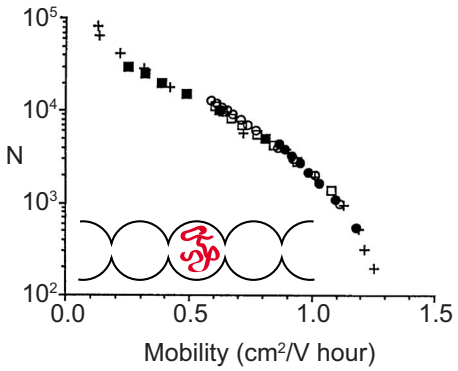

FIG. 6. (Color online) Electrophoretic mobility for different degrees of polymerization N of linear and star samples of polystyrene sulfonate. The circles and squares are different star samples; the linear samples are the + symbols. The inset shows the principle behind entropic trapping when the pore size a is commensurate with the radius of gyration, R_g. Data from Smisek and Hoagland, 1990.

gyration of the DNA ($a \approx R_g$). As shown in the inset of Fig. 6, the DNA can then freely coil into the large pores. In order to move to an adjacent pore, the DNA needs to squeeze through a small connecting hole. The latter step requires overcoming an entropic energy barrier due to the lower number of configurations available to the DNA as it passes through the hole. In a gel, we would expect to have a heterogeneous distribution of pores, with some of them being large enough for entropic trapping. However, it is possible to make a more ordered system of regular pores by patterning voids in a hydrogel (Liu *et al.*, 1999a, 1999b) or making an inverse opal from a colloidal crystal (Nykypanchuk *et al.*, 2002). Indeed, the latter papers represent the most direct observations of entropic trapping in the absence of an electric field.

In contrast to the theory of biased reptation, which was developed in response to experimental observations, the study of entropic trapping was initiated by a series of simulations by Baumgartner and Muthukumar (Baumgartner and Muthukumar, 1987; Muthukumar and Baumgartner, 1989a, 1989b). For a self-avoiding chain in a random system of obstacles, the diffusion decays exponentially with N_k once the obstacle density is large enough (Muthukumar and Baumgartner, 1989a). The rapid quenching of the diffusion with increasing molecular weight is the signal of entropic trapping.

Figure 6 presents the first clear example of entropic trapping in the context of gel electrophoresis. In this study, Smisek and Hoagland (1990) examined the electrophoretic mobility of linear polystyrene sulfonate (PSS) and star polystyrene sulfonate in low-concentration agarose. If the separation was due to Ogston sieving, then the mobility would depend on the molecular radius. However, as the data in Fig. 6 illustrate for PSS, the mobility only depends on the degree of polymerization. The entropic trapping phenomena are robust, having been demonstrated for DNA in agarose gels (Smisek and Hoagland, 1990; Mayer *et al.*, 1993), as well as PSS (Arvanitidou and Hoagland, 1991) and single-stranded DNA (Rousseau *et al.*, 1997) in polyacrylamide gels. A wide number of scaling results have also been reported. For example, Arvanitidou and Hoagland (1991) found that $\mu \sim N^{-2.1}-N^{-2.4}$ for PSS, eventually limiting to the biased-reptation result $\mu \sim N^{-1}$ for large N. The latter scalings contrast with the value $\mu \sim N_k^{-1.6}$ observed by Mayer *et al.* (1993) for double-stranded DNA.

C. The nuts and bolts

With its combination of physics, engineering, and analytical chemistry, DNA electrophoresis in microfabricated devices is an intrinsically interdisciplinary topic. While this review focuses primarily on the physics of DNA electrophoresis in microfabricated and nanofabricated devices, it is useful for us to discuss how these devices are actually constructed. We will not dwell on the details; these can easily be obtained in standard texts on microfabrication (Campbell, 2007).[2] Rather, we hope that this section will allow modeling-oriented readers to put the subsequent experimental data into context.

1. Device fabrication from the top down

The most common substrates that we encounter in this review are silicon, glass, and PDMS. As we will see shortly, glass (or, even better, fused silica or quartz) is the best substrate for microfluidic and nanofluidic devices owing to its transparency, well-known surface properties, and high electrical resistance. However, glass microfabrication is expensive and not always available. The tools for micromachining silicon are more readily (but not universally) available for academic use, owing to its ubiquity in semiconductor research. Although it is relatively easy to make robust microfluidic systems in silicon, the substrate itself is not transparent and must be oxidized prior to use to convert the surface to silicon dioxide. PDMS is an inexpensive option for producing many identical devices from a silicon or photoresist mold. Unfortunately, DNA electrophoresis in PDMS verifies the maxim that "you get what you pay for," as the porous and natively hydrophobic PDMS is plagued by a number of troublesome material properties. In all cases, the resulting device is electrically insulating and the electric field thus curves around surface features such as a post. As we will see later, the nonuniform electric field often plays a critical role in the DNA transport phenomena in a given device. Many other plastic materials are also available for microdevices, each with their advantages and drawbacks (Becker and Locascio, 2002).

Figure 7(a) outlines the basic strategy for fabricating silicon and glass devices. First, a two-dimensional pattern defining the channel and any internal structures is transferred into a resist. If the smallest feature sizes are

[2]In Sec. II.C.1, we restrict our references for the most part to the fabrication of those devices discussed in subsequent sections.

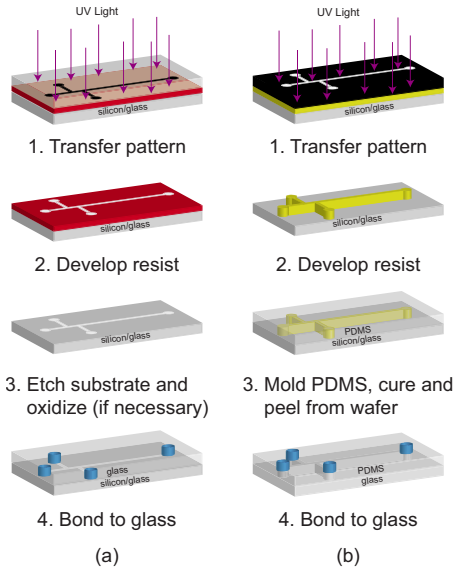

FIG. 7. (Color online) Schematic overview of device fabrication. (a) Conventional microfabrication in silicon and glass. To provide high-resolution features, these systems usually use a positive photoresist. Exposed positive resist is removed during the developing stage. Oxidation is required for silicon substrates to prevent conduction through the silicon. (b) PDMS microfabrication. The negative photoresist SU-8 is commonly used; the exposed SU-8 remains after the developing step. The PDMS is normally oxidized in a plasma to render it hydrophilic and make a strong seal to glass. The first step of this figure is optical lithography, which is useful for producing features larger than 1 μm. For smaller-scale features, electron-beam lithography, and nanoimprint lithography, among other methods, can replace the first step.

no less than 1 μm, this is commonly accomplished via optical photolithography. Recall from Table I that this length is commensurate with the size of coiled λ-DNA. One of the major advantages of photolithography is that large areas can be patterned in a single step.

While photolithography can produce submicron features (Chan *et al.*, 2003), it is quite common to resort to electron-beam lithography to pattern smaller structures such as in a nanopost array (Kaji *et al.*, 2004). The linewidth of advanced electron-beam systems is now below 10 nm, so it is relatively easy to reach length scales commensurate with the persistence length of double-stranded DNA. Electron-beam lithography is a direct write method; rather than use the masking step in Fig. 7(a), the electron beam directly transfers the pattern into the resist. Thus, electron-beam lithography is slow and patterns are nominally limited to hundreds of microns (Kaji *et al.*, 2004; Shi *et al.*, 2007). It is possible to make a larger pattern through a step-and-repeat method (with the potential for some stitching errors), with a concomitant increase in time.

Perhaps the biggest drawback to electron-beam lithography is that the time and money invested in writing the pattern yield a single device. Nanoimprint lithography (Chou *et al.*, 1997) is a route around this limitation. In this method, we first use electron-beam lithography to make a mold with the negative of the nanoscale features. The mold is then used to stamp the pattern into the resist, thereby replacing the first step of Fig. 7. Importantly, the mold can be used numerous times to (i) imprint the pattern at many locations on the same wafer and (ii) imprint multiple wafers. Thus, the time invested to create the mold opens the possibility of making many nanostructured devices. From a manufacturing perspective, nanoimprint lithography seems to be the most attractive method to produce nanoscale versions of the devices we discuss here.

Regardless of the approach used to pattern the wafer, the resist pattern is then transferred to the substrate by etching, which controls the height of the channel and its features. Dry etching is often used for small features; reactive ion etching is common for aspect ratios close to unity, whereas deep-trench etching is best for large aspect ratios. Creating a deep trench without scalloping the feature is an art and requires significant optimization of the protocol (Chan *et al.*, 2006; Mao and Han, 2009). Compared to dry etching, wet etching is a simpler procedure (you simply dip the substrate in an etchant such as buffered hydrofluoric acid), but wet etching is not well suited for high aspect ratios. The principle behind etching is that the resist is removed more slowly than the substrate, so that at the end of the etching step the resist is thinner but still protecting the substrate. For aggressive etches (e.g., wet etching) or resists that are thin relative to the etch depth, the polymeric photoresist is often replaced with a metal or oxide mask to increase the etch selectivity. The etch depth is limited by the aspect ratio of the system. As a result, it is relatively easy to make shallow etches that create nanoslits. (Sealing and operating such devices are considerably more challenging.) To create a multilevel pattern such as the slit-well motif, two patterning and etching steps are required (Han and Craighead, 1999). At some point in the process, access holes are drilled or etched into the original substrate.

To create the final device, the channel is closed by bonding to a second substrate. If the DNA is to be imaged using high-magnification immersion objectives, the second substrate needs to be a thin piece of glass, such as a coverslip. However, if the original substrate itself was a thin piece of glass, then the device can be sealed with a PDMS slab (Shi *et al.*, 2007). If one simply wants to obtain electropherograms using a long working length objective, the second substrate can be a thicker (and easier to handle) piece of glass, such as a microscope slide.

While microfabrication in silicon is generally easier than in glass, applying an electric potential in a silicon microchannel can lead to the formation of bubbles or a loss of current in the channel during electrophoresis (Harrison *et al.*, 1993). As a result, the Si near the surface is often converted to SiO_2 by thermal oxidation prior to bonding. While the resulting surface is now effectively glass, the oxide layer itself can break down when the potential is too high. As a rule of thumb, centimeter-scale oxidized silicon devices are normally operated at 100 V/cm or lower (Bakajin *et al.*, 2001; Fu

et al., 2005). If necessary, the surfaces of these devices can be further modified by the Hjerten method (Hjerten, 1985) to suppress electro-osmotic flow and adsorption to the walls. However, a high ionic strength buffer such as TBE 5× appears to suppress the electro-osmotic flow in the absence of any additional surface treatment (Han and Craighead, 1999; Kaji *et al.*, 2007).

The PDMS microfluidic devices discussed in this review are produced via the methods pioneered by the Whitesides group (Duffy *et al.*, 1998) and shown in Fig. 7(b). The first step of this method is to create a mold that contains the negative image of the channel structure. In the "rapid prototyping method," the mold is formed in photoresist by optical lithography. For relatively large features ($\geqslant 10$ μm), this is most easily accomplished using a negative photoresist such as SU-8 (step 2b in Fig. 7), whereas smaller features can be obtained using a positive photoresist (step 2a in Fig. 7). The height of the channel is thus fixed by the thickness of the photoresist. To provide more flexibility over the channel height (and to make a more robust mold), one can etch the photoresist pattern into the wafer (step 3a of Fig. 7). To create the chip, the viscous PDMS is mixed with a cross-linker, poured over the mold, and cured by heating. In order to release the PDMS, the silicon and photoresist are coated with a monolayer of silane prior to the molding. The cured PDMS is then pealed off the mold, which can be reused to create another device. The number of devices that can be fabricated from a wafer is limited by the robustness of the mold. For example, photoresist molds tend to delaminate after several dozen uses. As was the case with silicon and glass devices, access holes need to be added to the patterned PDMS and the channel is then sealed to a glass substrate. The sealing is usually accomplished by oxidizing the PDMS and glass cover in an air plasma, which not only provides an irreversible seal but also renders the PDMS temporarily hydrophilic.

In the context of electrophoresis, the main advantages of PDMS are its cost, the ease in producing additional devices from a single mold, and its optical transparency. However, these benefits are offset by a quartet of shortcomings: (i) It has also been our experience that DNA tends to adsorb irreversibly to PDMS, making disposability a necessity rather than an option. (ii) The channels need to remain wet at all times to limit hydrophobic recovery (Morra *et al.*, 1990). (iii) The PDMS itself needs to be saturated with buffer to avoid pervaporation (Verneuil *et al.*, 2004; Randall and Doyle, 2005b). (iv) The surface properties of PDMS are often heterogeneous, making control of the electro-osmosis more difficult than in silicon or glass. Electro-omosis can be suppressed by combining a high ionic strength buffer (TBE 2.2×) with high molecular-weight poly(vinylpyrollidone) (PVP) (Randall and Doyle, 2004). PVP is also a hydrophillic polymer, so its physioadsorption to the PDMS surface can add some hydrophilicity (van der Linden *et al.*, 2006).

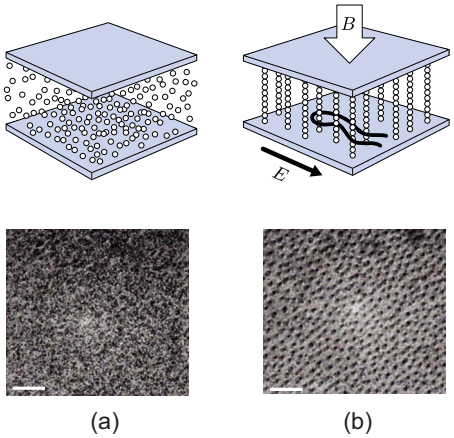

FIG. 8. (Color online) Self-assembly of superparamagnetic beads. (a) In the absence of a magnetic field, the beads form a homogenous suspension of particles. (b) In the presence of the magnetic field, the beads assemble into a quasihexagonal array of posts. The scale bar is 10 μm. The schematic on top is complements of Michel Gauthier; the experimental images below are from Minc (2005).

2. Device fabrication from the bottom up

The top-down lithographic approach discussed above is the method of choice for creating precisely defined periodic geometries. Owing to the clean-room processing time required to produce these devices, they are expensive and, for the time being, nondisposable if fabricated in glass or silicon. Moreover, devices with very fine features can be easily clogged by contaminants, rendering the device unusable. Some of these obstacles are overcome by replica molding in a polymeric material, such as the PDMS strategy described above. If problems arise, the inexpensive replica is discarded and a new device is produced from the master mold. However, creating a master mold with micron-scale features still requires clean-room processing.

As a result, a number of groups have pursued bottom-up (self-assembly) fabrication methods to avoid the expensive processing steps required to produce sieving matrices inside microchannels. An agarose gel is perhaps the simplest "self-assembled" system—upon cooling, the agarose/buffer mixture automatically forms the separation matrix, albeit a disordered one. The aim of the two bottom-up methods discussed below is to form a periodic separation matrix with similar ease.

The most well-developed self-assembly method, at least in terms of its application to DNA electrophoresis, is the magnetic bead array shown in Fig. 8 (Doyle *et al.*, 2002; Minc *et al.*, 2004; Minc, Bokov, *et al.*, 2005). In the absence of a magnetic field, the superparamagnetic beads have no magnetic moment and form a homogeneous suspension. This suspension is easily injected into the microchannel via pressure-driven flow. When a magnetic field is applied along the channel height, the beads stack into columns and form a quasihexagonal array in the thin slit (Liu *et al.*, 1995). After the electrophoresis experiment, the magnetic field is turned off and the beads can be easily flushed from the channel by a

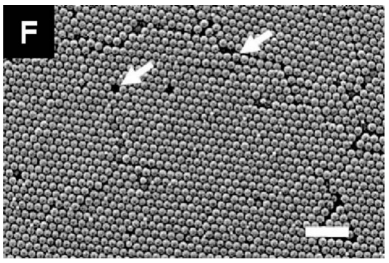

FIG. 9. Colloidal crystal of 2 μm polystyrene spheres packed by evaporation from the exit of a PDMS microchannel. The scale bar is 10 μm and arrows indicate point defects. From Zeng and Harrison, 2007.

pressure-driven flow. The exact structure of the array depends on both the surface properties of the magnetic particles (Minc *et al.*, 2004) and the shape of the bounding walls of the microchannel (Haghgooie *et al.*, 2006).

Colloidal crystals are the second self-assembled system used for electrophoresis thus far. The assembly and applications of colloidal crystals are a vast field of research, for example, in photonics and nanofabrication. The use of colloidal crystals to study DNA electrophoresis was pioneered by Meistermann and Tinland (2000) and since adopted by a number of groups (Zhang and Wirth, 2005; Zeng and Harrison, 2006, 2007; Shiu *et al.*, 2008; Zeng *et al.*, 2008). The crystals are normally fabricated using convective assembly (Norris *et al.*, 2004). It is challenging to create defect-free colloidal crystals over the large areas required for DNA separations. However, it appears that crystals grown via convective assembly in a PDMS microchannel, such as the one in Fig. 9, are sufficiently well ordered to separate DNA (Zeng and Harrison, 2007).

III. COLLISION WITH AN ISOLATED POST

We begin our discussion of the DNA dynamics in microfabricated systems by considering the collision of a long DNA molecule with an isolated obstacle, as in Fig. 10. The post-collision problem is fundamental to DNA electrophoresis; Kenward and Slater (2006) went so far as to describe this problem as "the basic quantum of separation." Indeed, although the work discussed in the present section was motivated by early experiments on DNA electrophoresis in post arrays (Volkmuth and Austin, 1992; Austin and Volkmuth, 1993), there is ample evidence that rope-over-pulley dynamics play a key role in gel electrophoresis (Schwartz and Koval, 1989; Smith *et al.*, 1989; Gurrieri *et al.*, 1990; Song and Maestre, 1991; Oana *et al.*, 1994) and polymer solutions (Shi *et al.*, 1995; Schwinefus *et al.*, 1999; de Carmejane *et al.*, 2001; Chiesl *et al.*, 2006; Forster *et al.*, 2009).

In what follows, we use three different metrics to describe the time scale for the DNA and post interaction: (i) the unhooking time t_{unhook}, the collision time t_c, and the hold-up time t_H. The unhooking time is the time required for an extended DNA molecule to transfer all of its mass to one side of the post. From a modeling standpoint, this is the most convenient metric. However, it is challenging to measure experimentally. The collision time is the sum of the unhooking time and the time required for the DNA to unravel from a coil into its extended form. Again, this time is challenging to measure experimentally. The hold-up time is the most convenient experimental and simulation metric (Saville and Sevick, 1999). Prior to the collision with an isolated post, the DNA is moving at its free-solution mobility. Likewise, at some point after the collision, the DNA will return again to its free-solution mobility. The hold-up time is the lag between these two points in time and readily extracted from trajectory data of the center of mass in the direction of the electric field, as in Fig. 10.

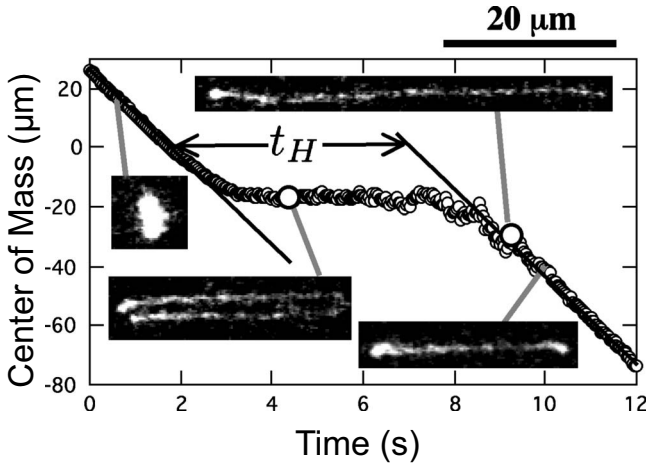

FIG. 10. Visualization of the post-collision process for T4-DNA colliding with a 0.8 μm radius PDMS post at a Péclet number Pe=8 [see Eq. (28)]. The center-of-mass position is measured in the direction of the electric field (from left to right in the images). The hold-up time t_H is computed from the offset between the slopes of the trajectories in the two regimes where the DNA moves with the free-solution mobility $\mu_0 E$. The first open circle and its image correspond to the point where the DNA is wrapped around the post and reaches complete extension. The second open circle and its image correspond to the conformation of the DNA when it is released from the post. From Randall and Doyle, 2006.

A. Unhooking from the post

1. A simple mechanical model

In a strong electric field, the simplest model of the post unhooking process is the rope-over-pulley system. Many have described the process in the context of DNA electrophoresis (Nixon and Slater, 1994; Sevick and Williams, 1994; Volkmuth *et al.*, 1994; Popelka *et al.*, 1999), with Randall and Doyle (2006) providing a clear derivation in the context of a bead-spring model. In the post-collision taxonomy (Randall and Doyle, 2006), collisions with nearly symmetric extended arms at the outset are referred to as U collisions and those with asymmetric extended arms at the outset are J collisions. From a practical standpoint, little is gained by defining a rigorous distinction between the two types of collisions.

To quantify the strength of the electric field, we use the Péclet number (Randall and Doyle, 2004)

$$\mathrm{Pe} = \frac{\mu_0 E l_p}{D}. \tag{28}$$

A Péclet number measures the relative effect of convection to diffusion over some length scale. The Péclet number defined in Eq. (28) measures the time scale for diffusion of the chain over the persistence length l_p^2/D relative to the time for electrophoretic convection over the same distance $l_p/\mu_0 E$. A large Péclet number corresponds to convection-dominated transport. The Péclet number is not unique since one can chose other length scales or diffusive rates (e.g., diffusivity of a Kuhn segment rather than the coil).[3] We prefer the Péclet number in Eq. (28) since it contains experimentally measurable parameters.

With the data in Table I, a useful approximation for λ-DNA in a PDMS channel is

$$\mathrm{Pe} \approx 0.2E \text{ (V/cm)} \quad \text{for λ-DNA}. \tag{29}$$

To a large extent, the simulation data reviewed here do not incorporate hydrodynamic interactions. As a result, these simulations feature Rouse diffusion. The Rouse diffusion coefficient is

$$D^{\mathrm{Rouse}} = \frac{k_B T}{\xi_k N_k}. \tag{30}$$

Inserting the latter into the definition of the Péclet number in Eq. (28), we arrive at a second useful form,

$$\mathrm{Pe} = \frac{\mu_0 E \xi_k \mathcal{L}}{2 k_B T}, \tag{31}$$

where we have used the definition of the contour length $\mathcal{L}=N_k l_k$ and the relationship between the persistence length and Kuhn length $l_k=2l_p$. Both Eqs. (28) and (31) measure the ratio of convection to chain diffusion over a persistence length. From Brownian dynamics simulations of the collision with a point-sized post, Holleran and Larson (2008) found that strongly stretched collisions represent around 90% of the ensemble of collisions when $\mathrm{Pe} \geqslant 10$. A corollary of this conclusion is that the longer chains will reach the strongly stretched regime at lower electric fields.

At the start of the unhooking process, we assume that the DNA is strongly extended in the electric field direction so that the total contour length $\mathcal{L}$ is divided into the two arms shown Fig. 11. We denote the instantaneous offset between the arms by $\chi(t)$ and the instantaneous length of the short arm by $\chi_1(t)$ such that $\mathcal{L}=2\chi_1+\chi$ is a constant. It is possible to consider nonuniform tension and extension during the unhooking process using a Langevin formulation. The numerical solution of the resulting dynamical equation still leads to exponential shrinking of χ_1 in time (Sevick and Williams, 1994).

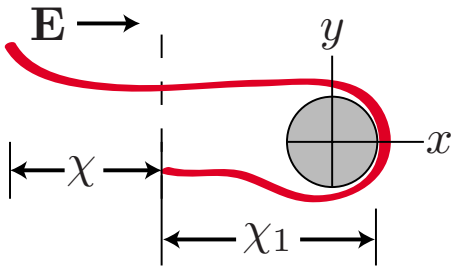

FIG. 11. (Color online) Schematic of the rope-over-pulley collision for an extended chain. The instantaneous difference in length between the two arms is denoted $\chi(t)$ and the length of the short arm is $\chi_1(t)$. The time $t=0$ is the start of the unhooking process. An (x,y) Cartesian coordinate system is fixed on the center of the obstacle such that the net DNA motion is in the $-x$ direction.

If the electrical force and friction acting on each arm are proportional to the arm length, then the time t_{unhook} required to unhook from an initial offset $\chi(0)$ is given by

$$t_{\mathrm{unhook}} = -\frac{\mathcal{L}}{2\mu_0 E} \ln\left[\frac{\chi(0)}{\mathcal{L}}\right]. \tag{32}$$

The free-solution mobility μ_0 appears in the latter result with use of Eqs. (10) and (11). When we discuss X collisions in Sec. III.A.5, it will prove convenient to rewrite this result in terms of the initial length of the short arm (Randall and Doyle, 2006),

$$t_{\mathrm{unhook}} = -\frac{\mathcal{L}}{2\mu_0 E} \ln\left[1 - \frac{2\chi_1(0)}{\mathcal{L}}\right]. \tag{33}$$

While the unhooking time is convenient for theoretical modeling, it is actually rather challenging to measure experimentally due to uncertainty about when (if ever) the two arms reach their full extension and start the unhooking process. Indeed, we will see in Sec. III.A.5 that the commonly invoked model of pulley formation followed by unhooking (Nixon and Slater, 1994) may not be an accurate description for all collisions. For an isolated post, it is much easier to describe experimental and simulation data with the hold-up time t_H proposed by Saville and Sevick (1999) and shown in Fig. 10. In what follows, we initially continue by focusing on models for t_{unhook}, ultimately making the connection to t_H in Sec. III.A.6.

To see how post collisions could be used for separations, we should also consider the average unhooking time. To make such a calculation, we need a distribution for the initial offset $\chi(0)$. Nixon and Slater (1994) proposed two simple models. If a previous collision tends to leave the DNA molecule aligned with the center of the next post and the DNA molecule is relaxed, then we

[3] In what follows, we recast the various results in the literature in terms of the Péclet number in Eq. (28) and model equations for the experimental parameters. For reference, the Pe here is $N_k/2$ times larger than the Pe defined by Patel and Shaqfeh (2003) and Holleran and Larson (2008) and $2N_k$ times larger than the Pe defined by Laachi *et al.* (2009a). The dimensionless parameter γL of Volkmuth *et al.* (1994) corresponds to $\sqrt{2\,\mathrm{Pe}\,N_k}$ here.

might expect the arms to be nearly symmetric. The latter situation is modeled by a Gaussian distribution for $\chi(0)$ centered around $\mathcal{L}/2$. If the collisions are uncorrelated, then a uniform distribution of offsets is more appropriate. Assuming $0 \leqslant \chi \leqslant \mathcal{L}$, then the average unhooking time for a uniform probability distribution is

$$\langle t_{\text{unhook}} \rangle = \frac{\mathcal{L}}{2\mu_0 E}. \tag{34}$$

Using Brownian dynamics simulations of the collision with an isolated post, Kim and Doyle (2007) found that the length of the short arm indeed reaches a uniform distribution as the electric field strength increases. Interestingly, Kim and Doyle (2007) also found that the offset χ between the two arms is skewed toward smaller values as the electric field increases, which can be attributed to the X collisions discussed in Sec. III.A.5. Looking ahead, the long arm in an X collision is shorter than it would be if it was completely extended, thus reducing the apparent value of the offset.

2. The fluctuating rope over pulley

The deterministic rope-over-pulley model given by Eq. (32) diverges when the initial offset between the two arms vanishes, i.e., $\chi(0)=0$. Fortunately, as long as these collisions do not make a large contribution to the ensemble, the singularity is integrable and leads to finite average hold-up times such as Eq. (34) (Nixon and Slater, 1994). As a result, most models of transport in post arrays ignore the singularity—the integrals and summations required to compute the mean velocity and dispersion coefficient converge even though the hold-up time for $\chi(0)=0$ is infinitely long.

If we want to properly model the unhooking process for $\chi \ll \mathcal{L}$, we need to consider the effects of both convection and diffusion on the curvilinear motion of the chain. This leads to a first-passage time problem (Volkmuth *et al.*, 1994; Redner, 2001) for the convection-diffusion process in an inverted harmonic potential with a pulse of probability density at $\chi(0)$ and adsorbing boundaries at $\chi = \pm\mathcal{L}$. Volkmuth *et al.* (1994) developed approximate results for several limiting cases. The chain at some initial offset $\chi(0)$ randomly diffuses back and forth along its contour until it passes the critical offset,

$$\chi^* \sim \frac{\mathcal{L}}{(\text{Pe}N_k)^{1/2}}, \tag{35}$$

where the convection flux due to the electrical force balances the diffusive flux (Kenward and Slater, 2006; Laachi *et al.*, 2009a). Taking λ-DNA ($N_k=166$) and an electric field of 1 V/cm as lower bounds for the electric field and molecular weight, we see with Eq. (29) that $(\text{Pe}\, N_k)^{1/2} \gg 1$. Using the latter in Eq. (35) means that $\chi^*/\mathcal{L} \ll 1$. In other words, the curvilinear motion of the unhooking chain during an experiment is governed by diffusion only for very small offsets. Thus, if $\chi(0) \gg \chi^*$, the first-passage time analysis approaches the deterministic limit given by Eq. (32) (Volkmuth *et al.*, 1994). If the offset and the electric field are small, Volkmuth *et al.* (1994) assumed that the time required to diffuse to the offset χ^* is also small compared to the ensuing rope-over-pulley unhooking time. Inserting Eq. (35) into Eq. (32), this logic leads to an unhooking time

$$t_{\text{unhook}} \approx \frac{\mathcal{L}}{4\mu_0 E} \ln(\text{Pe}N_k) \quad \text{for } \chi(0) \ll \mathcal{L}, \tag{36}$$

independent of the initial offset.[4]

While the mean first-passage time can be expressed as an integral (Volkmuth *et al.*, 1994), computing other statistical measures such as the survival probability distribution or higher-order moments of the first-passage time requires numerically solving the convection-diffusion equation with a fine mesh. The latter quantities are more easily evaluated by taking advantage of an analogy between the unhooking process and polymer translocation (Laachi *et al.*, 2009a). Explicitly, the passage of Kuhn segments from the short-arm side of the post to the long-arm side is equivalent to monomers moving through a pore connecting two reservoirs. We can thus use the powerful methods developed for translocation problems [Gauthier and Slater (2008)] to address all of the statistical properties of the unhooking process. This "translocation" model of post unhooking is consistent with the equivalent first-passage time description and produces results that compare favorably with more detailed Brownian dynamics simulations of the unhooking time distribution for $\chi(0)=0$ (Laachi *et al.*, 2009a).

Armed with the latter results, Laachi *et al.* (2009a) demonstrated that the diffusive fluctuations make a negligible contribution to the first two moments of the unhooking time even at the lowest electric fields (10 V/cm) and chain lengths ($N_k=50$, e.g., λ-DNA digested with XhoI) used in separation experiments. That being said, it is still possible for the chains to become trapped in long-lived hairpin configurations if the electric field is so large that thermal fluctuations are negligible (Patel and Shaqfeh, 2003). From a practical standpoint, these trapped DNA would never make it to the end of the channel. As a result, the main effect of long-lived trapped states on a separation would be to lower the signal at the detector rather than increase the width of the band.

[4]Formulating the convection-diffusion problem in terms of the offset requires accounting for the fact that $\partial\chi = -2\partial\chi_1$ (Laachi *et al.*, 2009b). Olson *et al.* (2001) noted that the first-passage time result in Eq. (1) of Volkmuth *et al.* (1994), along with the deterministic result in the latter text, does not include these numerical prefactors. Thus, the $\chi_1(0) \ll \mathcal{L}$ approximation and the deterministic results reported by Volkmuth *et al.* (1994) differ from Eqs. (36) and (32) by factors of 4 and 2, respectively. From a practical standpoint, the role of these numerical prefactors is likely to be small compared to the other assumptions in the model.

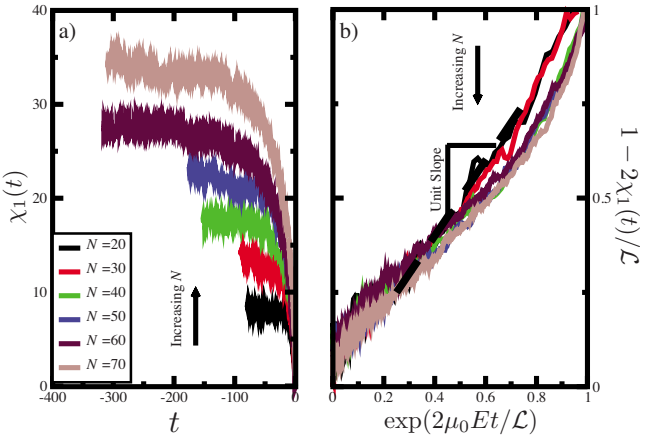

FIG. 12. (Color online) Unhooking dynamics for different length chains from molecular-dynamics simulations. The number N is the number of beads used to represent the chain. The axis labels have been converted to the present notation assuming that the chain friction is independent of the chain conformation. From Kenward and Slater, 2006.

3. Hydrodynamic interactions

One of the possible problems with this simple model of the unhooking from a post is the neglect of hydrodynamic interactions between different segments of the chain. As noted by Long *et al.* (1996), the motion of the counterions during free-solution electrophoresis leads to shear in the Debye layer, which screens hydrodynamic interactions between segments. However, when the chain is wrapped around the post, the counterions can still move freely but the DNA is acted on by a nonelectric force (the steric interaction with the post). As a result, hydrodynamic interactions between segments of the chain and between the chain and the post may be sensible.

If the chain is completely stretched, as is the case in Fig. 11, hydrodynamic interactions between different Kuhn segments do not contribute to the unhooking time (André *et al.*, 1998). However, experiments indicate that the chain is relaxed at its ends (due to the absence of tension there) during unhooking (Volkmuth *et al.*, 1994), so hydrodynamic interactions could be important. The role of hydrodynamic interactions was addressed by Kenward and Slater (2006) using molecular-dynamics simulations with explicit solvent.[5] Figure 12 reproduces unhooking data thus obtained after the collision with a small post. During the early parts of the unhooking process, the exponential unhooking dynamics of Eq. (33) are apparent, in agreement with the assertion by André *et al.* (1998). However, the unhooking rate increases toward the end of the process. For the particular value of the electric field (constant force) used for Fig. 12, the increased curvilinear velocity is attributed to an approximately 15% compression of the ends of the chain (Kenward and Slater, 2006), which reduces the friction.

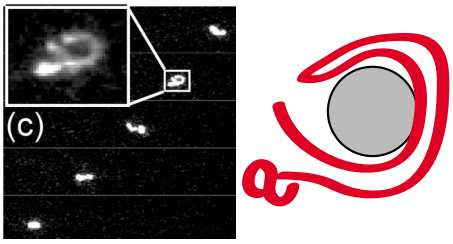

FIG. 13. (Color online) Visualization of the W collision of T4-DNA with a 0.8 μm radius post at Pe=8. From Randall and Doyle, 2006.

While hydrodynamic interactions during unhooking likely make a minor contribution to the total unhooking time in a strong electric field, hydrodynamic interactions between the loops of the chain may also play a role as the DNA unravels around a post (André *et al.*, 1998). Such interactions would be important in the modeling of so-called W collisions (Randall and Doyle, 2006), such as the one in Fig. 13. However, a detailed understanding of the hydrodynamics of this situation is probably not necessary to arrive at a useful model of the unhooking process. The W collision is metastable and often converts into the U or J collision (or the X collision of Sec. III.A.5) during the unraveling process (Randall and Doyle, 2006). Moreover, W collisions such as the one in Fig. 13 are rare and only occur for very long molecules. For example, Randall and Doyle (2006) observed some W collisions for T4-DNA with a 0.8 μm radius post, but no such collisions were observed for λ-DNA in the same system. Kim and Doyle (2007) suggested that the absence of W collisions for λ-DNA is due to the limited spatial resolution of the experiment, as these collisions were observed in Brownian dynamics simulations of the same system. Even if W collisions constituted a nonnegligible fraction of the ensemble of collisions, simple simulations of hairpin destruction indicate that hydrodynamic interactions do not play a significant role in the unraveling process (André *et al.*, 1998).

4. Weak electric fields

Our analysis thus far assumes that the electric field is strong enough to completely stretch the chain when it is draped around the post. This may not be the case in a weak electric field. Indeed, since the tension is highest at the pivot point on the post and vanishes at the free ends of the chain, there is always some relaxation even at high electric fields. Volkmuth *et al.* (1994) confirmed this point in early experiments, noting that the ends of the unhooking chain are anomalously bright.

Two different approaches have been used to model the weak-field regime. André *et al.* (1998) and Randall and Doyle (2006) replaced the full contour length $\mathcal{L}$ with an effective contour length $\mathcal{L}^{\text{eff}}$. If the somewhat

[5]The conversion from the simulation parameters of Kenward and Slater (2006) to our notation requires neglecting the conformation dependent mobility of the simulations (Kenward and Slater, 2004) in order to arrive at the term μ_0 in Fig. 12. Fortunately, this assumption does not alter the qualitative interpretation of the data.

stretched chain is modeled by a trumpet configuration in a good solvent (Brochard-Wyart, 1993) and we continue with a freely draining approximation, then the average unhooking time scales as $N_k^{3/5}E^{-1/3}$ (André *et al.*, 1998). If hydrodynamic interactions are incorporated in the trumpet model, the friction scales with the extension of the chain in the electric field direction rather than the contour length. As a result, the unhooking time scales as N_k^3E (André *et al.*, 1998). Alternatively, the extension can be modeled by a wormlike chain at large electric fields (Marko and Siggia, 1995). For modeling DNA electrophoresis, Mohan and Doyle (2007b) proposed the approximation formula

$$\frac{\mathcal{L}^{\text{eff}}}{\mathcal{L}} \approx \begin{cases} \text{Pe}/6 & (\text{Pe} \leqslant 1) \\ 1 - \text{Pe}^{-1/2} & (\text{Pe} > 1). \end{cases} \tag{37}$$

For more accuracy at weak electric fields, the approximation above can be replaced by the numerical inversion of the full wormlike chain model (Kim and Doyle, 2007).

Holleran and Larson (2008) proposed a slightly different model. Their "ball and chain" configuration is the same as the stem-flower model of Brochard-Wyart (1995), with two extended arms (stems) capped with a ball (flower) of DNA at their ends. In our notation, the total extension of the chain wrapped on the post is (Dorfman, 2008)

$$\mathcal{L}^{\text{eff}} \approx \mathcal{L}(1 - 2/\text{Pe}). \tag{38}$$

During the unhooking, Holleran and Larson (2008) assumed (i) upon reaching the pivot point, the flower instantaneously moves to the other side of the post and (ii) the friction of the arms is proportional to the number of monomers. In their model, the hold-up time for an initial short-arm length $\chi_1(0)$ is reduced from Eq. (33) to (Holleran and Larson, 2008)

$$t_{\text{unhook}} = \frac{\mathcal{L}}{2\mu_0 E} \ln\left[\frac{1 - \text{Pe}^{-1}}{\mathcal{L} - 2\chi_1(0)}\right]. \tag{39}$$

Holleran and Larson (2008) used this expression to fit their freely draining simulation data for $1 \leqslant \text{Pe} \leqslant 10$ and found reasonable agreement. However, we would expect that the chain friction would be reduced due to hydrodynamic interactions during the unhooking process (Long *et al.*, 1996; Kenward and Slater, 2006).

While there are a number of proposals for modeling the weak electric field regime, there is little experimental evidence available to test the models. The experiments themselves are not trivial since the DNA may not stretch around a finite-sized post under a weak electric field (Saville and Sevick, 1999).

5. The X collision

In all of the models presented thus far, we have assumed that the chain is completely extended before the unhooking process starts. The decoupling of the unraveling and unhooking was first proposed by Nixon and Slater (1994). If the length of the unraveling arms increases linearly in time (Nixon and Slater, 1994; Masubuchi *et al.*, 1995; Popelka *et al.*, 1999), then the typical time to form the pulley is actually the same as the average unhooking time appearing in Eq. (34) (Nixon and Slater, 1994).

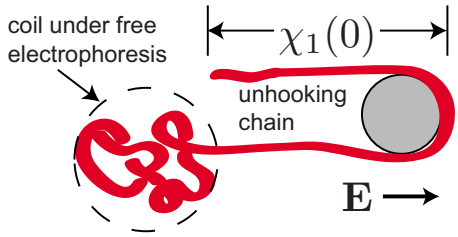

FIG. 14. (Color online) Schematic depiction of an X collision. The length of the short arm is $\chi_1(t)$.

We can also imagine the situation in Fig. 14, where the short arm completely uncoils to some length χ_1 while the coiled portion of long arm is still unraveling at a rate $\mu_0 E$. In this case, the short arm begins unhooking *before* the long arm completely uncoils. Randall and Doyle (2006) proposed calling these "extending collisions" or, more enigmatically, "X collisions." The key feature of an X collision is that the length of the long arm increases as fast as the coil can move downfield, whereas the short arm decreases in length exponentially in time (Randall and Doyle, 2006).

While Doyle and co-workers performed the most systematic investigation of this mode of unhooking through experiments (Randall and Doyle, 2006) and Brownian dynamics simulations (Kim and Doyle, 2007), X collisions have actually been described a number of times in the literature. Song and Maestre (1991) first observed X collisions during the migration of T4-DNA in gel electrophoresis. The data in this paper are very limited, with three J collisions and two X collisions at 4 V/cm and two X collisions at 8 V/cm (Song and Maestre, 1991).[6] Sevick and Williams (1994) also observed dynamics akin to an X collision from a deterministic model where the monomers begin at the position of a point-sized post and evolve according to a balance of friction, electrical force, and tension. Finally, Masubuchi *et al.* (1995), in an effort to explain the single-molecule observations of DNA migration in agarose by Oana *et al.* (1994), presented a detailed analysis of the X model.

The calculation of the unhooking time for an X collision proceeds along the same lines as the normal rope-over-pulley model, except that the length of the long arm increases linearly in time (Masubuchi *et al.*, 1995; Randall and Doyle, 2006). After a time $\chi_1(0)/\mu_0 E$ the short arm reaches its stretched length $\chi_1(0)$. The ensuing unhooking time is given by (Masubuchi *et al.*, 1995; Randall and Doyle, 2006)

[6]Interestingly, even for the J collisions observed by Song and Maestre (1991), the exponential relaxation times for the two arms differed, indicating a possible difference between X collisions with a gel and an isolated post.

$$t_{\text{unhook},X} = \left[\sqrt{2}\exp\left(\frac{\pi}{4}\right) - 1\right]\frac{\chi_1(0)}{\mu_0 E}. \quad (40)$$

The exact prefactor is due to Masubuchi *et al.* (1995) and agrees with the numerical result obtained by Randall and Doyle (2006). This unhooking time is physically consistent if $\chi_1(0)/\mathcal{L} < 0.3$ (Randall and Doyle, 2006). If the long arm does not contain enough segments, then it will become stretched before the chain completely unhooks. The analysis in this case is somewhat more involved and discussed by Masubuchi *et al.* (1995).

While much of the post-collision literature has focused on U/J collisions, the X collision is actually relatively common. Experiments for T4 collisions at Pe=8 led to approximately 60% X collisions (Randall and Doyle, 2006), and related Brownian dynamics simulations indicate that the fraction of X collisions indeed saturates around 60% as the Péclet number increases (Kim and Doyle, 2007). The shift from U/J collisions toward X collisions is due to the reduced residence time at the impact point as the electric field increases; for weaker electric fields, the chain has more time to be stretched into a U or J shape (Kim and Doyle, 2007).

6. Hold-up time

As noted in Sec. III.A.1, while the unhooking time is a convenient quantity for modeling, it is not easy to measure experimentally. Rather, it is much easier to ascertain the hold-up time, t_H, proposed by Saville and Sevick (1999) and shown in Fig. 10. Far from the post, the DNA moves at the constant velocity $\mu_0 E$. Thus, a plot of the center of mass versus time is linear at some time well before and after the collision. The hold-up time is defined as the offset between these two lines. Experimentally, the slopes of the incoming and outgoing trajectories are normally within 10% of each other (Randall and Doyle, 2006).

In computing the hold-up time, Randall and Doyle (2006) noted that the center of mass actually moves downfield during the collision (Randall and Doyle, 2006). As a result, the hold-up time is not equal to the sum of the unraveling and unhooking times, as frequently used to model the dynamics in arrays of obstacles (Popelka *et al.*, 1999; Minc, Viovy, and Dorfman, 2005; Dorfman, 2006). Accounting for this center-of-mass motion, the J-hold-up time is (Randall and Doyle, 2006)

$$t_H = \frac{\mathcal{L}}{2\mu_0 E}\left[1 - \frac{2\chi_1(0)}{\mathcal{L}} - \ln\left(1 - \frac{2\chi_1(0)}{\mathcal{L}}\right)\right], \quad (41)$$

whereas the X-hold-up time is (Randall and Doyle, 2006)

$$t_{H,X} = 4.8\frac{\mathcal{L}}{\mu_0 E}\left(\frac{\chi_1(0)}{\mathcal{L}}\right)^2. \quad (42)$$

Randall and Doyle (2006) compared their experimental data to the unhooking models for J collisions [Eq. (33)] and X collisions [Eq. (40)], as well as equivalent hold-up models (41) and (42). Figure 15 demonstrates

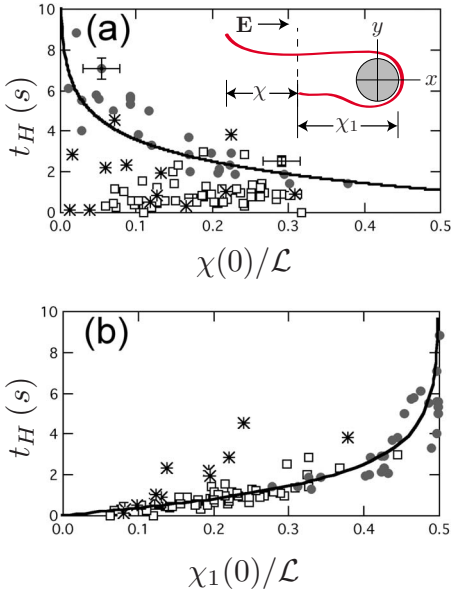

FIG. 15. (Color online) Plot of the hold-up time as a function of (a) the initial dimensionless offset between the two arms and (b) the initial dimensionless length of the short arm for T4-DNA colliding with a 0.8 μm radius PDMS post at a Péclet number Pe=8. The circles are U/J collisions, the open squares are X collisions, and the stars are W collisions. The solid line in (a) is Eq. (32) and the line in (b) is Eq. (33). Data from Randall and Doyle, 2006.

that J collision unhooking time (33), formulated in terms of the length of the short arm, adequately captures both the X and U/J collisions—without needing to account for the additional center-of-mass motion. Thus, although Eq. (33) for the J-collision unhooking time is the simplest possible model we can envision, it also appears to be the best fit to the experimental data.

Figure 15 also demonstrates the failure of using the offset between the arms in Eq. (32) to describe the X collision. The long arm is not completely extended at the start of unhooking during these collisions, so the difference between the end of the short arm and the long arm does not correctly capture the total electrical force acting on each arm due to the stored length in the long arm. Randall and Doyle (2006) argued that the J-collision model, when plotted in terms of the short-arm length, works well because the short arm is already at its steady-state tension at the start of unhooking. Note that the J-collision model fails to capture W collisions in Fig. 15. Fortunately, the latter collisions are rare and do not contribute much to the averaged behavior.

While the data in Fig. 15 only correspond to T4-DNA collisions at Pe=8, Randall and Doyle (2006) observed similar agreement between Eq. (33) and the hold-up time for λ-DNA at Pe=2 and 8. The J-collision unhooking time also captures Brownian dynamics simulations of the collision with a small post over a range of molecular weights (λ, 2λ, and T4) and Péclet numbers (Kim and Doyle, 2007).

B. Colliding with the post

In our discussion of the post problem thus far, we have only considered what happens after, at the minimum, the short arm of the DNA unravels to some initial length $\chi_1(0)$. The long arm may also be unraveled or still partially coiled. In the present section, we consider how and if an initially coiled DNA molecule reaches this state.

1. Critical Péclet number for an infinitely thin post

During its approach toward an isolated post, the DNA is presumably in its equilibrium coil conformation. In order for the DNA to unravel around the post during a collision, André *et al.* (1998) proposed that the post needs to penetrate the coil more quickly than thermal fluctuations can randomize the DNA conformation. The electrical force trying to deform the coil is $F \sim \xi_k N_k \mu_0 E$ for a freely draining model and $F \sim \xi_k N_k^{\nu} \mu_0 E$ if hydrodynamic interactions are included. André *et al.* (1998) argued that this force needs to exceed thermal energy over the characteristic size of the coil,

$$F > k_B T / R_g, \tag{43}$$

leading to a critical Péclet number for unhooking

$$\mathrm{Pe}^* \sim N_k^{\gamma}, \tag{44}$$

where $\gamma = -\nu$ for the freely draining model and $\gamma = 1 - 2\nu$ with hydrodynamic interactions.

Patel and Shaqfeh (2003) proposed a smaller-scale unraveling criteria where the Rouse relaxation time, $\xi_k l_k^2 N_k^2 / k_B T$, is long compared to the hairpin formation time, $N_k l_k / \mu_0 E$. While the nonelectric force of the post implies that a Zimm relaxation time may be more appropriate (Long *et al.*, 1996), the Rouse relaxation time used by Patel and Shaqfeh (2003) is relevant for comparison with their Brownian dynamics simulations. The balance of these two-time scales leads to a result similar to Eq. (43), except that now the force is strong relative to diffusion over the Kuhn length. This model predicts that the critical Péclet number is

$$\mathrm{Pe}^* \sim 1. \tag{45}$$

The simulations of Holleran and Larson (2008) suggested the same critical Péclet number.

It is difficult to discern which of these estimates is correct from the extant experimental data. The experiments by Volkmuth and Austin (1992) represent the lowest electric field data available in the literature. They observed rope-over-pulley collisions of 100 kbp DNA ($N_k = 333$) at an electric field of 1 V/cm. Rescaling the data in Table I for this larger DNA implies that collisions occur at least down to $\mathrm{Pe} = 0.3$. The latter result is consistent with the predictions of both Eqs. (44) and (45). Equations (44) and (45) predict different critical electric fields versus molecular weight (recall that the diffusion coefficient appearing in Pe depends on N_k), so further experiments could elucidate which model is correct.

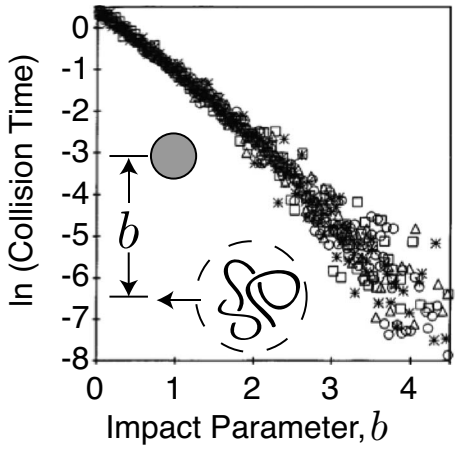

FIG. 16. Universal scaling of the dimensionless collision time $\langle t_c \rangle \mu_0 E / \mathcal{L}$ vs the impact parameter for a point-sized post. In converting from the notation of Sevick and Williams (1996) to the present one, we assumed the numerical constant $A = 1$ and that the degree of polymerization N is equivalent to the contour length $\mathcal{L}$. From Sevick and Williams, 1996.

Even if the electric field is too weak to unravel the DNA into a rope-over-pulley conformation, the post can still affect the translation of the nondeformed DNA by providing a steric obstacle, akin to the lattice models of Ogston sieving (Slater and Guo, 1996a). Remarkably, this steric hindrance appears to play a role even if the post radius is much smaller than the Kuhn length of the DNA. In their analysis of simulation data for collisions with a point-sized post, Holleran and Larson (2008) considered two mean first-passage time models, one where the DNA can pass by only on one side of the post and one where the DNA can pass by on either side of the post. Their simulation data were best described by the one-sided mean first-passage time, implying that once the DNA begins to move toward one side of the obstacle (the particular side being a random variable), the DNA passes on that side. The latter behavior persists down to $\mathrm{Pe} = 5 N_k^{-1/2}$. For even weaker electric fields, diffusion is sufficiently fast that even if the chain manages to diffuse to one side of the post, it can diffuse back to the center again.

2. The impact parameter

Even if the electric field is strong enough to unravel the DNA, the molecule still needs to collide with the obstacle in the first place. For a point-sized post, Sevick and Williams (1996) showed that a vast array of the relevant collision data can be collapsed as a function of the so-called impact parameter b. As shown in Fig. 16, the impact parameter measures the distance between the center of mass of the chain and the center of the post in the direction of the electric field, and it is easily generalized to the finite-sized posts used in experiments.

Using a deterministic model, Sevick and Williams (1996) computed the mass transfer between multiple hairpins on either side of the obstacle through a balance of friction, the electrical force, and a Langevin spring

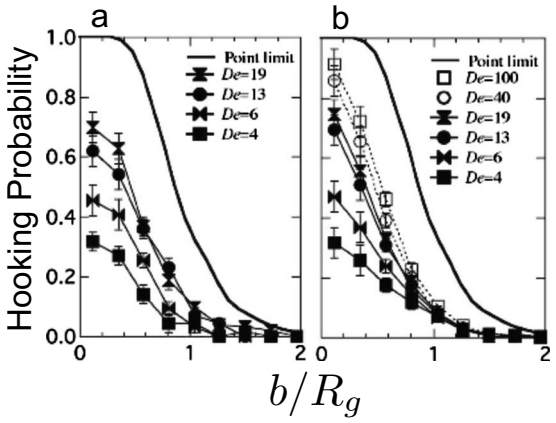

FIG. 17. Plot of the probability of λ-DNA hooking with a 0.8 μm radius post as a function the scaled impact parameter b/R_g for different values of the Deborah number De from (a) experiment and (b) Brownian dynamics simulations. The point-sized limit agrees with Sevick and Williams (1996). From Randall and Doyle, 2004.

force. The chain starts with its center of mass at some distance b from the post and the equation of motion for each monomer is integrated in time until all of the monomers lie on one side of the post. Sevick and Williams (1996) defined this time as the collision time t_c, which includes both the unraveling and unhooking processes. In practice, the collision time t_c would be slightly different from the hold-up time t_H since there may be a relaxation time prior to resuming motion at the free-solution velocity. However, since the dominant contribution to both processes is from unraveling and unhooking, $t_c \approx t_H$.

Based on dimensional analysis, Sevick and Williams (1996) suggested that the collision time has the form

$$\langle t_c \rangle = \frac{\mathcal{L}}{\mu_0 E} f\left(\frac{b}{R_g}\right). \tag{46}$$

As shown in Fig. 16, this is indeed the case, with the function f being essentially exponential for $b < 2R_g$. Sevick and Williams (1996) do not claim a fundamental reason for the exponential decay rather stating that it is simply a good fit. The center of mass at the release from the post, which Sevick and Williams (1996) defined as the collision distance, also falls on a universal curve that is linear up to $b \approx 2R_g$. This universal behavior was also reproduced in bead-rod Brownian dynamics simulations that incorporate thermal fluctuations (Patel and Shaqfeh, 2003).

While the concept of the impact parameter is extremely useful, the computational results for relatively large values of b/R_g may be artifacts of the point-sized post approximation. In experiments with an obstacle radius $R_{obs}=0.8$ μm, a size commensurate with R_g for λ-DNA, Randall and Doyle (2006) only observed hooking collisions for $b < R_{obs}+R_g$ (see Fig. 17 and the related discussion).

3. Finite-sized posts

The latter observation about the collision probability observed in experiments points out a limitation of the models discussed thus far. These models do not account for the finite size of the obstacle, treating the post as a frictionless pivot point during the unhooking process. However, microfabricated posts are obviously of finite size. Indeed, optical lithography normally leads to post diameters not smaller than 1 μm, which is one order of magnitude larger than the Kuhn length of DNA. Even posts fabricated by electron-beam lithography often have post radii that exceed the Kuhn length of DNA. Although results such as those reproduced in Fig. 15 indicate that a point-sized model adequately describes the unhooking process, the size of the post can play a dramatic role in the deformation of the DNA prior to the collision, especially when the post is large compared to the radius of gyration of the DNA.

Saville and Sevick (1999) provided the earliest discussion of the role of the post radius using a conductive obstacle (i.e., uniform electric field) as their model. As noted in Sec. II.C.1, microfabricated systems are typically electrically insulating and the electric field needs to curve around the obstacles. For an isolated post, the electrophoretic velocity has an exact solution (Randall and Doyle, 2004)

$$\frac{\mathbf{v}}{\mu_0 E} = -\cos\theta\left(1-\frac{R_{obs}^2}{r^2}\right)\mathbf{e}_r + \sin\theta\left(1+\frac{R_{obs}^2}{r^2}\right)\mathbf{e}_\theta. \tag{47}$$

The latter is based on a cylindrical coordinate system fixed on the center of the post in Fig. 11, where r is the radial distance from the post center and $\theta=0$ corresponds to the positive x axis. While the electric field distribution proximate to the obstacle is clearly nonuniform, the tangential electric field at the obstacle surface varies as $\sin\theta$, identical to the component of a uniform electric field acting tangent to the obstacle surface (Saville and Sevick, 1999). If the DNA is not deformed during a collision with a very large post ($R_{obs} \gg R_g$), then the "rolling" of a point-sized particle along insulating and conducting obstacles should be similar. Since the tangential velocity is small for small impact parameters, the DNA needs to diffuse up to a critical location s^* on the arc defining the post surface, at which point convection around the post becomes strong relative to diffusion (Saville and Sevick, 1999). As a result, roll-off collisions cannot give rise to a separation by molecular weight (Saville and Sevick, 1999).

Although the rolling dynamics may be qualitatively similar for conducting and insulating obstacles, the electric field gradients near an insulating obstacle have a profound impact on the deformation of the DNA, rendering the discussion above questionable. From an analysis of the velocity gradient, Randall and Doyle (2004, 2005a) established that the deformation near the post surface is purely elongational. The strain rate $\dot{\epsilon}(r,\theta)$ is largest at the obstacle surface. Randall and Doyle (2004, 2005a) chose to use the latter strain rate to define the Deborah number

$$\mathrm{De} = \dot{\epsilon}\tau_r = 2\mu_0 E\tau_r/R_{\mathrm{obs}}, \tag{48}$$

where τ_r is the longest relaxation time of the DNA. The Deborah number represents the ratio of the time scale for relaxation by diffusion τ_r relative to the time scale for deformation by the extensional flow $1/\dot{\epsilon}$. In the context of the post-collision problem, a large Deborah number means that the electric field gradients caused by a nearby post deform the coil. When we think about the relaxation time, we need to remember that single-molecule experiments such as the ones by Randall and Doyle (2004, 2005a, 2006) are normally performed in a thin slit to keep the DNA in focus during the experiment and suppress hydrodynamic flow. The relaxation time τ_r is affected by confinement (Randall and Doyle, 2005a); indeed, there are actually two regimes of the relaxation for long DNA in a slit as deep as 1 μm (Balducci *et al.*, 2007).

The Deborah number plays an important role in determining the probability of colliding with the post and its dependence on the impact parameter b. When they established the concept of the impact parameter, Sevick and Williams (1996) used a point-sized obstacle, which corresponds to the limit $\mathrm{De}\to\infty$. The hooking probability for this case is the solid line in Fig. 17. The latter figure illustrates the role of the strain on the hooking probability even for a relatively small obstacle (Randall and Doyle, 2004). For an impact parameter $b/R_g \ll 1$, the DNA approaches the obstacle with its center of mass aligned along the electric field line that terminates in the stagnation point on the front side of the obstacle at $y=0$. Kuhn segments located at $y>0$ are convected toward the top of the post at $y=R_{\mathrm{obs}}$, whereas their counterparts located at $y<0$ are convected toward the bottom of the post at $y=-R_{\mathrm{obs}}$. The ensuing "pre-stretching" increases the projection of the DNA onto the post, thereby increasing the probability of hooking (Randall and Doyle, 2004). For a small isolated obstacle, the strain-induced deformation only plays a role when the chain is coiled and approaches the post; during the unhooking process, the chain is stretched into the uniform electric field region (Randall and Doyle, 2006). Thus, the agreement in Fig. 15 and elsewhere (Randall and Doyle, 2006; Kim and Doyle, 2007) between experimental data and a point-sized model for a small post might be expected (even if the universal applicability of the J-unhooking model is not obvious).

The deformation due to a large post is markedly different from a small post. The strain rate near a large post can be large enough for the DNA to undergo a coil-stretch transition due to the extensional electrophoretic velocity field proximate to the post without ending up in a rope-over-pulley conformation (Randall and Doyle, 2005a). In principle, the DNA should be stretched when $\mathrm{De}>1/2$ (Magda *et al.*, 1988). To confirm that the Deborah number controls the deformation rather than the Péclet number, Randall and Doyle (2004) measured the extension of λ-DNA during collisions with $R_{\mathrm{obs}}=3$ and 10 μm for $\mathrm{Pe}=1.4$ and 5.5. In each case, the maximal extension of the molecule (i) increased with De at a fixed Pe and (ii) increased overall as a function of the Deborah number, with no stretch at $\mathrm{De}=0.25$ (Randall and Doyle, 2004).

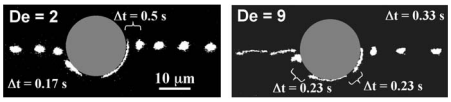

(a) (b)

FIG. 18. Collision of λ-DNA with a large insulating post. (a) Extension at $\mathrm{De}=2$ in 1.3 cP buffer. Time step Δt between frames is 0.17 s unless noted. (b) Extension at $\mathrm{De}=9$ in 6 cP buffer. The time step between frames is 0.33 s unless noted. In both images, the DNA motion is from right to left. From Randall and Doyle, 2005a.

Doyle and co-workers also studied in detail the deformation caused by the finite size of the post, focusing on head-on collisions of λ-DNA with a 10 μm radius post via experiment (Randall and Doyle, 2005a) and Brownian dynamics simulations (Kim and Doyle, 2006). Both approaches yielded similar results. When DNA approaches on the centerline during such a collision, the extensional electric field is quasihomogeneous and quickly ramps up to its maximum strain rate as the DNA approaches the post. The stretching on the frontside of the post is close to affine, and the backside compression is almost always affine (Randall and Doyle, 2005a). Figure 18 shows both the extension and compression of the molecule as it moves along the cylinder surface. Interestingly, the DNA can again be stretched at the backside of the post, with the degree of stretching at the backside of the post increasing with the Deborah number.

The extension of the DNA as it leaves the post qualitatively resembles the exiting conformations observed by Saville and Sevick (1999) for a conducting post. However, the source of the stretching is quite different in the conducting (Saville and Sevick, 1999) and insulating (Kim and Doyle, 2006) obstacle cases. In both cases, the DNA is stretched on the front side of the post. In the conducting obstacle case, the recoiling is due to thermal relaxation. The residence time of DNA that quickly rolls off a conductive post may be insufficient to achieve complete relaxation, leading to an extended exiting configuration. In contrast, the affine compression on the backside of an insulating post leads to the DNA returning to a compact state much faster than would be expected by thermal motion. The stretching at the backside in Fig. 18 is due to a second extensional component along the x axis. In simulations, the stretching saturates around $\mathrm{De}=9$ (Kim and Doyle, 2006).

The deformation near a collision is controlled by the velocity gradient, so the collision dynamics should depend on the obstacle shape. Cho *et al.* (2010) simulated the collision of λ-DNA with a small ellipsoidal obstacle. In the latter, the major axis of the ellipse forms an angle α with the uniform electric field vector $\mathbf{E}^{\infty}$ far from the obstacle surface. An exact solution for the electric potential is available in elliptical coordinates (Milne-Thomson, 1960), making the Brownian dynamics simu-

lations here almost as efficient as for cylinders. When $\alpha \neq c\pi/2$, where c is an integer, the stagnation point is no longer coincident with an axis of the ellipse. Although the DNA still forms a rope over pulley, their unhooking is biased toward one side of the ellipse (Cho *et al.*, 2010). Although the dynamics of the collision process are affected by the ellipse orientation, the probability distribution for the unhooking times is essentially independent of orientation (Cho *et al.*, 2010).

IV. DYNAMICS IN A POST ARRAY

We now move from the collision with a single isolated post to consider the dynamics of DNA moving in an array of such posts. As most of the devices (and simulations) we discuss use periodic arrays, it is convenient to define certain geometric parameters at the outset. We denote the post diameter by $d=2R_{\mathrm{obs}}$ and the center-to-center spacing by a. For a square array, the gap between the posts is thus $a-d$. For hexagonal arrays or quasiordered systems such as magnetic beads, $a-d$ still serves as a reasonable measure of the pore space (see Fig. 21). Although we mention colloidal crystals in the context of the DNA prism in Sec. IV.C.2, we otherwise restrict our discussion to two-dimensional patterns.

We generally focus on electric field strengths large enough such that $\mathrm{Pe}>1$ and the DNA is able to form a hairpin when it collides with a sufficiently small obstacle. Note that these electric fields are larger than the upper limit for the biased-reptation model given in Eq. (20). Indeed, biased-reptation models assume that the electric field is not strong enough to induce "tube leakage" due to hairpin formation.

Most imaging experiments are performed in channels around $h=2$ μm deep to keep the DNA in focus. For separations, deeper channels ($h\approx 10$ μm) are preferable to increase the signal at the detector. The choice of the channel height can have a strong effect on both the conformation and the dynamics of the chain. As the confinement increases, the chain conformation switches from a random coil to a series of blobs (Brochard and de Gennes, 1977) to a deflected chain (Odijk, 1983). Moreover, the friction is affected by the channel height. Using the unhooking from a post as a model process, the experiments of Bakajin *et al.* (1998) showed that the friction crosses through a number of regimes. For $h<\mathcal{L}$, there is partial screening of hydrodynamic interactions between the segments of the chain, whereas these interactions are completely screened for $h<l_k$.

The analytical models that we discuss do not make any corrections due to the channel height. During the post collision, they adopt a friction proportional to the length of the chain (no hydrodynamic screening by the walls), while the size of the coiled chain between collisions is modeled with the free-solution radius of gyration. Thus, these analytical models are most appropriate for separations in deep channels. In contrast, it is relatively simple to incorporate the channel walls in a simulation [see, for example, Ou *et al.* (2009)]. However, it is expensive to incorporate hydrodynamic interactions during the collision with a post. Thus, the simulation models are appropriate for a thin slit where such interactions are screened.

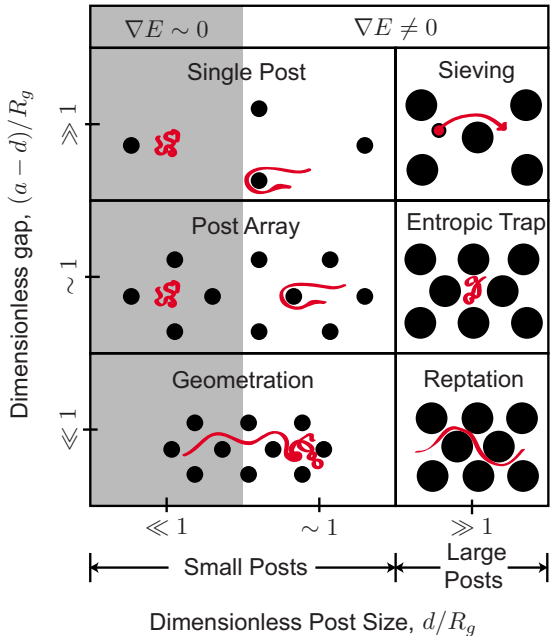

FIG. 19. (Color online) Schematic of the different types of dynamics in a post array as a function of the size of the obstacles and the gap between obstacles. These regimes are only valid for a time-independent electric field. For clarity, a representative trajectory is included for the small DNA molecule during Ogston sieving in an array of large posts.

Based on our understanding of the single-post collision, we can use the schematic diagram in Fig. 19 to classify the dynamics in a post array under a steady dc electric field. For posts that are commensurate with the radius of gyration of the DNA (or smaller, if possible), we would expect to observe hairpin collisions and subsequent rope-over-pulley dynamics. If the posts are very small, they hardly distort the electric field and a uniform electric field model is appropriate. In contrast, post diameters that are commensurate with the gap between posts introduce significant electric field gradients proximate to the post. Depending on the density of the array, these electric field gradients can be significant throughout the system. We explore how the models of single-post collisions discussed in the prior section can be used to build models in this "small post" regime by further accounting for the density of the obstacles and the nonuniform electric field.

When the posts are large relative to the size of the DNA, we would not expect to observe rope-over-pulley collisions. Rather, the dynamics here are governed by the size of the gap between these "large posts." If the gaps are very small, the DNA will not be able to form a random coil and we speculate that the DNA would reptate through the array. The dynamics reported in a number of recent publications on DNA migration in nanoslits and nanochannels would be similar to the mi-

gration in the small-gap large-post regime (Campbell *et al.*, 2004; Cross *et al.*, 2007; Mathe *et al.*, 2007; Parikesit *et al.*, 2008; Salieb-Beugelaar *et al.*, 2008; Strychalski *et al.*, 2009). As the gap increases, we begin to approach well-known regimes in gel electrophoresis. Entropic trapping has not received much attention in the context of posts and is much more easily implemented in the slit-well motif of Sec. V. While the large gap regime could be used in the conventional Ogston sieving regime, we will see shortly how microfabrication can be exploited to create sieves with sometimes surprising effects.

A. Small posts

1. Single-post limit

We begin with the simplest case of a very dilute array of small obstacles. By dilute, we mean that the nominal time to travel between rows of the array is large compared to the longest relaxation time τ_r of the DNA,

$$a \gg \mu_0 E \tau_r. \tag{49}$$

In such a dilute array, the DNA has sufficient time to relax before encountering the next post. Interestingly, the dilute-limit theories that we discuss here were motivated by experimental data on collisions in microfabricated arrays (Volkmuth and Austin, 1992), lipid bilayers (Olson *et al.*, 2001), and magnetic bead arrays (Doyle *et al.*, 2002; Minc *et al.*, 2004). The characteristic obstacle spacing in these arrays ranges from $a=2$ to 5 μm. For an electric field of 10 V/cm and a relaxation time $\tau_r = 0.19$ s (Randall and Doyle, 2004), these arrays actually correspond to $a \approx \mu_0 E \tau_r$ and are not quite dilute enough to be truly in the single-post limit.

For simplicity, assume the posts are arranged in a square array with spacing a such that $\rho = 1/a^2$ is the number of posts per unit area. Based on the distributions obtained for the collision probability, the collision time, and the distance moved during the collision, Sevick and Williams (1996) obtained an effective mobility

$$\mu/\mu_0 = 1 - c\rho N_k^{3/2}, \tag{50}$$

where c is a numerical constant. As shown in Fig. 17, the probability of hooking with a point-sized post decays dramatically as the impact parameter increases. To a reasonable approximation, the probability of colliding in a given row of point-sized posts is R_g/a. Likewise, the distance between rows is a and the nominal hold-up time is $\mathcal{L}/\mu_0 E$. With the scaling $R_g \sim N_k^{1/2}$ and $\mathcal{L} \sim N_k$, we see that the reduction is the product of the nominal collision frequency and the typical hold-up time due to the collisions (Sevick and Williams, 1996).

Patel and Shaqfeh (2003) took a similar approach to homogenize data they obtained from the two-dimensional bead-rod Brownian dynamics simulations of the collision with a small post. Their mobility result,

$$\frac{\mu}{\mu_0} = \frac{1}{1 + 0.33\rho l_k^2 N_k^{3/2}}, \tag{51}$$

includes the numerical prefactor obtained from fitting the simulation data. In the limit $\rho N_k \ll 1$, the form of Eq. (51) is the same as Eq. (50). Patel and Shaqfeh (2003) also computed the variance of the collision times from their simulations. By assuming that the dispersion is the product of the collision probability and the variance about the collision times, they obtained

$$D^*/\mu_0 E a = 0.06\rho l_k^2 N_k^{5/2}, \tag{52}$$

where the numerical prefactor again arises from fitting the simulation data.

We can also take a semiphenomenological approach toward understanding the single-post limit in lieu of simulation data (Dorfman and Viovy, 2004). Assume that there is a probability Π_c of colliding with the post in a given row and, if the collision occurs, the DNA is held up for a nominal time $\langle t_c \rangle$. This defines a simple graphical model of the process that can be solved exactly (Dorfman, 2003; Dorfman *et al.*, 2003) to obtain the mobility

$$\frac{\mu}{\mu_0} = \frac{1}{1 + \Pi_c(\gamma - 1)}, \tag{53}$$

and dispersivity

$$\frac{D^*}{\mu_0 E a} = \frac{\Pi_c(\gamma - 1)[1 + (2 - \Pi_c)(\gamma - 1)]}{2[1 + \Pi_c(\gamma - 1)]^3}. \tag{54}$$

In the latter, the parameter $\gamma = \langle t_c \rangle \mu_0 E/a$ represents the ratio of the collision time to the convection time between rows of posts.

This graphical model agrees with the simulation-based models in the limit of a very sparse array. Following the arguments of Sevick and Williams (1996), if we assume that $\Pi_c \sim \rho N_k^{1/2}$ and $\gamma - 1 \sim N_k$ then Eq. (53) has the same form as Eq. (51), albeit without the numerical prefactor. Likewise, the dispersivity appearing in Eq. (54) has the same scaling as Eq. (52) for long DNA ($N_k \gg 1$) in a very sparse array ($\Pi_c N_k \ll 1$).

Although relatively simple in origin, these single-post models allow us to make some estimates on whether DNA can be separated in dilute post arrays. For a relatively sparse array of effectively point-sized posts, Eqs. (51) and (52) predict that we should be able to separate molecular weights up to λ-DNA. However, Nixon and Slater (1994) pointed out early on that single-post models predict a "catastrophic" increase in the dispersion at high molecular weights that would render the process unusable for separations. Fortunately, this is not the case in experiments (Doyle *et al.*, 2002; Minc *et al.*, 2004) or simulations (Patel and Shaqfeh, 2003). When compared to experiments, the single-post models presented here overestimate both the hold-up time due to the collisions and the ensuing dispersion. As a result, the experimental separations are sharper and faster than would be expected based on a single-post model. For example, Minc *et al.* (2004) obtained excellent resolution between λ and

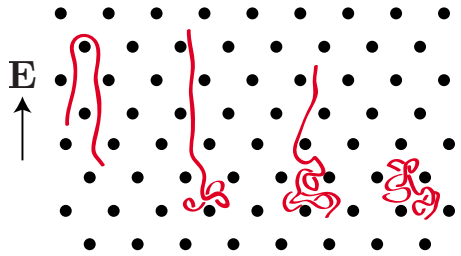

FIG. 20. (Color online) Steps in the geometration process in an array of small posts with small gaps.

T4-DNA using electric fields around $E=20$ V/cm in 2–3 min using a spacing $a=4.1$ μm and a separation length of 7.5 mm. In contrast, the most thorough single-post model (Patel and Shaqfeh, 2003) predicts that the dispersivity of T4 will be 250,000 larger than molecular diffusion and lead to nominal bandwidth of 3.7 mm—almost half of the channel. We thus need to consider more detailed models for the transport in an array if we want to capture the experimental data, especially for long DNA.

2. Geometration

Let us now take the post geometry toward the opposite limit and discuss the dynamics of DNA in an array of small posts with small gaps between the posts. If we ignore the order of the system in Fig. 20, this is a reasonable description of large DNA in an agarose gel. Indeed, the simulations and models discussed here (Deutsch, 1988; Deutsch and Madden, 1989; Shaffer and de la Cruz, 1989; Popelka *et al.*, 1999) were originally developed to describe the single-molecule dynamics observed during dc gel electrophoresis (Schwartz and Koval, 1989; Smith *et al.*, 1989).[7]

The term geometration was introduced by Deutsch (1989) to point out the analogy between the dynamics of DNA in a tight array and the motion of an inchworm. The overall process is the repetitive cycle of collision with an obstacle, rope-over-pulley disengagement, and an electric field driven relaxation with the post illustrated in Fig. 20. As we noted in our discussion on unhooking from a single post, the ends of the DNA during the unhooking process are not under tension and tend to be relaxed. For very small post spacings, the coil thus formed may be too large to fit through the downfield gap. This leads to a "bunching instability," where the electric field drives the extended portion of the chain toward an ever-growing coil at the front end (Deutsch, 1988; Deutsch and Madden, 1989; Shaffer and de la Cruz, 1989). Eventually, there is sufficient DNA in the coil to form a new hairpin and the process repeats. Simulations indicate that the mobility in the geometrative regime is no longer a function of molecular weight (Deutsch, 1988; Deutsch and Madden, 1989; Shaffer and de la Cruz, 1989), consistent with what we observe in gel electrophoresis under the same conditions.

[7]Calladine *et al.* (1991) also proposed a geometrationlike model where the accumulating DNA creates a force that eventually bends the gel and allows the DNA to pass. This model is unlikely to be applicable to the post arrays since the "gel" in this case is a rigid substrate.

TABLE II. Prefactors for mobility (c_1) and dispersivity (c_2) in Eq. (56) for different unraveling models. The first two lines correspond to the results obtained by Popelka *et al.* (1999).

Unraveling model	Mobility μ/μ_0	Dispersivity $D^*/\mu_0 E\mathcal{L}$
Random	4/9	14/2187
Preaveraged	2/5	1/125
None	2/3	1/27

Popelka *et al.* (1999) provided a simple three-step model for geometration that permits an analytical solution for both the effective mobility μ and the dispersivity D^*. In the first step, the chain unravels around the obstacle with each arm extending at a constant rate. This time is either a random variable that depends on the time to unravel the long arm at a rate $\mu_0 E$,

$$t_1 = \frac{\mathcal{L} - \chi_1}{\mu_0 E}, \tag{55}$$

or treated in a "preaveraged" sense as $t_1=\mathcal{L}/\mu_0 E$. The unhooking time t_2 is given by Eq. (33), leading to a chain completely extended on one side of the post. The front of the chain is presumably immobilized by a gel fiber (obstacle) located a distance $\mathcal{L}$ downfield. In the third step, the electric field drives the rear of the chain into its front during a time $t_3=\mathcal{L}/\mu_0 E$.

The geometrative velocity is not a function of length—the chain travels a distance $\mathcal{L}$ and the time for each step in the process scales as $\mathcal{L}/\mu_0 E$. Assuming that the initial length of the short arm is uniformly distributed, the electrophoretic mobility and dispersivity of the chain adopt the forms

$$\mu = c_1 \mu_0 \quad \text{and} \quad D^* = c_2 \mu_0 E \mathcal{L}. \tag{56}$$

The coefficients c_1 and c_2 for the two geometration models of Popelka *et al.* (1999) are listed in Table II. A geometrative mechanism is clearly a poor choice for separating long DNA because the mobility is independent of molecular weight and the dispersion increases as the DNA becomes longer.

Based on the experimental data of Randall and Doyle (2006) reproduced in Fig. 15, we should also consider the case where the sum of the unraveling and unhooking times is given by Eq. (33). We simply follow the same derivation as Popelka *et al.* (1999) and set $t_1=0$. As indicated in Table II, the latter model predicts higher velocities and less dispersion than models with unraveling since the duration of a given collision is shorter. Nevertheless, the mobility remains independent of molecular weight.

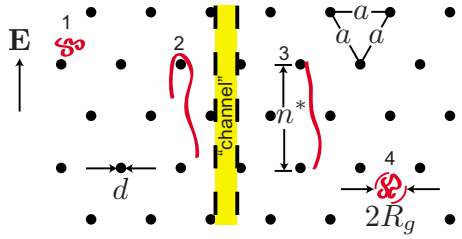

FIG. 21. (Color online) Schematic of a continuous-time random-walk model for DNA electrophoresis in a post array. The numbers indicate different points in time during the cyclic process. The hexagonal array has a center-to-center spacing a and post diameter d. The DNA radius of gyration R_g is indicated. The excluded row parameter n^* is defined in Eq. (57). The role of the highlighted channel in a sparse array is discussed in Sec. IV.A.4.

3. Continuous-time random-walk model

As the array density decreases, there is no reason why an unhooking chain will necessarily interact with the post immediately downfield from its leading end. Indeed, for the relatively sparse array shown in Fig. 21, there is sufficient space for the chain to completely coil in the interstices. Minc, Viovy, and Dorfman (2005) proposed an extension to the geometration model that could account for the sparseness of the array. The first two steps of this model are the same as geometration: preaveraged unraveling around the post followed by a rope-over-pulley disengagement. At the end of this process, the chain has some extension $\mathcal{L}^{\text{eff}}$. As a result, there are

$$n^* = \mathcal{L}^{\text{eff}}/a \tag{57}$$

rows of posts along the chain backbone that are unavailable for collisions. For example, the unhooking DNA in Fig. 21 cannot collide with the $n^*=2$ posts immediately downfield from the previous collision. In this model, the probability of colliding with a post in row $n>n^*$ away from the previous collision is given by the constant value Π_c. Eventually the DNA collides with another post and the cycle begins again.

This model of the transport process (Minc, Viovy, and Dorfman, 2005) is a partially separable continuous-time random walk. Scher and Lax (1973) obtained a general solution to the random walk in terms of the probability density $\psi(n,t)$ that one pass through the cycle leads to translation over a distance of n rows in a time t. Taking advantage of this solution, Minc, Viovy, and Dorfman (2005) derived the effective mobility

$$\frac{\mu}{\mu_0} = \frac{2(\Pi_c n^* + 1 - \Pi_c)}{5\Pi_c n^* + 2(1-\Pi_c)} \tag{58}$$

and the dispersivity

$$\frac{D^*}{\mu_0 Ea} = \frac{\Pi_c (n^*)^2[10 + \Pi_c(2n^* - 11) + (1-n^*)^2\Pi_c^2]}{[5\Pi_c n^* + 2(1-\Pi_c)]^3}. \tag{59}$$

If we neglect the unraveling time, motivated by the experimental data reproduced in Fig. 15, then the numerical prefactors are slightly different (Mohan and Doyle, 2007b),

$$\frac{\mu}{\mu_0} = \frac{2(\Pi_c n^* + 1 - \Pi_c)}{3\Pi_c n^* + 2(1-\Pi_c)} \tag{60}$$

and

$$\frac{D^*}{\mu_0 Ea} = \frac{\Pi_c (n^*)^2[2 + \Pi_c(2n^* - 3) + (1-n^*)^2\Pi_c^2]}{[3\Pi_c n^* + 2(1-\Pi_c)]^3}. \tag{61}$$

Note that the geometration results are recovered for the respective unraveling models (preaveraged and none) for $\Pi_c=1$ and $\mathcal{L}^{\text{eff}}=\mathcal{L}$. Like the models for the single-post limit, these continuous-time random-walk models predict that the mobility decays monotonically with molecular weight.

One immediate concern in this model is the assumption that the collision in a post array is identical to a single post. Minc, Bokov, *et al.* (2005) addressed this question for T4-DNA in different magnetic bead arrays. The trapping time in the array tends to agree well with the single-post model. For all of the arrays studied, the DNA appears to only form a single hairpin during their collision. The collision time distribution for a given electric field decays exponentially, and the average collision time scales as E^{-1}. All of these data lend support to using an isolated post-collision model, at least at the scaling level.

In order to have any predictive power, we also need to have model equations for $\mathcal{L}^{\text{eff}}$ and Π_c. At the minimum, the collision probability should depend on the density of the obstacles and/or the size of the DNA. Thus, we can consider using $\Pi_c=d/a$ (Dorfman and Viovy, 2004; Minc, Viovy, and Dorfman, 2005) or $\Pi_c=R_g/a$ (Mohan and Doyle, 2007b). These are crude approximations to the true collision probability, but they represent an attractive starting point for modeling the overall transport process.

The models for the chain extension during the unhooking process are better grounded than the collision frequency models. In the original incarnation of the model, Minc, Viovy, and Dorfman (2005) assumed that the chain was fully stretched so that $\mathcal{L}^{\text{eff}}=\mathcal{L}$. However, we saw in Sec. III.A.4 that the extension of the chain should be a function of the electric field. Two different models have tried to capture the lower-field regime: (i) Dorfman (2006, 2008) proposed using the stem-flower conformation given by Eq. (38) and (ii) Mohan and Doyle (2007b) suggested that the wormlike chain extension of Eq. (37) is more appropriate. In general, the incomplete extension of the chain in the continuous-time random-walk model tends to accentuate the difference

in mobility between longer and shorter DNA. This is consistent with the observations of Doyle *et al.* (2002) in magnetic bead arrays.

While we can imagine many permutations of Eqs. (58)–(61) with the various models for $\mathcal{L}^{\text{eff}}$ and Π_c, there are no definitive experimental data that would allow us to distinguish which (if any) of these models actually describe DNA electrophoresis in a post array. Simulation data in geometries reminiscent of the magnetic bead array are reasonably well approximated in Eqs. (60) and (61) with the wormlike chain mode and $\Pi_c = R_g/a$ (Mohan and Doyle, 2007b). However, these simulations use a spatially uniform electric field. As we will see in the upcoming section, it is unlikely that these simulations reflect the experimental data that one would obtain in a similar experimental system (Doyle *et al.*, 2002; Minc *et al.*, 2004; Minc, Bokov, *et al.*, 2005; Ou *et al.*, 2009). For very sparse arrays the perturbations to the electric field in a sparse system are localized near the posts. We would expect the uniform-field simulation data of Mohan and Doyle (2007b) to be a more accurate reflection of these experiments (Ou *et al.*, 2010).

4. The "channeling" hypothesis

The models discussed thus far are essentially mean-field approaches to understanding DNA electrophoresis in post arrays. We express the collision probabilities in terms of the geometric parameters of the system (d and a) or the size of the DNA (R_g), but at no point did we consider how the particular arrangement of the posts affects the transport process.

From a fabrication standpoint, the most convenient array geometries are periodic ordered matrices with features on the micron scale. However, Brownian dynamics simulations of the electrophoresis in such ordered arrays suggested a potential problem (Patel and Shaqfeh, 2003; Mohan and Doyle, 2007a, 2007b). As shown in Fig. 21, ordered arrays feature a "channel" of characteristic size $(a-d)/2$. If the electric field is strong, then the DNA could simply be convected over long distances through these post-free regions before they have sufficient time to diffuse laterally and align with a post. The role of post order on the simulated transport is most clearly illustrated by Brownian dynamics simulations of DNA electrophoresis in magnetic bead arrays as a function of the applied magnetic field (Mohan and Doyle, 2007a). The simulated mobility and dispersivity undergo a sharp transition when the magnetic field strength causes the magnetic bead array to undergo a disorder-order transition.

Experimental data in the array shown in the inset of Fig. 22 do not support the channeling hypothesis. If channeling occurs, we would expect to see the mobility and dispersivity approach their free-solution values as the electric field increases (Mohan and Doyle, 2007b). However, experiments in ordered arrays similar to those simulated by Mohan and Doyle (2007b) lead to dispersivities that are linear in the electric field and orders of magnitude higher than the molecular diffusivity. The latter results are consistent with the predictions of Eqs. (52), (54), (59), and (61). The failure of the channeling hypothesis in these arrays lies in the nonuniform electric field engendered by the insulating posts. As shown in Fig. 22, Brownian dynamics simulations using a uniform field overestimate the electrophoretic mobility. When a nonuniform field is included in the simulations, the simulations are in much closer agreement with the experimental data.

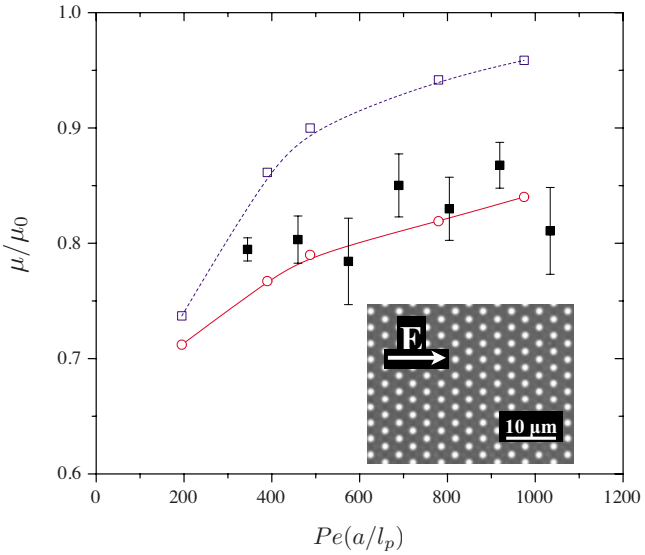

FIG. 22. (Color online) Electrophoretic mobility as a function of the electric field in an array of 1.2 μm diameter PDMS posts in a hexagonal array with spacing $a=3$ μm. The solid squares correspond to the experimental data, the circles correspond to Brownian dynamics simulations using a nonuniform electric field, and the open squares correspond to Brownian dynamics simulations using a uniform electric field. Data from Ou *et al.*, 2009.

Channeling should occur for sufficiently large-post spacing because the electric field gradients due to the presence of the post decay with distance. The critical post spacing to avoid channeling is not clear. For example, Saliba *et al.* (2006) obtained high-resolution separations of λ, 2λ, and T4-DNA in 2 min using $d=2.6$ μm diameter posts in a hexagonal array with $a=7$ μm. In contrast, Ou *et al.* (2010) showed that λ-DNA will channel through the array when the post diameter is decreased to 1 μm at the same spacing. The latter study further demonstrated that the onset of channeling is a gradual process.

5. Working across regime boundaries with nanoposts

The crossover between geometration and the continuous-time random-walk models depends on both the molecular weight of the DNA and the geometry of the array. This opens up the possibility of exploiting different migration mechanisms to separate two different sized DNA. For the model binary mixture of λ-DNA and T4-DNA, the change in migration mechanism may explain the spectacularly fast separations in nanopost arrays (Kaji *et al.*, 2004; Chan *et al.*, 2006; Ogawa *et al.*,

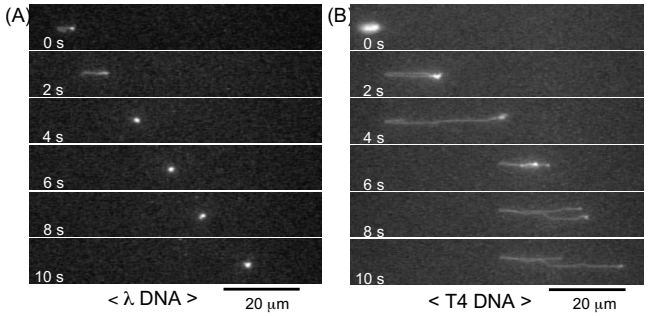

FIG. 23. Videomicroscopy images of λ-DNA and T4-DNA in a nanopost array under an electric field of 7 V/cm. From Kaji *et al.*, 2004.

2007; Shi *et al.*, 2007). The latter arrays generally feature posts and gap sizes in the submicron regime, reaching as low as 300 nm. In the best results reported to date, Kaji *et al.* (2004) separated λ-DNA and T4-DNA in only 15 s using a very strong electric field and a hexagonal array with $d=500$ nm and $a=1$ μm. Other experiments on nanopost arrays reported separations in the minute range (Chan *et al.*, 2006; Shi *et al.*, 2007). As seen in the videomicroscopy data of Kaji *et al.* (2004), the smaller λ-DNA tends to move through the system in its coiled conformation. Occasionally, the λ-DNA collides with one of the obstacles and forms a rope-over-pulley conformation. In contrast, the larger T4-DNA exhibits a geometrativelike motion.

The models presented thus far fail to capture these experimental data. To see why, we first recall that the continuous-time random-walk theory has been formulated so that it approaches geometration as the collision probability $\Pi_c \to 1$. In any of the models for n^* and Π_c presented thus far, the quantity $(1-\Pi_c)/\Pi_c n^*$ is a small parameter. The resulting continuous-time walk mobility μ_{CTRW} is thus a perturbation of the geometrative mobility μ_{geo},

$$\mu_{\mathrm{CTRW}} \approx \mu_{\mathrm{geo}}\left[1 + c\left(\frac{1-\Pi_c}{\Pi_c n^*}\right)\right], \tag{62}$$

where $c=3/5$ for Eq. (58) and $c=1/3$ for Eq. (60). The failure of the extant models to capture the nanopost data lies in the simplistic models used to predict the distance between collisions. After coiling, the models $\Pi_c = d/a$ and R_g/a predict that λ-DNA will travel, on average, approximately 1 μm in the coiled form prior to the next collision. These predictions do not agree with the data in Fig. 23, which show that λ-DNA can move many microns between collisions.

We could greatly advance our understanding of the dynamics of DNA in nanopost arrays through systematic single-molecule experiments along the lines of those performed by Randall and Doyle (2004, 2005a, 2006) for an isolated obstacle. However, nanopost arrays are considerably more challenging to fabricate than a single post in a PDMS channel. Hopefully, devices such as the ones produced by nanoimprint lithography (Austin, Tegenfeldt, *et al.*, 2002; Shi *et al.*, 2007) or nanosphere lithography (Kuo *et al.*, 2008) will lower the barrier to performing such experiments.

6. Role of the electric field strength

While we have focused for the most part on the role of the array density, the electric field strength also plays an important role in the transport through the array. We first consider the case where the electric field is strong enough to lead to hairpin formation and rope-over-pulley dynamics. Both our single-post and continuous-time random-walk models make the same predictions about the role of the electric field. Explicitly, by assuming that the collision frequency is independent of the electric field, these models predict that the mobility is independent of E and the dispersivity scales linearly with E. In principle, we could operate the device at the highest permissible electric field and still obtain the same resolution between the peaks at a reduced time (Dorfman and Viovy, 2004).

Both the collision frequency assumption and concomitant resolution predictions have been tested experimentally. Single-molecule experiments indicate that the collision frequency is not well correlated with the electric field strength (Minc, Bokov, *et al.*, 2005), lending some credence to the assumption $\Pi_c \sim E^0$. The resolution prediction does not appear to be as robust. Experiments in magnetic bead arrays confirm that the resolution is independent of electric field strength for moderate electric fields (Minc *et al.*, 2004). However, the resolution is not as high for $E<15$ V/cm and appears to decay for $E>30$ V/cm as well (Minc *et al.*, 2004). Patel and Shaqfeh (2003) also observed a similar decay in the resolution at high electric fields during Brownian dynamics simulations in random arrays of point-sized posts. With the help of the conversion factor [Eq. (29)], we estimate that their simulations range from 8.3 to 83 V/cm; Patel and Shaqfeh (2003) remarked that the resolution generally improved as the electric field decreased.

Minc *et al.* (2004) suggested that the lower resolution at weak electric fields is probably due to incomplete stretching of the chain during collisions and more frequent roll-off collisions. Brownian dynamics simulations have provided a more detailed picture of the transport in a weak electric field, demonstrating the existence of a minimum in the electrophoretic mobility. The location of the minimum differs depending on the details of the simulation; Patel and Shaqfeh (2003) reported a minimum around $\mathrm{Pe}=10$ while the minimum of Mohan and Doyle (2007b) occurs for $\mathrm{Pe}\approx 1$. These Péclet numbers represent a balance between the chain relaxation and the hairpin formation time and thus an optimum combination of collision frequency (due to the relaxation of the chain between collisions) and hairpin formation during collisions (Patel and Shaqfeh, 2003). At higher electric fields, the chains do not relax as quickly and make fewer collisions per unit distance. At lower electric

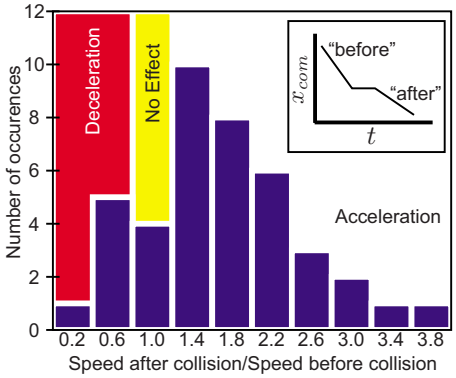

FIG. 24. (Color online) Histogram of the relative electrophoretic velocity before and after collisions of T4-DNA in a magnetic bead array at a macroscopic electric field E =26.8 V/cm. The inset is a schematic of a trajectory of a DNA molecule's center of mass x_{com} as a function of time. The speed before the collision is computed from the slope of the trajectory prior to the plateau (the collision); the speed after the collision is computed from the slope of the trajectory after the plateau. Adapted from Minc, 2005.

fields, the chains can collide with the post but do not easily form hairpins. Indeed, the dispersion at very low electric fields resembles Ogston sieving (Mohan and Doyle, 2007b). However, the scaling $D^* \sim E^{1.3}$ obtained from Brownian dynamics simulations of DNA in a random array of obstacles (Mohan and Doyle, 2007b) differs from the prediction $D^* \sim E^2$ produced by an exactly solvable Ogston sieving model of diffusion in a random array (Gauthier and Slater, 2003).

7. Acceleration after a collision

While the unhooking process in the magnetic bead arrays seems to be well described by the single-post model, at least at the scaling level, Minc, Bokov, *et al.* (2005) observed that the electrophoretic velocity of the DNA following a post collision tends to be higher than the incoming velocity. As shown in Fig. 24, the velocity ratio distribution is relatively broad, with a nontrivial fraction of the DNA exiting the post at a lower speed than they had prior to the collision. Moreover, the deviation between the incoming and outgoing velocities is much larger than the 10% difference observed during collisions with an isolated obstacle (Randall and Doyle, 2006). The acceleration phenomenon may be a major reason why the dispersion in the experimental systems is much less than predicted by the variation in the collision times with a single post.

The origin of this "acceleration" effect is not entirely clear. At first glance, it is tempting to attribute the higher outgoing velocity to hydrodynamic interactions. We already saw in Fig. 12 how the lower friction at the relaxed end of an unhooking chain can lead to a decrease in the hold-up time when hydrodynamic interactions are included in the model. Indeed, Minc, Bokov, *et al.* (2005) noted that the average value of the distribution in Fig. 24 is almost identical to the ratio of the hydrodynamic mobility of a cylinder and a sphere in free solution. However, these explanations run counter to the free-draining behavior of DNA in free solution. Although hydrodynamic interactions may play a role during the unhooking process (Long *et al.*, 1996; André *et al.*, 1998), it would seem that these interactions would not affect the motion of the DNA in free solution. However, the DNA does not sample the full configuration space. As noted previously, the screening of hydrodynamic interactions for a given configuration is different from its average over all conformations (at least for an isotropic particle) (Long and Ajdari, 2001).

We can also consider another possibility related to the conformation of the DNA. The electrophoretic velocity in the distribution is measured in the direction of the average motion (i.e., down the channel). When the DNA is in its coiled state and approaching the post, it may need to wend its way around the obstacles due to the finite size of both the DNA and the array. This tortuous path would lead to an "in array" mobility lower than the free-solution mobility in an empty channel (Minc, Viovy, and Dorfman, 2005). After the collision, the highly extended chain is narrow and thus able to move freely through the gaps between the posts. It is difficult to rule out this explanation from the data on electrophoresis in quasiordered magnetic bead arrays. Similar experiments in an ordered array would be much easier to interpret.

The nonuniform electric field provides a third possible explanation of the acceleration effect. We have already noted in Sec. IV.A.4 that the electric field lines are curved in an array of insulating obstacles. The electric field lines are compressed in the gaps between the obstacles, leading to a higher local electric field therein. It is possible that the extended DNA molecule exiting the post is biased toward the higher electric field regions of the array. In contrast, the coiled configuration before a collision tends to sample all of the electric field strengths.

B. Large posts

1. Not exactly Ogston sieving

We now turn our attention on arrays of large posts. What qualifies as "large" depends on the size of the DNA and the geometry of the post; we take as an operational definition that a collision between DNA and a large post does not lead to hairpin formation and rope-over-pulley dynamics. Such arrays can separate DNA using a mechanism analogous to size-exclusion chromatography (Baba *et al.*, 2003). From a more fundamental perspective, regular arrays of large posts provide the ideal test bed for the exactly solvable Ogston sieving model proposed by Slater and co-workers (Slater and Guo, 1996a, 1996b; Slater and Treurniet, 1997; Mercier and Slater, 1998, 2001; Labrie *et al.*, 2000; Boileau and Slater, 2001; Mercier *et al.*, 2001; Gauthier and Slater, 2002, 2003; Gauthier *et al.*, 2004). The latter models were developed to describe gel electrophoresis of small globu-

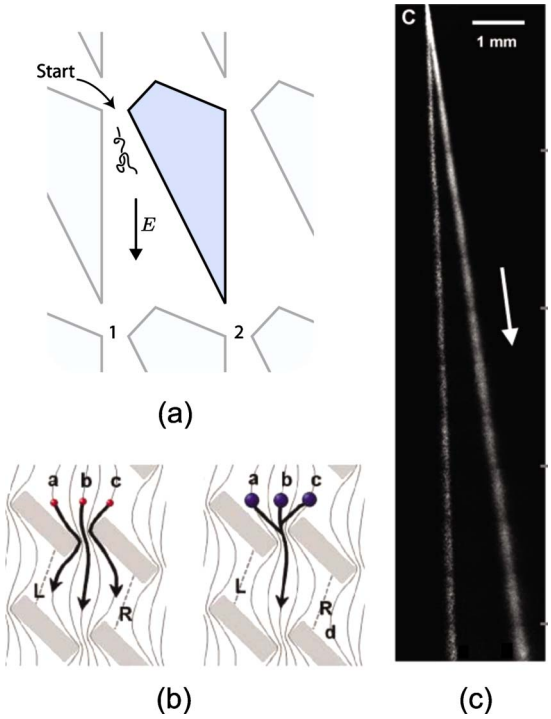

FIG. 25. (Color online) Brownian ratchet separation in a post array. (a) Schematic illustration of the principle behind the separation. (b) Illustration of the transport of a small (left) and large (right) particles approaching the gap between the obstacles. (c) Separation of λ and T2 (164 kbp) DNA in an optimal system. (a) From Ertas, 1998 by Michel Gauthier, (b) from Huang, Silberzan, *et al.*, 2002, and (c) from Huang *et al.*, 2003.

lar particles. They idealize the gel as a periodic array of impenetrable obstacles on a regular lattice. The mobility and dispersivity of a particle moving on this lattice are computed using Monte Carlo moves based on the first-passage time for jumps between adjacent lattice sites. While these Ogston sieving models only approximate the structure of a gel, they closely resemble a dilute array of large posts.

While testing these lattice models would be of fundamental interest, we can do even more interesting things with arrays of large obstacles if they are arranged asymmetrically and the electric field is applied at an angle with respect to the lattice vectors of the array. There are many possible ways to accomplish this goal; one such geometry is shown in Fig. 25(a). The first attempts to elucidate the mechanism of such a separation were published in back-to-back papers by Ertas (1998) and Duke and Austin (1998). The latter works rely on the concept of a Brownian ratchet. With the geometry of Fig. 25(a), the particle enters at the top of the highlighted region. In these models, all of the DNA is convected at a uniform rate $\mu_0 E$ in the downward direction while diffusing laterally with a size-dependent molecular diffusivity D. At the bottom of the region, the particle takes the branch either toward direction 1, which leads to no deflection, or toward direction 2, which leads to deflection perpendicular to the electric field. The probability of branching depends on the diffusivity of the particle. From Eq. (18), we would conclude that smaller molecules having a higher probability of reaching branch 2 than their larger counterparts. The overall process is a series of such branches that ultimately leads to different sized DNA moving at different angles with respect to the electric field.

Through a series of ever-improved device designs (Chou *et al.*, 1999; Cabodi, Chen, *et al.*, 2002; Huang, Silberzan, *et al.*, 2002; Huang *et al.*, 2003), Austin and co-workers demonstrated the robustness of the Brownian ratchet separation device.[8] As shown in Fig. 25(c), their final device design achieved a remarkable separation of large DNA. Moreover, since the device is based on DNA moving at different angles, it can operate in a continuous mode.

Although this geometry does, in fact, separate DNA by size, the mechanism behind the separation is not as simple as the models originally proposed by Ertas (1998) and Duke and Austin (1998). The latter models feature a point-sized particle convecting with a spatially uniform electrophoretic velocity $\mathbf{v}=\mu\mathbf{E}$. In the long-time limit, such a system will lead to all particles moving in the same direction because the velocity field is solenoidal, $\nabla\cdot\mathbf{v}=0$, and the normal component of the electric field is zero, $\mathbf{n}\cdot\nabla\phi=0$ (Austin, Darnton, *et al.*, 2002; Li and Drazer, 2007). If the electrophoretic mobility was somehow dependent on position, say via wall effects (Dorfman and Brenner, 2002), or if the obstacles were not perfectly insulating (Austin, Darnton, *et al.*, 2002), we could have directional separation because the local velocity vector $\mathbf{v}$ is no longer proportional to the electric field $\mathbf{E}$ at all points in space.

In the course of arriving at the device producing the separation in Fig. 25(c), Huang, Silberzan, *et al.* (2002) determined the two key design parameters for a successful separation. First, the equipotential lines need to be parallel to the rows of obstacles so that the periodicity of the nonuniform field is identical to the obstacle lattice. This task is accomplished by tilting the electric field at the inlet. Second, the gaps between obstacles need to be commensurate with the size of the DNA. As shown in Fig. 25(b), small molecules tend to simply move along an electric field line as they pass through the gap. In contrast, the obstacles exert a significant effect on larger molecules. Even if the molecules were on distant electric field lines during their approach, the compression of the electric field lines in the gap tends to leave them on a common electric field line as they enter the next unit cell. The ensuing dynamics are thus similar to the ratchet model. While our theoretical understanding remains incomplete, the experimental evidence (Huang,

[8]van Oudenaarden and Boxer (1999) also produced a similar ratcheting device for charged lipids in a lipid bilayer. Since the obstacles are fluid (and thus conducting), the separation occurs by the ratcheting mechanism described in the previous paragraph (Austin, Darnton, *et al.*, 2002).

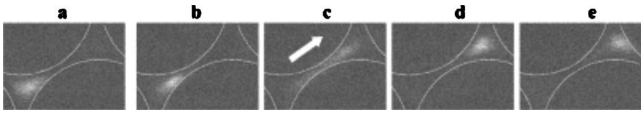

FIG. 26. Videomicroscopy data for λ-DNA moving in a hexagonal array of 10 μm high, 15 μm diameter PDMS pillars with a minimum separation distance of 1 μm under a nominal electric field of 50 V/cm. The post boundaries, which do not appear in fluorescence, are added for clarity. From Inatomi *et al.*, 2003.

Silberzan, *et al.*, 2002; Huang *et al.*, 2003) leaves no question that the separation works.[9]

2. Entropic trapping

As the large posts are placed closer together, it is possible to reach a geometry that leads to the entropic trapping dynamics discussed in Sec. II.B.3. We will see in Sec. V.A that the slit-well motif is an ideal geometry for entropic trapping. However, it is possible to observe entropic trappinglike behavior in a tight array of large obstacles. Figure 26 reproduces videomicroscopy data for λ-DNA moving through a hexagonal array of tightly spaced pillars. The entropic penalty for λ-DNA is small since its radius of gyration (730 nm) is not much larger than the half width of the gap (500 nm). The corresponding entropic penalty for T4-DNA to move through the gap is larger. From videomicroscopy data, Inatomi *et al.* (2003) found that the mobility of λ-DNA is slightly higher than T4 (relative mobility of 1.2) with a significant spread in the T4 mobility distribution. These data are consistent with the weak entropic trapping effect that we would expect to observe in this system.

Dense arrays of small posts also can be arranged in an asymmetric configuration to provide a continuous separation by entropic trapping (Fu *et al.*, 2007). Figure 27 shows the details of a second-generation device for these separations (Mao and Han, 2009). The device is configured so that there are relatively wide channels (running in the vertical direction in the upper-right inset) that are periodically connected to one another by narrow channels. The net electric field is applied at an angle with respect to the symmetry axes of the array, leading to occasional jumps between wide channels by the DNA. The jump rate is governed by the physics of entropic trapping if the DNA is long and the slits are small. It is also possible to use devices such as the one in Fig. 27 to continuously separate DNA by size exclusion or charge exclusion by changing the size of the DNA, the buffer composition, and the size of the slits (Fu *et al.*, 2007).

[9]Similar geometries produce even better separation devices under a pressure-driven flow (Huang *et al.*, 2004). Here, although the hydrodynamic fluid flow satisfies $\nabla\cdot\mathbf{v}=0$ and $\mathbf{v}=\mathbf{0}$ on the solid boundaries, the particles are certainly not freely draining and their hydrodynamic mobilities depend on position. These separations do not appear to depend at all on the diffusivity of the particles.

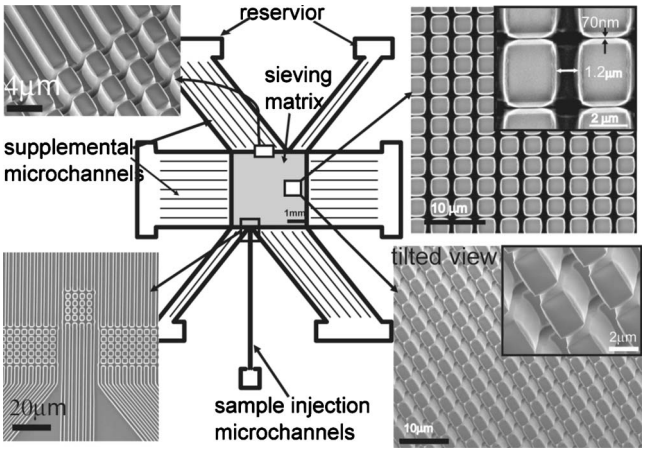

FIG. 27. Second-generation anisotropic array for continuous separation by entropic trapping, size exclusion, or electrostatic exclusion. The insets show different portions of the device and different zoom levels. The gaps between the posts are different in the vertical and horizontal directions. By applying the average electric field at an angle to the lattice vectors of the array, the DNA moves freely in the vertical direction but can make horizontal jumps. Depending on the size of the gap, the jump frequency is due to entropic trapping, steric hindrances, or charge exclusion (see Sec. V). From Mao and Han, 2009.

Since different sized DNA will tend to jump between wide channels with different frequencies, they tend to move at different net angles with respect to the applied electric field. This system thus produces a directional separation analogous to what is observed in the Brownian ratchet in Fig. 25.

3. Reptation (for small and large posts)

We conclude our discussion of constant electric field electrophoresis in post arrays with some comments on reptation in these systems. We already discussed the principle of reptation in Sec. II.B. As shown in Fig. 19, we would expect reptation to occur in a post array if the gaps between the posts are small compared to the radius of gyration of the DNA. We need to further restrict ourselves to large posts for $\mathrm{Pe}>1$. Hairpin formation around small posts should occur at higher electric fields and break the biased reptation.

As noted in the context of Fig. 19, it is challenging to fabricate arrays that would exhibit biased reptation. Kuo *et al.* (2008) explored the use of nanosphere lithography to create dense nanopost arrays. Their devices featured gaps as small as 50 nm, which is commensurate with the persistence length of double-stranded DNA. Under a strong electric field of 50 V/cm, Kuo *et al.* (2008) indeed observed head-on reptative motion of the DNA. They also observed some entropic trapping events under a weaker electric field of 5 V/cm, which may be due to defects in the array during the nanosphere lithography step.

Remarkably, Ogawa *et al.* (2007) and Yasui *et al.* (2007) also reported similar head-first dynamics for T4 in square arrays of 500 nm diameter pillars with a gap of

500 nm, which do not represent very strong confinement. Chan *et al.* (2009) observed similar dynamics in square arrays of rectangular obstacles. We might expect to see hooking in these arrays since the posts are small. However, the nanopillar arrays used for these experiments consist of alternating periods of 215 nm (Yasui *et al.*, 2007) or 500 nm (Ogawa *et al.*, 2007) diameter pillar regions followed by 35 μm long pillar-free regions. It is likely that the residence time in the pillar region is too short for the DNA to relax, especially since the pillar regions are only a few times the contour length of T4-DNA.

C. Pulsed electric fields

The utility of post arrays for DNA separations is not limited to constant electric fields. Indeed, we will see here that some of the most remarkable post array separations have been achieved using pulsed electric fields (Bakajin *et al.*, 2001; Huang, Tegenfeldt, *et al.*, 2002). The physics underlying these separations are markedly different from the hairpin formation and rope-over-pulley collisions discussed thus far.

1. The switchback mechanism

The first approach to using pulsed electric fields in post arrays was a direct miniaturization of the contour-clamped homogeneous electric field method of pulsed-field gel electrophoresis (Chu *et al.*, 1986; Clark *et al.*, 1988) by Austin and co-workers (Duke *et al.*, 1996; Bakajin *et al.*, 2001). In this process, a uniform electric field periodically switches between two directions, with the angle θ between the two electric fields being obtuse. Work on gel electrophoresis established that the mobility of the bands is essentially independent of the angle for $105° \leqslant \theta \leqslant 165°$ (Birren *et al.*, 1988). Typical gel electrophoresis separations, as well as the proof-of-principle separations in post arrays (Bakajin *et al.*, 2001), use $\theta = 120°$.

Owing to the precise structure of the post array, we would expect the physics to be simpler to describe than in the heterogeneous medium of a gel. Duke *et al.* (1996) modified Southern's switchback mechanism for gel electrophoresis (Southern *et al.*, 1987) to develop the model for pulsed-field electrophoresis in a post array shown in Fig. 28. In the switchback mechanism, each time the electric field changes direction the "head" and the "tail" of the chain exchange roles. In the original version of this model, the chain moves at a constant velocity. In this modified version, the chains first reorient via biased reptation (Slater and Noolandi, 1989) and then proceed in the direction of the electric field with constant velocity $\mu_0 E$.

To simplify the transport process, it is desirable for the chain not to switch between "channels" of the post array during the constant velocity phase. This can be accomplished by using a sufficiently strong electric field. If we imagine the channel between posts to be a tube of size

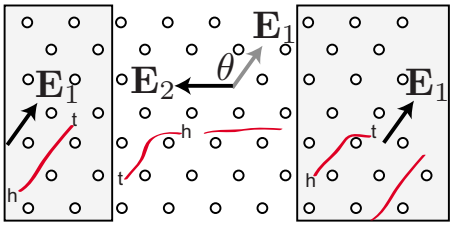

FIG. 28. (Color online) Schematic illustration of the switchback mechanism in a post array. The gray shaded region corresponds to the electric field direction $\mathbf{E}_1$ and the clear region corresponds to an electric field rotated by the angle θ. The symbols h and t refer to the head and tail of the chain for a given electric field direction.

$a/2$, the segment diffusion time is (Doi and Edwards, 1988)

$$t_d = (a/2)^4(\xi_k/k_B T l_k^2). \tag{63}$$

This time needs to be long compared to the time $2a/\mu_0 E$ required for convection from post to post. This leads to the critical electric field (Duke *et al.*, 1996)

$$E/E_0 \gg 32(l_k/a)^3, \tag{64}$$

where $E_0 = k_B T/\mu_0 \xi_k l_k$ is the electric field where convection and diffusion balance on the Kuhn length scale.

As shown in Fig. 28, the DNA needs to turn the corner when the electric field changes to begin moving in the new electric field direction. Duke *et al.* (1996) posited that this reorientation time should be equal to the biased-reptation reorientation time (Slater and Noolandi, 1989),[10]

$$t_{or} = c_1 N_k (E_0/E)\tau_B, \tag{65}$$

where $c_1 = \ln(1/|\cos\theta|)/(1-|\cos\theta|)$ is a constant and $\tau_B = \xi_k l_k^2/k_B T$ is the diffusive time scale for a Kuhn segment. For a pulse time t_p, the chain can reorient as long as it is less than the critical length

$$N_k^* = \left(\frac{t_p}{\tau_B}\right)\left(\frac{E}{E_0}\right)\left(\frac{1}{c_1}\right). \tag{66}$$

Chains of length $N_k < N_k^*$ will thus spend the fraction of the pulse time $1 - t_{or}/t_p$ moving along the electric field direction with a speed $\mu_0 E$. For a square pulses in time, the net motion is along the bisector of the angle θ with effective mobility

$$\frac{\mu}{\mu_0} = \left(1 - \frac{N_k}{N_k^*}\right)\cos\left(\frac{\theta}{2}\right), \tag{67}$$

implying a linear fractionation with respect to molecular weight (Duke *et al.*, 1996).

The qualitative features of this theory are captured in the experiments of Bakajin *et al.* (2001), who used a hexagonal array of 2 μm pillars with a 2 μm gap to separate

[10]To arrive at this result, Duke *et al.* (1996) assumed that the primitive segment of the chain of Slater and Noolandi (1989) contains a/l_k Kuhn segments.

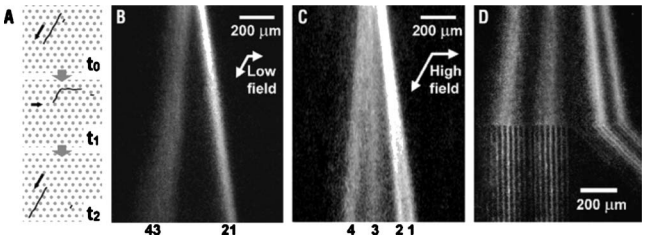

FIG. 29. Continuous separation in the DNA prism. (a) Schematic illustration of the separation mechanism for a DNA prism. (b)–(d) Separation results for (1) 61, (2) 114, (3) 158, and (4) 209 kbp in a hexagonal array of 2 μm diameter posts with a gap of 2 μm. Image (b) corresponds to 250 ms square pulse of 32 and 20 V/cm alternating at 2 Hz. Images (c) and (d) correspond to 40 ms square pulses of 240 and 150 V/cm alternating at 12.5 Hz. From Huang, Tegenfeldt, *et al.*, 2002.

λ and T4-DNA. The array geometry naturally suggested an angle $\theta=120°$ so that the electric field directions point along the lattice vectors of the array. The separation reached baseline in around 10 s, which is comparable to the speed achieved by Kaji *et al.* (2004) in a nanopost array. This impressive separation took advantage of a precise loading and injection scheme based on entropic trapping (Han and Craighead, 1999). However, the theory fails to quantitatively describe the separation most likely due to incomplete extension of the chain (Bakajin *et al.*, 2001).

While both the nanopost array (Kaji *et al.*, 2004) and the switchback device (Bakajin *et al.*, 2001) led to baseline resolution of λ and T4-DNA in a matter of seconds, the pulsed-field separation device of Bakajin *et al.* (2001) is the more robust separation method. In the pulsed-field device, all of the DNA is moving by the same mechanisms and the mobility difference depends linearly on the difference in molecular weight. In contrast, we speculated in Sec. IV.A.5 that the nanopost array separation was the result of λ-DNA and T4-DNA moving by two different mechanisms. Thus, it is not clear that the nanopost array will work as well as a pulsed-field device for separating arbitrary mixtures, especially if the DNA has similar molecular weights.

2. DNA prism

In the separations of the previous section, the electric field strengths and pulse times are identical. As a result, all of the DNA moves along the bisector of the angle θ, albeit with the different mobilities given by Eq. (67). If we break the symmetry of the system, by varying either the pulse strength or the pulse time, different sized DNA will not only move at different velocities but also move in different directions with respect to the net electric field. Huang, Tegenfeldt, *et al.* (2002) aptly termed their separation device based on this principle the "DNA prism." With a proper tuning of the electric field strength and pulse times, the DNA separation in Fig. 29 resembles that of light in a prism.

Based on the switchback mechanism, we can build a simple deterministic model of the DNA prism. As in Fig. 29, let a strong electric field E_1 lead to motion in the positive x direction and the weaker electric field E_2 lead to motion at an angle θ counterclockwise with respect to the positive x direction. Each of these electric fields is associated with a reorientation time t_{or} given by Eq. (65). If we assume that the reorientation time for a given direction is shorter than the pulse time, then the DNA moves with an angle,

$$\tan\phi = \frac{(N^*_{k,2} - N_k)\sin\theta}{(N^*_{k,1} - N_k) + (N^*_{k,2} - N_k)\cos\theta}, \tag{68}$$

counterclockwise with respect to the direction of the high electric field. In the latter, $N^*_{k,i}$ is the cutoff molecular weight N^*_k in Eq. (66) for the pulse with electric field strength E_i. The latter equation is valid down to $N_k = N^*_2$, after which point the DNA should move along the direction of the strongest electric field. In the low-frequency limit, reorientation is fast relative to the pulse time and all of the DNA moves along the time-averaged electric field direction.

Recent DNA prism experiments in colloidal crystals call into question this deterministic model. Using relatively small DNA (2–20 kbp) in a colloidal crystal of 330 nm silica spheres, Zeng *et al.* (2008) observed that the angular dependence on frequency is generally nonmonotonic and collapses to a molecular-weight independent value as the electric field increases. With the exception of the shortest DNA, the maximum angular deflection also appears to obey a power law with respect to molecular weight. This nonmonotonic behavior is not explained by the deterministic model (Zeng *et al.*, 2008).

3. Entropic recoil

In gel electrophoresis, it is well known that very large linear DNA or circular DNA can be trapped at the entrance of the gel if they become entangled with the dangling fibers at the edge of the gel. Both types of DNA can be driven into the gel by pulsing the electric field (Levene and Zimm, 1987; Turmel *et al.*, 1990). The pulses are not long enough to lead to significant molecular rearrangement, but they are of sufficient duration to disentangle the DNA from the protruding fibers.

Naturally, cylindrical posts cannot have protruding "fibers" that impale the DNA. However, it is still possible to clog the entrance to the array if the posts are sufficiently dense. For example, Turner *et al.* (1998) observed significant clogging of linear λ-DNA and a 7.2 kbp circular DNA in a square array of 35 nm high, 100 nm diameter pillars, with a 100 nm gap. Although that DNA that enter the array moves with different mobilities, the clogging appeared to be a critical problem for using such dense arrays for separations.

Cabodi, Turner, and Craighead (2002) showed how the clogging at the entrance can be exploited to separate different sized DNA by employing the series of pulses shown in Fig. 30. During the "drive" period of the voltage cycle, the DNA is driven into the array by the electric field. The DNA that completely enters the array re-

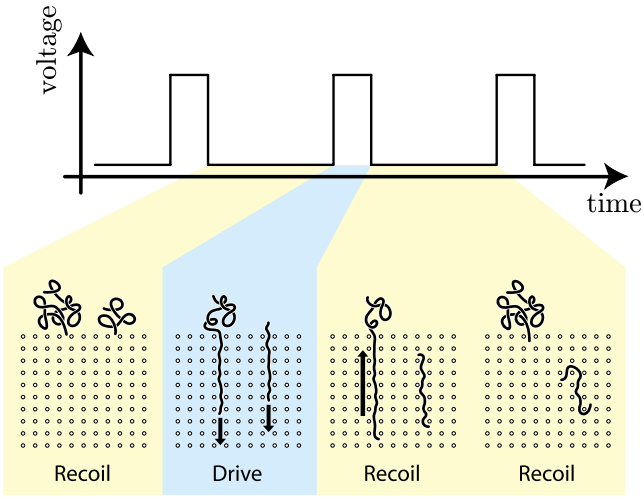

FIG. 30. (Color online) Principle behind an entropic recoil separation of different sized DNA in a dense post array under a pulsed electric field. Adapted from Cabodi, Turner, and Craighead, 2002.

mains there. In contrast, the DNA that only partially enters the array is driven back to the entrance to increase their configurational entropy (Turner *et al.*, 2002).

To perform the separation, Cabodi, Turner, and Craighead (2002) set the initial pulse time so that the short DNA tends to completely enter the array while the longer DNA tends to partially enter. Complete entry is a stochastic process, so the time for the "on" pulse is gradually increased. In the subsequent pulses, DNA already in the array reptates further away from the interface while additional DNA is injected at the inlet. While the method works in principle, there are some challenges for using entropic recoil to separate long DNA (aside from the fabrication of such dense shallow arrays) (Cabodi, Turner, and Craighead, 2002). First, DNA that happens to adopt a herniated form enters the array more rapidly than expected. In contrast, DNA that forms a hairpin at the entrance enters much more slowly. The latter phenomena lead to band broadening for a given molecular weight. Second, the recoil time scales quadratically with contour length and can be very long as the molecular weight increases.

V. THE SLIT-WELL MOTIF

Having completed our discussion of the dynamics of DNA in arrays of posts, we now turn our attention toward the other standard microfabricated geometry for DNA electrophoresis: the slit-well motif in Fig. 31. This system consists of a periodic array of deep wells of length l_w and depth d_w connected by narrow slits of length l_s and depth d_s. In general, we will see that d_s and l_w are at least as large as $2R_g$ so that the DNA can relax therein. In contrast, the slit width is typically commensurate with the Kuhn length of the DNA, $d_s \approx l_k$, and the confinement in the slit is only in one dimension. We also consider the case of a weakly confining slit with a deep well in Sec. V.A.5.

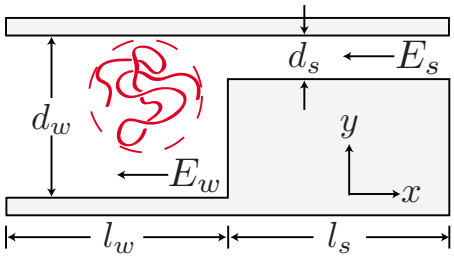

FIG. 31. (Color online) Schematic illustration of the slit-well motif. The relevant geometric length scales and electric field strengths are indicated. The deep region (the well) is generally larger than the equilibrium size the DNA in the device.

These devices are electrically insulating, so the nominal electric field in the well E_w is lower that in the slit E_s. If we make a simple resistors-in-series model, then the electric fields are related by

$$E_w/E_s = d_s/d_w. \tag{69}$$

As was the case for post arrays, the local details of the inhomogeneous electric field also affect the DNA dynamics.

In this section we explore two modes of operations for DNA electrophoresis in the slit-well motif: (i) entropic trapping (Han *et al.*, 1999) and (ii) filtration (Fu *et al.*, 2005). In general, the separation arises from the change in entropy upon entering the slit and the need to overcome the concomitant energy barrier. Although the separation mechanism is thermodynamic in origin, the kinetics of hopping over the barrier play a crucial and often surprising role in the transport process.

A. Entropic trapping

We begin with entropic trapping, which is by far the most extensively studied mode of operation for the slit-well motif. As we saw in Sec. II.B.3, entropic trapping occurs in a gel when there are occasional pores with radius $a \approx R_g$. By choosing $d_w \approx 2R_g$ and $d_s \approx l_k$, the slit well provides an ideal system to realize entropic trapping. Indeed, using well depths $d_w = 0.65-1.6$ μm and a slit depth $d_s = 90$ nm in a prototype device, Han and Craighead (1999) demonstrated separation by entropic trapping in a microfabricated slit-well device for electric fields from 20 to 60 V/cm. Below the lower bound for these particular DNA and device length scales, the electric field does not provide sufficient enthalpy to overcome the entropic penalty in a realistic amount of time; above the upper bound, the entropic penalty becomes negligible. The trapping effect is also robust with respect to the device parameters, provided that the slit induces an entropic penalty. To wit, Han and Craighead (1999, 2000, 2002) separated a wide range of DNA in the 5–50 kbp range using various permutations of the trap pitches $l_w + l_s = 4$, 8, 10, 16, 20, and 40 μm, well depths d_w between 650 nm and 3.3 μm, and slits depths d_s ranging from 75 to 100 nm. Naturally, the useful range of electric fields will depend on the device parameters. Han and

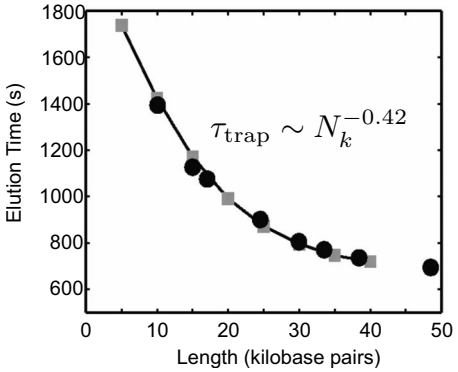

FIG. 32. Elution time as a function of molecular weight for d_w=1.8 μm, d_s=75 nm, l_s=l_w=2 μm, and E=80 V/cm in a second-generation device developed by Han and Craighead (2000). The black circles and gray squares correspond to experiments performed with two different DNA ladders. The scaling law is based on Eq. (70) assuming that t_{travel} is independent of N_k (Wong and Muthukumar, 2008). Data from Han and Craighead, 2000.

Craighead (2000) also developed a clever side-by-side loading method that furnishes data in a form similar to a gel.

Entropic trapping also occurs when there is a long oil slug inside a buffer-filled microchannel. In this system, the thin layer of buffer between the oil and the walls serves as the entropic trap (Hsieh *et al.*, 2008; Hsieh and Wei, 2009). The basic physics of the separation is identical to the slit-well system. However, the geometry is quite different. Owing to interfacial tension, the oil slug is an elliptical cylinder capped with two hemispherical ends. In the experiments of Hsieh *et al.* (2008), the microchannel is rectangular. As a result, the "slits" in this system are the relatively large gaps between the cylinders inscribed in a square.

The most remarkable aspect of the entropic trapping device is not its separation resolution, which is quite impressive on its own, but the fact that the average electrophoretic mobility *increases* with molecular weight (Han and Craighead, 1999). Figure 32 reproduces one particular data set (Han and Craighead, 2000) and the scaling result of a subsequent reanalysis by Wong and Muthukumar (2008). This behavior is counterintuitive since the entropic penalty for deformation inside the slit increases with molecular weight. Moreover, simple translocation-type models for crossing the slit indicate that the translocation time should increase with molecular weight (Sung and Park, 1996; Muthukumar, 1999; Sebastian and Paul, 2000; Panwar and Kumar, 2006). Thus began a flurry of theoretical activity aimed at rationalizing this surprising result.

1. Activation model

Many of the features of the entropic trapping process are captured through a simple scaling model. If we assume that the chain is trapped on average for some time τ_{trap}, then the mobility is given by (Han *et al.*, 1999)

$$\frac{\mu}{\mu_0} = \frac{t_{travel}}{t_{travel} + \tau_{trap}}, \tag{70}$$

where t_{travel} is the time required for the DNA to move through the slit and the well with its free-solution mobility. Han *et al.* (1999) proposed that the trapping time can be described by the Kramers escape over the energy barrier imposed by the slit. Their model built upon work by Deutsch (1987) on the reorientation of long DNA during pulsed-field gel electrophoresis. In order to escape the trap, the chain needs to insert a hairpin containing j Kuhn segments into the slit. The hairpin formation leads to an entropic penalty proportional to jk_BT and a favorable enthalpic term that scales as $j^2q_kE_sl_k$. The corresponding free-energy change is thus

$$\Delta F \sim jk_BT - j^2q_kE_sl_k. \tag{71}$$

The transition state $j_c \sim k_BT/q_kE_sl_k$ occurs at the maximum in the free energy[11]

$$\Delta F_{max}/k_BT \sim k_BT/q_kE_sl_k. \tag{72}$$

Interestingly, the role of the size of the hairpin on ΔF_{max} is independent of whether or not the hairpin is extended inside the slit. In the latter case, the enthalpic contribution is reduced to (Tessier *et al.*, 2002)

$$\Delta F \sim jk_BT - j^{1+\nu}q_kE_sl_k \tag{73}$$

since the chain forms blobs inside the slit. The maximum height of the barrier occurs at $j_c^\nu \sim k_BT/q_kE_sl_k$. However, since a contour length of j_c creates a hairpin length proportional to j_c^ν, the effective size of the hairpin is unaffected by the incomplete extension of the chain. However, the electric field dependence of the barrier differs, scaling as $\Delta F_{max} \sim E^{-1/\nu}$ (Tessier *et al.*, 2002).

The energy barrier should also depend on the size of the slit. Explicitly, the osmotic pressure $\Pi \sim k_BT/d_s^3$ pushing the hairpin out of the slit increases as the slit gets smaller. The resulting energy barrier is (Sakaue, 2006)

$$\frac{\Delta F_{max}}{k_BT} \sim \frac{k_BT}{q_kE_s}\left(\frac{l_k}{d_s^2}\right). \tag{74}$$

All of these models predict that the barrier should be independent of the molecular weight of the chain. However, simulation data indicate that this behavior is valid only for large molecular weights. Using Monte Carlo simulations with the configurational bias chain insertion method (de Pablo *et al.*, 1992), Chen and Escabedo (2003) found that ΔF_{max} is indeed a function of N_k, but only for small N_k. The free-energy energy barrier also depends on the way in which the chain enters the slit

[11] Chen and Escabedo (2003) called into question the common use of j as the variable defining the transition state. Rather, they proposed that the degree of penetration is a better measure of the transition state. The latter is defined as $\Sigma_{i=1}^{j} x_i/N_k$, where the x_i are the locations of the j segments that are inside the slit.

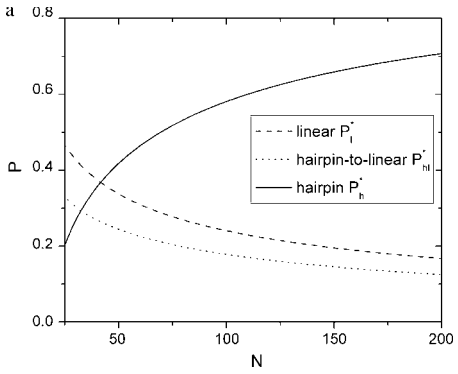

FIG. 33. Probability of end-first (linear) hairpin to linear or hairpin insertion as a function of the chain size using the model of Wong and Muthukumar (2008) with a dimensionless force of 0.08 and slit width of 1.5. From Wong and Muthukumar, 2008.

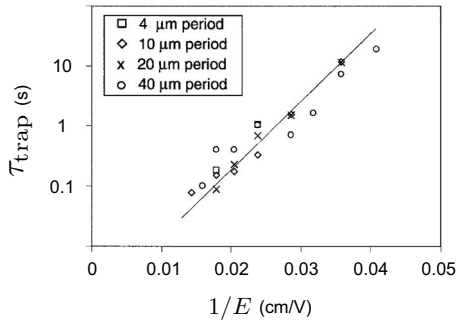

FIG. 34. Plot of the trapping time for λ-DNA as a function of the inverse of the electric field for entropic trap arrays with different pitches. From Han *et al.*, 1999.

(Tessier *et al.*, 2002) because the barrier height for a linear configuration inside the slit is half that for a hairpin (Sebastian and Paul, 2000; Wong and Muthukumar, 2008). As shown in Fig. 33, a blob model of the escape process predicts a combination of linear and hairpin escapes for smaller chains (Wong and Muthukumar, 2008). In arriving at the latter result, Wong and Muthukumar (2008) pointed out that there are two paths that lead to a linear configuration inside the slit. The simplest path is an end-first entry. However, if the hairpin forms near the end of the chain, then it can unravel inside the slit. For very large chains, the hairpin mode of entry is dominant (Sebastian and Paul, 2000; Wong and Muthukumar, 2008). If we were to compute an effective barrier height by averaging over both linear and hairpin escapes, this would lead to an N_k dependence at small N_k.

Regardless of the particular model chosen for to describe $\Delta F_{\max}$, the trapping time for the Kramers escape problem is given by (Kramers, 1940)

$$\tau_{\text{trap}} = \tau_0 \exp(\Delta F_{\max}/k_B T), \tag{75}$$

where τ_0 is the rate constant for the escape attempt frequency. For the models discussed thus far, at least in the large N_k limit, the barrier height is independent of N_k and inversely proportional to the electric field. If τ_0 is also independent of the electric field, then the logarithm of the trapping time should scale as $1/E$. As shown in Fig. 34, this is indeed the case for a range of experimental data (Han *et al.*, 1999). The latter scaling has also been reported by numerous simulations of the entropic trap (Tessier *et al.*, 2002; Chen and Escabedo, 2003; Panwar and Kumar, 2006), breaking down for small chains (Tessier *et al.*, 2002). As noted above, the smaller chains exhibit a mixture of linear and hairpin configurations and thus have an averaged barrier height that depends on molecular weight.

If the barrier height is independent of molecular weight, then the mechanism underlying the separation must be embodied in the prefactor τ_0 describing the frequency that the chain attempts to cross the barrier. Han and Craighead (2002) proposed that this factor should be inversely proportional to the area of the chain that can be pressed against the slit, $d_s R_g$. If the chain is Gaussian, then this scaling predicts that $\tau_{\text{trap}} \sim N_k^{-1/2}$. The mobility produced by the Gaussian scaling is close to the scaling $\tau_{\text{trap}} \sim N_k^{-0.42}$ shown in Fig. 32 and provides a good fit to other experimental data (Han and Craighead, 2002).

It is not clear, however, that such large DNA would form an ideal chain. A model with $\tau_0 \sim 1/R_g$ that accounts for excluded volume implies that $\tau_{\text{trap}} \sim N_k^{-3/5}$ (Streek *et al.*, 2004), which deviates further from the experimental data. The double-well model of Sebastian and Paul (2000) leads to $\tau_0 \sim 1/N_k E^{1/2}$ for a hairpin crossing, which does not appear to be an improvement.

Wong and Muthukumar (2008) proposed an alternate model that appears to provide a much more reasonable fit to the experimental data while still retaining the excluded volume of the chain. Explicitly, they assumed that the prefactor τ_0 is independent of N_k and included the conformational entropy of the chain remaining in the well,

$$S(j) \approx k_B T(1-\gamma)\ln(N_k - j), \tag{76}$$

in the free-energy barrier. For a self-avoiding chain, the parameter γ=0.69. Their model thus assumes that the relaxation time of the chain is short compared to the frequency for injecting segments into the slit. With the later scaling, Wong and Muthukumar (2008) arrived at $\tau_0 \sim N^{-0.31}$ for end-first escape and $\tau_0 \sim N^{-0.38}$ for hairpin escape. The linear escape leads to the shorter DNA moving more quickly, which contradicts the experimental evidence. However, as noted in the context of Fig. 33, large chains tend to escape by forming hairpins. The corresponding exponent is very to the scaling $N^{-0.42}$ appearing in Fig. 32.

2. Device length scales and electric field gradients

For a given average electric field E, the nominal electric field in the slit is controlled by the relative size of the slit and well through Eq. (69). Using the Kramers escape model for the entropic trap, we can gain some qualitative insights into the role of the device length scales. For example, increasing the well depth d_w while fixing E and the other length scales leads to an increase in E_s. The

increased electric field in the slit lowers the free-energy barrier and generally favors escape (Han and Craighead, 2002). However, if the wells are sufficiently deep, then DNA that diffuses into the corner can remain trapped for long times. This slow mode of escape has a very weak dependence on molecular weight, scaling as $N^{-1/5}$ for a freely draining model with excluded volume (Streek *et al.*, 2004).

The effect of increasing the slit depth d_s while keeping the remaining parameters fixed is more complicated. From a resistors-in-series model for the electric field, increasing the slit depth decreases the electric field therein. Thus, Eq. (72) predicts that the free-energy barrier height increases with increasing d_s. If we also include the osmotic pressure pushing the chain out of the slit, as seen in Eq. (74), then the free-energy barrier height decreases with increasing d_s. In any event, neither of these arguments account for the dependence of the prefactor τ_0 on d_s. Presumably, a larger slit will lead to a decrease in τ_0 since more of the chain can be in contact with the slit (Han and Craighead, 2002).

While the resistors-in-series model is useful at the scaling level, it is important to realize that the local electric field is inhomogeneous, especially near the interface between the slit and the well (Tessier *et al.*, 2002). The ensuing electric field gradients lead to deformation of the chain. For example, the bond-fluctuation simulations of Tessier *et al.* (2002) indicate that upon exiting the slit the electric field gradients should produce a large compression in the x direction of Fig. 31 and a corresponding extension of the chain in the y direction. Since the chain needs to stretch in the x direction to pass through the slit in the first place, the electric field gradients at the exit of the slit aid in the relaxation back to the coiled form. This electric-field-enhanced relaxation could be one reason why the entropic trapping mechanism can operate up to the relatively large electric field of 128 V/cm for shorter DNA (Han and Craighead, 2000).

The details of the electric field also play a role at the entrance to the slit. For example, Panwar and Kumar (2006) noted that the electric field gradients can suppress the trapping mechanism observed by Streek *et al.* (2005) in relative shallow wells. The electric field also tends to press the DNA against the wall under the slit (Tessier *et al.*, 2002; Chen and Escabedo, 2003; Sakaue, 2006). At higher electric fields, Tessier *et al.* (2002) suggested that the extent of the pinning of the DNA to the well/slit interface, which increases with molecular weight, is the main mechanism behind the separation. Under large electric fields, the free-energy barrier for escape becomes small. However, the process is still stochastic and the leading part of the chain can fluctuate in and out of the slit. These fluctuations only depend on the size of the hairpin and not the molecular weight of the chain. After a fluctuation out of the slit, the small molecules can more easily move away from the interface. In contrast, the larger molecules are pinned more tightly near the interface by their higher charge and lower diffusion coefficients. The larger molecules tend to make a number of attempts to cross the barrier before larger-scale fluctuations cause the longer DNA to temporarily move away from the interface. Thus, the extent of pinning to the interface also favors the escape of larger DNA.

3. Hydrodynamic interactions

The simulations of entropic trapping discussed thus far (Tessier *et al.*, 2002; Chen and Escabedo, 2003; Streek *et al.*, 2004) have not incorporated hydrodynamic interactions. As noted in a number of publications (Tessier *et al.*, 2002; Streek *et al.*, 2004; Panwar and Kumar, 2006), the entropic trap is analogous to a mechanical force that impedes the DNA. During the trapping, the counterions remain mobile even though the DNA is fixed. Based on the electrohydrodynamic equivalence principle (Long *et al.*, 1996), hydrodynamic interactions should play a role.

Sakaue (2006) addressed the role of hydrodynamic interactions on the Kramers escape model of entropic trapping at the scaling level. In this model, the stall force near the well/slit interface is opposed by the entropic force. As a result, the critical electric field required to deform the chain in the well,

$$E^{\mathrm{def}} \approx \frac{k_B T}{\eta \mu_0 l_k d_s} N_k^{-3/5}, \tag{77}$$

decreases with molecular weight. When $E_s > E^{\mathrm{def}}$, the chain is pushed against the slit and adopts a cigarlike conformation with blob size $k_B T/\eta\mu_0 E_s d_s$. If the blobs are smaller than the size of the slit d_s, then the deformation of the chain at the interface eliminates the entropic trapping effect. The DNA is thus smoothly injected into the slit above the electric field (Sakaue, 2006)

$$E^{\mathrm{inj}} \approx E^{\mathrm{def}}(R_g/d_s). \tag{78}$$

Electric fields corresponding to $E_s > E^{\mathrm{inj}}$ are of little interest for separations.

Sakaue (2006) also identified the critical electric field in the slit at which the size of the hairpin at the transition state is equal to the entire size of the chain. This permeation electric field corresponds to

$$E^{\mathrm{per}} \approx E^{\mathrm{inj}}(d_s/R_g)^{5/3}. \tag{79}$$

Since this transition state corresponds to the entire chain entering the slit, there is no need to account for the free energy of the chain in the well.

The model of Sakaue (2006) for $E^{\mathrm{per}} < E_s < E^{\mathrm{def}}$ predicts that the trapping time scales as $\tau_{\mathrm{trap}} \sim N^{-3/5}$. This scaling is equivalent to the freely draining models proposed by Han and Craighead (2002) and Streek *et al.* (2004), where the latter is modified for the excluded volume. The scaling law changes for $E^{\mathrm{def}} < E_s < E^{\mathrm{inj}}$. In this regime, the competition between the osmotic pressure across the slit and the enthalpic contribution due to the electric field furnishes a free-energy barrier[12]

[12]Hsieh and Wei (2009) also suggested simply adding an osmotic term to the free energy to give a form $\Delta F_{\max}/k_B T = -(2R_g/d_s)^{5/3} + E_0/E_s$, where E_0 is a constant. This leads to a free-energy barrier height that depends on N_k.

$$\frac{\Delta F_{\max}}{k_B T} \approx \frac{[1-(E_s/E^{\text{inj}})^3]^2}{E_s/E^{\text{inj}}}. \tag{80}$$

This free-energy barrier height is independent of N_k and does not scale as $1/E$ if E_s/E^{inj} is not very small.

4. Relationship to polymer translocation

Activated escape from an entropic trap shares some properties in common with the much-studied problem of DNA translocation through a small pore. We do not have sufficient space here to discuss the translocation problem in detail; the interested reader is encouraged to consult the seminal experimental paper by Kasianowicz *et al.* (1996) and the references which cite this paper. In the context of the slit-well length scales in Fig. 31, a typical translocation model corresponds to a short narrow pore, wherein l_s and d_s are no larger than the Kuhn length. As a result, modeling the escape through this "hole in a wall" requires accounting for the chemical potential and configurational entropy of the chain on either side of the slit. In a second contrast with the entropic trap, the "well" dimensions (l_w and d_w) for translocation are much larger than the radius of gyration of the DNA. From Eq. (69), the electric field is concentrated inside the slit and effectively zero in the well. Finally, experiments for translocation correspond to a single well-slit-well combination, as opposed to the thousands of periods in an entropic trap.

Early experiments demonstrated that the translocation time is proportional to molecular weight (Kasianowicz *et al.*, 1996), a result that was confirmed by a number of theoretical analyses (Sung and Park, 1996; Muthukumar, 1999; Sebastian and Paul, 2000). Thus, there should be a regime where the escape in a slit-well motif crosses over from entropic trapping to translocation. To clarify this concept, Panwar and Kumar (2006) used bead-rod Brownian dynamics simulations to dissect the overall escape process into three steps: approach to the slit, activation, and crossing. They indeed found that the time to approach the slit and the time to activate the crossing (which we have called τ_{trap}) decrease with molecular weight. In contrast, the crossing time increases with molecular weight. The precise location at which the crossing and activation times balance depends on the particular model used to describe the process. For example, with the double-well model of Sebastian and Paul (2000), Panwar and Kumar (2006) found that the critical electric field for balancing these two-time scales varies as $E^* \sim 1/\ln N_k$. In principle, a slit-well device could operate in a band-inverted mode for a particular range of electric fields by crossing over to the translocation-dominated mode of operation.

5. Weak confinement

Compared to the entropic trapping device of Han and Craighead (1999), it is considerably easier to fabricate weakly confining media with slit and well sizes of several microns. In contrast to the case of strong confinement, Duong *et al.* (2003) observed that the mobility of λ-DNA (48.5 kbp) is now higher than that of T2-DNA (164 kbp) over a range of 20–120 V/cm. Using Brownian dynamics simulations and further experiments, Streek *et al.* (2005) developed a two-state model to describe these mobility data. In the high mobility state, the DNA simply moves smoothly through the device without any trapping. In the lower mobility state, the DNA jumps between wells. The mechanism is similar to that in the device by Han *et al.* (1999), except that the chain can more easily enter the slit. The average mobility depends on the fraction of the DNA that is in each state. The λ-DNA moves more quickly that the T2-DNA because, on average, a higher fraction of the λ-DNA exists in the high mobility state.

The electric field required to stabilize the slow state requires a critical amount of stretching. The data obtained by Streek *et al.* (2005) indicate that the critical number of segments to stabilize a slow state scales as $N_k^* \sim l_w E^{-2/3}$. For weak electric fields, the critical length to stabilize the slow state can exceed the size of the DNA. In the latter case, the DNA would only move in the fast unperturbed state and the separation should be lost (Streek *et al.*, 2005).

6. Pulsed electric fields

To date, all entropic trapping experiments were performed using a dc electric field. The resulting electrophoretic mobility is a nonlinear function of molecular weight and electric field. However, even before the first experiments in a slit-well motif (Han *et al.*, 1999), Slater *et al.* (1997) had already predicted from simulations that entropic trapping leads to nontrivial behavior in a low-frequency ac electric field. For example, operating in the zero-integrated-field electrophoresis (ZIFE) mode, the resulting electrophoretic mobility is not only nonzero but can be shifted such that the smaller DNA now has the higher mobility—even though the entropic trapping process remains unchanged. Likewise, it is even possible to have different size DNA moves in different directions due to the broken symmetry (Slater *et al.*, 1997).

The entropic trapping device of Han and Craighead (1999) is the ideal platform for testing the ratchet ideas proposed by Slater *et al.* (1997). To provide quantitative predictions, Tessier and Slater (2002) used their simulated mobility data for a dc electric field to explore the mobility of DNA in a slit-well device in the low-frequency ac limit. Figure 35 reproduces the bidirectional results obtained when the electric field E_1 is applied for some time t_1 and then an electric field $E_2 = -E_1/2$ is applied for some time $t_2 = r_t t_1$. For a given pair of DNA, there exists a range of values r_t where the smaller DNA has a positive mobility and the larger DNA has a negative mobility. Tessier and Slater (2002) explored a range of possible ratchet modes for the entropic trap, including the ZIFE mode and a broken spatial symmetry corresponding to adding a step before the slit. These possible modes of operation for the entropic trap remain a theoretical prediction awaiting their experimental test.

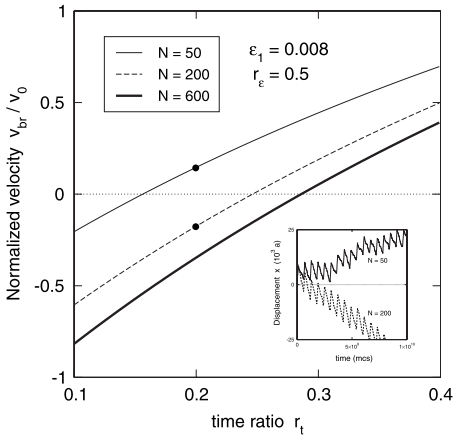

FIG. 35. Normalized velocities (relative to a typical velocity in the dc separation regime) as a function of the time ratio $r_t = t_1/t_2$ for the dimensionless electric field ϵ_1 and electric field ratio $\epsilon_2 = -r_\epsilon \epsilon_1$. The inset shows two representative trajectories. From Tessier and Slater, 2002.

B. Short DNA and (nano)filtration

In our discussion of entropic trapping, we have focused on long flexible DNA. The entropic penalty for entering the slit arises because the long DNA needs to form an entropically unfavorable hairpin to enter the slit. We now turn our attention to short rigid DNA containing $N_{bp} < 1000$ base pairs. As a simple approximation, DNA of one or two persistence lengths can be treated as a slender rod of length $\mathcal{L} = N_{bp} l_{bp}$. For a more accurate measure of the length, we can use the Kratky-Porod model for the mean-square end-to-end distance (Doi and Edwards, 1988; Fu *et al.*, 2006),

$$\bar{R}^2 = l_k^2 \{N_k - \tfrac{1}{2}[1 - \exp(-2N_k)]\}. \tag{81}$$

This DNA is too small to undergo a coil-stretch transition upon entering the slit (Giddings *et al.*, 1968). Rather, they lose orientational degrees of freedom inside the slit due to steric interactions with the walls. If the Debye layer is not thin relative to the slit size d_s and the walls are negatively charged, the excluded volume effect is augmented by electrostatic repulsion. The rotational degrees of freedom are further reduced, and we can view the electrostatic repulsions as effectively reducing the size of the slit (Bow *et al.*, 2008).

Since the DNA in this system is short, the slits must be extremely thin in order to provide an entropic barrier. The nanofilter devices produced by Fu *et al.* (2005) featured slits from 40 to 180 nm, and a subsequent device pushed the slit width down to 21 nm (Strychalski *et al.*, 2009). Fu *et al.* (2005) reported high-resolution separations for both denatured proteins and a DNA ladder (50, 150, 300, 500, and 766 bp) using a 60 nm slit. While the throughput of a single filter is limited in the design of Fig. 36, Mao and Han (2009) provided a route for fabricating tall narrow filters—essentially a very dense post array for short DNA. Like the entropic trapping system, the nanofilters can be arranged in the anisotropic configuration of Fig. 27 for a continuous separation (Fu *et al.*, 2007; Mao and Han, 2009).[13]

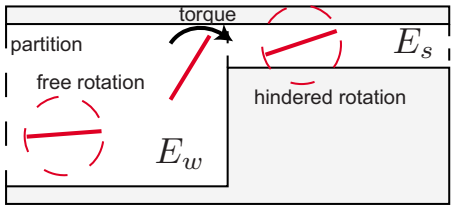

FIG. 36. (Color online) Schematic illustration of filtration of small rigid DNA by size in a slit-well motif, the so-called nanofilter. At low electric fields, the reduced configurational entropy in the slit leads to an effective partitioning between the two regimes. At high electric fields, the torque due on a molecule near the partition governs the separation.

1. Near-equilibrium mode

As its name implies, the nanofilter operates under a weak electric field in a manner similar to a membrane filter. As a result, the basic physics underpinning the separation are well understood (Giddings *et al.*, 1968). The excluded volume interactions in the slit increase with molecular weight, leading to the larger DNA tending to partition into the well. Under a weak driving force, the small DNA tends to move more quickly through the device. Once the reduction in enthalpy by moving into the slit is larger than the entropic penalty, the resolution is lost. These basic conclusions from chromatography theory agree with the experimental data (Fu *et al.*, 2005).

In contrast to conventional filtration media, the nanofilter has an ordered periodic geometry. As a result, we should be able to exploit this geometric control to develop robust theories for transport in the nanofilter. In their first model, Fu *et al.* (2006) modified the activated escape model for an entropic trap (Han *et al.*, 1999). For the nanofilter, they argued that the trapping time in a weak electric field should be

$$\tau_{trap} \approx c N_{bp} / E^2 K, \tag{82}$$

where K is the partition coefficient for a rod in a slit of size d_s (Giddings *et al.*, 1968) and c is a dimensional prefactor. Using c as a fitting parameter, Fu *et al.* (2006) obtained excellent agreement with their experimental data for the shorter molecules. The theory begins to break down for the longer molecules, as the model employed for the partition coefficient does not account for the flexibility of the longer DNA. The DNA achieves sufficient flexibility at 1500 bp for the migration mechanism to shift from filtration to entropic trapping (Fu *et al.*, 2006, 2007).

[13] In fact, Fu *et al.* (2007) demonstrated entropic trapping, filtration, and charge exclusion with a single device. The particular mode of operation is controlled by the buffer composition and the analyte's size or charge density.

Li *et al.* (2008) proposed a more detailed model that further attempts to account for the anisotropic diffusivity and electrophoretic mobility expected for a rodlike particle in a confined geometry. Note that, owing to the flow of counterions, these tensors are not related by the Stokes-Einstein equation. In order to simplify the calculations, Li *et al.* (2008) preaveraged the diffusion and electrophoretic mobility tensors over the available orientations to avoid including the orientation of the rod in their convection-diffusion equation. Likewise, the role of the excluded volume in the slit was approximated by an entropic contribution to the flux. The model does an excellent job of matching the experimental mobility data. However, the model predicts that the band broadening should decay with molecular weight. The experimental band broadening, while of comparable magnitude to the model predictions, is effectively independent of molecular weight. A number of experimental factors contribute to band broadening (size of the injection plug and Joule heating, for example) that are not included in the model. As a result, it is difficult to make a definitive conclusion about the model's ability to capture the dispersion.

2. Strong electric fields

Near-equilibrium models such as the activated escape model of Fu *et al.* (2006) predict that the DNA will all move with identical mobilities in a strong electric field. Indeed, experiments showed the onset of band compression for the larger DNA at 100 V/cm (Fu *et al.*, 2005), but higher electric fields were not accessible due to electrical breakdown of the oxide layer of the device. Laachi *et al.* (2007) argued that the trend exhibited by the experimental data is not band compression but rather the onset of a band inversion at higher electric fields. When the electric field is strong, the DNA no longer has time to explore the full space of the well. Rather, they are rapidly convected from slit to slit while undergoing rotational diffusion. In order to enter the slit, the DNA needs to reassume an allowable orientation. Laachi *et al.* (2007) argued that the reorientation process is dominated by the torque due to the difference between the weak electric field in the well and the strong electric field in the slit. The magnitude of the torque is the product of the total charge on the DNA and its length, thus scaling as N_{bp}^2. Under this mechanism, once the rotational Péclet number (the ratio of the torque to thermal energy) exceeds unity then the longer DNA should exit the device first.

The latter theory was tested by Strychalski *et al.* (2009) using 55 bp, 259 bp, and 753 bp DNA in two different nanoslit devices, one with $d_s=42$ nm slits and the other with $d_s=21$ nm slits. They indeed observed a band compression and eventual inversion, with the effect most pronounced in the thinner slit devices. At the critical electric field, the smallest rotational Péclet number is O(1), in agreement with the argument underlying the torque-assisted escape model (Laachi *et al.*, 2007). In an effort to move beyond a phenomenological description of the process, Strychalski *et al.* (2009) proposed an activated escape model for the nanofilter. The model provides a good fit for the experimental mobility data with three adjustable parameters. However, some of the fitted parameters deviate by one order of magnitude from their theoretical values. Moreover, the model assumes that the escape over the barrier is purely diffusive. It remains to be seen whether including an electrorotation contribution to the attempt frequency improves the fit with the experimental data.

VI. PERSPECTIVES

Having looked back at the past two decades of research on DNA electrophoresis in microfabricated systems, what does the future hold? Based on what we have seen so far, it is clear that a complete understanding of DNA electrophoresis in artificial sieving matrices requires an integrated mix of single-molecule experiments, ensemble-level measurements of the average electrophoretic mobility and dispersivity, and computer simulation. These sentiments echo the outlook of Slater (2009), and I think that the tight interplay between theory and experiment explored here serves as a template for attacking similar problems. For example, an emerging area in DNA separations is electrophoresis in colloidal crystals and inverse opals (Meistermann and Tinland, 2000; Zhang and Wirth, 2005; Zeng and Harrison, 2006, 2007; Shiu *et al.*, 2008; Zeng *et al.*, 2008). It remains to be seen whether these self-assembled systems, which are relatively easy to fabricate, are simply an ordered version of gel electrophoresis or whether the pertinent length scales of the crystals and the corresponding confinement will play an important role. The approach reviewed here to address DNA dynamics in post arrays would certainly be effective for these self-assembled systems.

While there are still a number of questions that remain unanswered by this review, especially related to transport in post arrays, it seems that we now have a fairly thorough understanding of the basic physics. Is there still work to be done by physicists in the post array or slit-well geometries? If the goal is to discover some new basic physics, then I think the answer is no; all of the low-hanging fruit has been picked. Rather, the interesting questions related to these devices have crossed over from being questions of physics to questions of engineering. To put it another way, the problem is no longer to discover new physics but to apply known physics to the design of operational devices. For all of the basic physics that has been worked out in the past two decades, we still do not know how to design an optimal post array or even whether a post array is actually an improvement over pulsed-field gel electrophoresis when put in the hands of an end user. Answering these questions requires developing a conceptual framework that allows us to estimate the performance of the device as a function of its operating parameters (e.g., the size of the DNA, the electric field, the post spacing, and the post diameter) and then to test our framework in the labora-

tory. This is the quintessential task of the engineer.

Although the DNA separation problem has shifted from physics to engineering, two related problems still remain. The first area is developing a rational method for simulating DNA electrophoresis along the lines of the thinking in the colloidal electrophoresis community (Anderson, 1989). As pointed out in Sec. II.A.3, the local force model remains ubiquitous in the DNA electrophoresis literature even though there have been several prominent arguments against its use (Long *et al.*, 1996; Viovy, 2000). A number of methods now exist for incorporating mesoscopic hydrodynamic effects, including molecular dynamics, lattice Boltzmann, and stochastic rotational dynamics (Slater *et al.*, 2009). While these methods have been used with success in other fields, they remain in a nascent stage in the context of DNA and polyelectrolyte electrophoresis. Recent simulation models (Frank and Winkler, 2009; Grass and Holm, 2010) led to quantitative predictions of the free-solution mobility of short polyelectrolytes. The key to validating these models was the existence of experimental data, such as those in Fig. 2. As we move toward modeling longer chains and incorporating wall effects into these models, the wealth of knowledge on DNA electrophoresis in microfabricated devices will provide the test bed for validating the methods.

The second area is understanding DNA dynamics (including electrophoresis) in nanoslits and nanochannels. It is already clear that separation of short oligonucleotides is enhanced in a nanochannel when the Debye layers overlap (Pennathur *et al.*, 2007). More surprising are the increasing number of studies that report a size-dependent electrophoretic mobility for long DNA in nanochannels (Cross *et al.*, 2007; Mathe *et al.*, 2007; Parikesit *et al.*, 2008; Salieb-Beugelaar *et al.*, 2008) or band-inversion behavior in a nanoslit (Strychalski *et al.*, 2009). These observations are often the result of single-molecule videomicroscopy, which is only one of the analysis tools at our disposal and certain to be complemented by simulation in the near future.

An important part of understanding experiments in nanoslits and nanochannels is accounting correctly for the confinement of the DNA. In the problems discussed in this review, we were able to make ample progress by simply treating DNA as a piece of rope or, at a somewhat more detailed level, with a bead-spring or bead-rod model. If the chain is confined to a dimension smaller than its Kuhn length, which is readily achieved with advanced nanofabrication methods, then the bead-spring and bead-rod models break down. We thus need to adopt a finer-scale model of the DNA to study these regimes (Odijk, 1983, 2008). Only now are we able to experimentally probe DNA dynamics under strong confinement, making this a promising area for future work far beyond those problems related to DNA electrophoresis. Indeed, the combination of experiment, theory, and simulation explored here will prove key to gaining a complete understanding of the problem.

LIST OF SYMBOLS AND ABBREVIATIONS

A	constant
a	pore radius or spacing between obstacles
b	impact parameter
c	constant
c_i	concentration of ion i
D	molecular diffusion coefficient
D^{Rouse}	Rouse diffusion coefficient
D^*	dispersivity (effective diffusivity)
De	Deborah number
d	post diameter
d_s	slit depth
d_w	well depth
E	magnitude of the (average) electric field
E^{def}	critical electric field for deformation
E^{inj}	critical electric field for injection
E^{per}	critical electric field for permeation
E_s	electric field in a slit
E_w	electric field in a well
E_0	strong electric field on the Kuhn length scale
$\mathbf{E}$	electric field vector
$\mathbf{E}_t$	tangential electric field vector
$\mathbf{E}^\infty$	electric field far from an obstacle
e	charge of an electron
$\mathbf{e}_r$	radial unit vector
$\mathbf{e}_\theta$	angular unit vector
F	force
F_{elec}	electrical force acting on a chain
F_{fric}	friction coefficient acting on a chain
$f(\cdots)$	function of $\cdots$
h	channel height
h_x	projection of the chain in the electric field direction
I	ionic strength
j	number of Kuhn segments inserted into the slit
j_c	number of Kuhn segments at transition state
K	partition coefficient
k_B	Boltzmann's constant
L_{tube}	tube length
l_B	Bjerrum length
l_{bp}	distance between two base pairs
l_c	effective charge spacing
l_k	Kuhn length
l_{OSF}	Odijk-Skolnick-Fixman length
l_p	persistence length
$l_{p'}$	bare persistence length
l_s	length of a slit
l_w	length of a well
$\mathcal{L}$	contour length of the chain
$\mathcal{L}^{\mathrm{eff}}$	effective contour length
N	degree of polymerization
N_{blob}	number of blobs
N_{bp}	number of base pairs
N_k	number of Kuhn segments
N_k^*	crossover molecular weight
n	post row number
n^*	excluded post rows

Pe	Péclet's number
Pe*	critical Péclet number
P_{hook}	hooking probability
q_k	charge per Kuhn segment
$\bar{R}$	mean end-to-end distance
R_g	radius of gyration
R_{obs}	obstacle radius
r	radial distance
r_{ij}	distance between segment i and $j \neq i$
r_t	time ratio
r_ϵ	electric field ratio
S	entropy
s^*	critical position on an arc
T	temperature
t	time
t_c	collision time
t_d	diffusion time
t_H	hold-up time
$t_{H,\text{X}}$	hold-up time (X collision)
t_{or}	orientation time
t_p	pulse time
t_{travel}	travel time
t_{unhook}	unhooking time
$t_{\text{unhook,X}}$	unhooking time (X collision)
v	velocity
v_{br}	velocity of a ratchet
v_{tube}	curvilinear velocity in a reptation tube
v_0	nominal velocity in an entropic trap array
$\mathbf{v}$	velocity vector
$\mathbf{v}_{\text{slip}}$	slip velocity vector
x	position (rectangular coordinates)
x_{com}	x position of the center of mass
y	position (rectangular coordinates)
z_i	valence of species i
α	angle
γ	parameter
ΔF	change in free energy
ΔF_{max}	height of free-energy barrier
Δt	elapsed time
Δx	displacement
ϵ	dimensionless electric field
ϵ_b	bulk permittivity
ϵ_0	permittivity of free space
$\dot{\epsilon}$	strain rate
ζ	ζ potential
η	fluid viscosity
θ	angular position (cylindrical coordinates)
κ^{-1}	Debye length
μ	effective electrophoretic mobility
μ_{CTRW}	electrophoretic mobility from continuous-time random walk
μ_{ele}	electrophoretic component of μ_0
μ_{eof}	electro-osmotic component of μ_0
μ_{geo}	electrophoretic mobility from geometration
μ_0	free-solution mobility
ν	Flory exponent
ξ_c	friction coefficient of the chain
ξ_c^{Rouse}	Rouse friction coefficient
ξ_c^{Zimm}	Zimm friction coefficient
ξ_k	friction coefficient of a Kuhn segment
Π	osmotic pressure
Π_c	collision probability
ρ	post density
τ_B	Brownian time
τ_r	relaxation time
τ_{trap}	trapping time
τ_0	Kramers escape prefactor
ϕ	angle
χ	offset between two arms
χ^*	critical offset
χ_1	length of the short arm

ac	alternating current
bp	base pairs
dc	direct current
kbp	kilobase pair
OSF	Odijk-Skolnick-Fixman
PDMS	polydimethylsiloxane
PSS	polystyrene sulfonate
PVP	polyvinylpyrrolidone
TBE	tris-base, boric acid, EDTA (buffer)
TOTO	intercalating dye (molecular probes)
YOYO	intercalating dye (molecular probes)
ZIFE	zero-integrated-field electrophoresis

ACKNOWLEDGMENTS

A number of topics in this review resulted from discussions with Patrick Doyle, Gary Slater, and Jean-Louis Viovy. I am grateful to Noritoshi Araki, Jaeseol Cho, Sarit Dutta, Tobias Foster, Scott King, Nabil Laachi, Margaret C. Linak, Nicolas Minc, Daniel W. Olson, Jia Ou, Joel Thomas, and Doug Tree for their comments on earlier versions of this paper. Michel Gauthier prepared Figs. 8, 25(a), and 30, and Jia Ou prepared Fig. 22. This research was supported by the David and Lucile Packard Foundation, the NSF Award No. CBET-0642794, the DARPA Award No. N66001-09-1-2103 and the Camille and Henry Dreyfus Foundation.

REFERENCES

Anderson, J. L., 1989, Annu. Rev. Fluid Mech. **21**, 61.
André, P., D. Long, and A. Ajdari, 1998, Eur. Phys. J. B **4**, 307.
Arvanitidou, E., and D. Hoagland, 1991, Phys. Rev. Lett. **67**, 1464.
Austin, J. O., R. H. Tegenfeldt, H. Cao, S. Y. Chou, and E. C. Cox, 2002, IEEE Trans. Nanotechnol. **1**, 12.
Austin, R. H., N. Darnton, R. Huang, J. Sturm, O. Bakajin, and T. Duke, 2002, Appl. Phys. A: Mater. Sci. Process. **75**, 279.
Austin, R. H., and W. D. Volkmuth, 1993, Analusis **21**, 235.
Baba, M., T. Sano, N. Iguchi, K. Iida, T. Sakamoto, and H. Kawaura, 2003, Appl. Phys. Lett. **83**, 1468.
Bakajin, O., T. A. J. Duke, J. Tegenfeldt, C.-F. Chou, S. S. Chan, R. H. Austin, and E. C. Cox, 2001, Anal. Chem. **73**, 6053.

Bakajin, O. B., T. A. J. Duke, C. F. Chou, S. S. Chan, R. H. Austin, and E. C. Cox, 1998, Phys. Rev. Lett. **80**, 2737.
Balducci, A., C. C. Hsieh, and P. S. Doyle, 2007, Phys. Rev. Lett. **99**, 238102.
Baumann, C. G., S. B. Smith, V. A. Bloomfield, and C. Bustamante, 1997, Proc. Natl. Acad. Sci. U.S.A. **94**, 6185.
Baumgärtner, A., and M. Muthukumar, 1987, J. Chem. Phys. **87**, 3082.
Becker, H., and L. E. Locascio, 2002, Talanta **56**, 267.
Birren, B. W., E. Lai, S. M. Clark, L. Hood, and M. I. Simon, 1988, Nucleic Acids Res. **16**, 7563.
Bloomfield, V. A., D. M. Crothers, and I. Tinioco, Jr., 2000, *Nucleic Acids: Structures, Properties and Functions* (University Science Books, Sausalito, CA).
Boileau, J., and G. W. Slater, 2001, Electrophoresis **22**, 673.
Bow, H., J. Fu, and J. Han, 2008, Electrophoresis **29**, 4646.
Brochard, F., and P. G. de Gennes, 1977, J. Chem. Phys. **67**, 52.
Brochard-Wyart, F., 1993, Europhys. Lett. **23**, 105.
Brochard-Wyart, F., 1995, Europhys. Lett. **30**, 387.
Bustamante, C., J. F. Marko, E. D. Siggia, and S. Smith, 1994, Science **265**, 1599.
Cabodi, M., Y.-F. Chen, S. W. P. Turner, H. G. Craighead, and R. H. Austin, 2002, Electrophoresis **23**, 3496.
Cabodi, M., S. W. P. Turner, and H. G. Craighead, 2002, Anal. Chem. **74**, 5169.
Calladine, C. R., C. M. Collis, H. R. Drew, and M. R. Mott, 1991, J. Mol. Biol. **221**, 981.
Calladine, C. R., and H. R. Drew, 1997, *Understanding DNA* (Academic, San Diego).
Campbell, L. C., M. J. Wilkinson, A. Manz, P. Camilleri, and C. J. Humphreys, 2004, Lab Chip **4**, 225.
Campbell, S. A., 2007, *The Science and Technology of Microelectronic Fabrication* (Oxford University Press, Oxford).
Carle, G. F., M. Frank, and M. V. Olson, 1986, Science **232**, 65.
Chan, Y.-C., M. Carles, N. J. Sucher, M. Wong, and Y. Zohar, 2003, J. Micromech. Microeng. **13**, 914.
Chan, Y. C., Y.-K. Lee, and Y. Zohar, 2006, J. Micromech. Microeng. **16**, 699.
Chan, Y. C., Y. Zohar, and Y.-K. Lee, 2009, Electrophoresis **30**, 3242.
Chen, Y.-L., M. D. Graham, J. J. de Pablo, G. C. Randall, M. Gupta, and P. S. Doyle, 2004, Phys. Rev. E **70**, 060901(R).
Chen, Z., and F. A. Escabedo, 2003, Mol. Simul. **29**, 417.
Chiesl, T. N., K. W. Putz, M. Babu, P. Mathias, K. A. Shaikh, E. D. Goluch, C. Liu, and A. E. Barron, 2006, Anal. Chem. **78**, 4409.
Cho, J., S. Kumar, and K. D. Dorfman, 2010, Electrophoresis **31**, 860.
Chou, C. F., O. Bakajin, S. W. P. Turner, T. A. J. Duke, S. S. Chan, E. C. Cox, H. G. Craighead, and R. H. Austin, 1999, Proc. Natl. Acad. Sci. U.S.A. **96**, 13762.
Chou, S.-Y., P. R. Krauss, and P. J. Renstrom, 1996, Science **272**, 85.
Chu, G., D. Vollrath, and R. W. Davis, 1986, Science **234**, 1582.
Clark, S. M., E. Lai, B. W. Birren, and L. Hood, 1988, Science **241**, 1203.
Cross, J. D., E. A. Strychalski, and H. G. Craighead, 2007, J. Appl. Phys. **102**, 024701.
Cummings, E. B., S. K. Griffiths, R. H. Nilson, and P. H. Paul, 2000, Anal. Chem. **72**, 2526.
Davies, K., 2001, *Cracking the Genome: Inside the Race to Unlock Human DNA* (Free, New York).
de Carmejane, O., Y. Yamaguchi, T. I. Todorov, and M. D. Morris, 2001, Electrophoresis **22**, 2433.
de Gennes, P. G., 1971, J. Chem. Phys. **55**, 572.
de Pablo, J. J., M. Laso, and U. W. Suter, 1992, J. Chem. Phys. **96**, 6157.
Deutsch, J. M., 1987, Phys. Rev. Lett. **59**, 1255.
Deutsch, J. M., 1988, Science **240**, 922.
Deutsch, J. M., 1989, J. Chem. Phys. **90**, 7436.
Deutsch, J. M., and T. L. Madden, 1989, J. Chem. Phys. **90**, 2476.
Dobrynin, A., 2005, Macromolecules **38**, 9304.
Doi, M., 1996, *Introduction to Polymer Physics* (Clarendon, Oxford).
Doi, M., and S. F. Edwards, 1988, *The Theory of Polymer Dynamics* (Clarendon, Oxford).
Doi, M., T. Kobayashi, Y. Makino, M. Ogawa, G. W. Slater, and J. Noolandi, 1988, Phys. Rev. Lett. **61**, 1893.
Dorfman, K. D., 2003, J. Chem. Phys. **118**, 8428.
Dorfman, K. D., 2006, Phys. Rev. E **73**, 061922.
Dorfman, K. D., 2008, Phys. Rev. E **77**, 019901(E).
Dorfman, K. D., and H. Brenner, 2002, Phys. Rev. E **65**, 052103.
Dorfman, K. D., G. W. Slater, and M. G. Gauthier, 2003, J. Chem. Phys. **119**, 6979.
Dorfman, K. D., and J.-L. Viovy, 2004, Phys. Rev. E **69**, 011901.
Doyle, P. S., J. Bibette, A. Bancaud, and J.-L. Viovy, 2002, Science **295**, 2237.
Duffy, D. C., J. C. McDonald, O. J. A. Schueller, and G. M. Whitesides, 1998, Anal. Chem. **70**, 4974.
Duke, T., J.-L. Viovy, and A. N. Semenov, 1994, Biopolymers **34**, 239.
Duke, T. A. J., 1990, J. Chem. Phys. **93**, 9055.
Duke, T. A. J., and R. H. Austin, 1998, Phys. Rev. Lett. **80**, 1552.
Duke, T. A. J., R. H. Austin, E. C. Cox, and S. S. Chan, 1996, Electrophoresis **17**, 1075.
Duke, T. A. J., A. N. Semenov, and J.-L. Viovy, 1992, Phys. Rev. Lett. **69**, 3260.
Duke, T. A. J., and J.-L. Viovy, 1992a, J. Chem. Phys. **96**, 8552.
Duke, T. A. J., and J.-L. Viovy, 1992b, Phys. Rev. Lett. **68**, 542.
Duong, T. T., G. Kim, R. Ros, M. Streek, F. Schmid, J. Brugger, D. Anselmetti, and A. Ros, 2003, Microelectron. Eng. **67-68**, 905.
Ertaş, D., 1998, Phys. Rev. Lett. **80**, 1548.
Fangman, W. L., 1978, Nucleic Acids Res. **5**, 653.
Flint, D. H., and R. E. Harrington, 1972, Biochemistry **11**, 4858.
Forster, R. E., D. G. Hert, T. N. Chiesl, C. P. Fredlake, and A. E. Barron, 2009, Electrophoresis **30**, 2014.
Frank, S., and R. G. Winkler, 2009, J. Chem. Phys. **131**, 234905.
Fu, J., P. Mao, and J. Han, 2005, Appl. Phys. Lett. **87**, 263902.
Fu, J., R. B. Schoch, A. L. Stevens, S. R. Tannenbaum, and J. Han, 2007, Nat. Nanotechnol. **2**, 121.
Fu, J., J. Yoo, and J. Han, 2006, Phys. Rev. Lett. **97**, 018103.
Gauthier, M. G., and G. W. Slater, 2002, J. Chem. Phys. **117**, 6745.
Gauthier, M. G., and G. W. Slater, 2003, Electrophoresis **24**, 441.
Gauthier, M. G., and G. W. Slater, 2008, J. Chem. Phys. **128**, 065103.
Gauthier, M. G., G. W. Slater, and K. D. Dorfman, 2004, Eur. Phys. J. E **15**, 71.
Giddings, J. C., E. Kucera, C. P. Russell, and M. N. Myers,

1968, J. Phys. Chem. **72**, 4397.
Grass, K., and C. Holm, 2010, Faraday Discuss. **144**, 57.
Gunther, K., M. Mertig, and R. Seidel, 2010, Nucleic Acids Res. (to be published).
Gurrieri, S., E. Rizzarelli, D. Beach, and C. Bustamante, 1990, Biochemistry **29**, 3396.
Gurrieri, S., S. K. Wells, I. D. Johnson, and C. Bustamante, 1997, Anal. Biochem. **249**, 44.
Haghgooie, R., C. Li, and P. S. Doyle, 2006, Langmuir **22**, 3601.
Han, J., and H. G. Craighead, 1999, J. Vac. Sci. Technol. A **17**, 2142.
Han, J., and H. G. Craighead, 2000, Science **288**, 1026.
Han, J., and H. G. Craighead, 2002, Anal. Chem. **74**, 394.
Han, J., S. W. Turner, and H. G. Craighead, 1999, Phys. Rev. Lett. **83**, 1688.
Harrison, D. J., P. G. Glavina, and A. Manz, 1993, Sens. Actuators B **10**, 107.
Heller, C., T. Duke, and J.-L. Viovy, 1994, Biopolymers **34**, 249.
Hjertén, S., 1985, J. Chromatogr. A **347**, 191.
Holleran, S. P., and R. G. Larson, 2008, Macromolecules **41**, 5042.
Hsieh, S.-F., C.-P. Chang, Y.-J. Juang, and H.-H. Wei, 2008, Appl. Phys. Lett. **93**, 084103.
Hsieh, S.-F., and H.-H. Wei, 2009, Phys. Rev. E **79**, 021901.
Huang, L. R., E. C. Cox, R. H. Austin, and J. C. Sturm, 2003, Anal. Chem. **75**, 6963.
Huang, L. R., E. C. Cox, R. H. Austin, and J. C. Sturm, 2004, Science **304**, 987.
Huang, L. R., P. Silberzan, J. O. Tegenfeldt, E. C. Cox, J. C. Sturm, R. H. Austin, and H. G. Craighead, 2002, Phys. Rev. Lett. **89**, 178301.
Huang, L. R., J. O. Tegenfeldt, J. J. Kraeft, J. C. Sturm, R. H. Austin, and E. C. Cox, 2002, Nat. Biotechnol. **20**, 1048.
Inatomi, K., S. Izuo, S. S. Lee, H. Ohji, and S. Shiono, 2003, Microelectron. Eng. **70**, 13.
Jacobson, S. C., R. Hergenroder, L. B. Koutney, R. J. Warmack, and J. M. Ramsey, 1994, Anal. Chem. **66**, 1107.
Kaji, N., A. Oki, R. Ogawa, Y. Takamura, T. Nishimoto, H. Nakanishi, Y. Horiike, M. Tokeshi, and Y. Baba, 2007, Isr. J. Chem. **47**, 161.
Kaji, N., Y. Tezuka, Y. Takamura, M. Ueda, T. Nishimoto, H. Nakanishi, Y. Horiike, and Y. Baba, 2004, Anal. Chem. **76**, 15.
Kasianowicz, J. J., E. Brandin, D. Branton, and D. W. Deamer, 1996, Proc. Natl. Acad. Sci. U.S.A. **93**, 13770.
Kenward, M., and G. W. Slater, 2004, Eur. Phys. J. E **14**, 55.
Kenward, M., and G. W. Slater, 2006, Eur. Phys. J. E **20**, 125.
Kim, J. M., and P. S. Doyle, 2006, J. Chem. Phys. **125**, 074906.
Kim, J. M., and P. S. Doyle, 2007, Macromolecules **40**, 9151.
Kirby, B. J., and E. F. Hasselbrink, Jr., 2004a, Electrophoresis **25**, 187.
Kirby, B. J., and E. F. Hasselbrink, Jr., 2004b, Electrophoresis **25**, 203.
Klotz, L. C., and B. H. Zimm, 1972, Macromolecules **5**, 471.
Kramers, H. A., 1940, Physica **7**, 284.
Kuo, C.-W., K. H. Wei, C.-H. Lin, J.-Y. Shiu, and P. Chen, 2008, Electrophoresis **29**, 2931.
Laachi, N., J. Cho, and K. D. Dorfman, 2009a, Phys. Rev. E **79**, 031928.
Laachi, N., J. Cho, and K. D. Dorfman, 2009b, Phys. Rev. E **80**, 019903(E).
Laachi, N., C. Declet, C. Matson, and K. D. Dorfman, 2007, Phys. Rev. Lett. **98**, 098106.
Labrie, J., J.-F. Mercier, and G. W. Slater, 2000, Electrophoresis **21**, 823.
Lalande, M., J. Noolandi, C. Turmel, R. Brousseau, J. Rousseau, and G. W. Slater, 1988, Nucleic Acids Res. **16**, 5427.
Lalande, M., J. Noolandi, C. Turmel, J. Rousseau, and G. W. Slater, 1987, Proc. Natl. Acad. Sci. U.S.A. **84**, 8011.
Lerman, L. S., and H. L. Frisch, 1982, Biopolymers **21**, 995.
Levene, S. D., and B. H. Zimm, 1987, Proc. Natl. Acad. Sci. U.S.A. **84**, 4054.
Li, Z., and G. Drazer, 2007, Phys. Rev. Lett. **98**, 050602.
Li, Z. R., G. R. Liu, Y. Z. Chen, J.-S. Wang, H. Bow, Y. Cheng, and J. Han, 2008, Electrophoresis **29**, 329.
Liu, J., E. M. Lawrence, A. Wu, M. L. Ivey, G. A. Flores, K. Javier, J. Bibette, and J. Richard, 1995, Phys. Rev. Lett. **74**, 2828.
Liu, L., P. Li, and S. A. Asher, 1999a, J. Am. Chem. Soc. **121**, 4040.
Liu, L., P. Li, and S. A. Asher, 1999b, Nature (London) **397**, 141.
Long, D., and A. Ajdari, 2001, Eur. Phys. J. E **4**, 29.
Long, D., H. A. Stone, and A. Ajdari, 1999, J. Colloid Interface Sci. **212**, 338.
Long, D., J.-L. Viovy, and A. Ajdari, 1996, Phys. Rev. Lett. **76**, 3858.
Lumpkin, O. J., P. Déjardin, and B. H. Zimm, 1985, Biopolymers **24**, 1573.
Lumpkin, O. J., and B. H. Zimm, 1982, Biopolymers **21**, 2315.
Magda, J. J., R. G. Larson, and M. E. Mackay, 1988, J. Chem. Phys. **89**, 2504.
Manning, G. S., 1969, J. Chem. Phys. **51**, 924.
Manning, G. S., 1978, Q. Rev. Biophys. **11**, 179.
Manning, G. S., 1981, J. Phys. Chem. **85**, 1506.
Manz, A., D. J. Harrison, E. M. J. Verpoorte, J. C. Fettinger, A. Paulus, H. Ludi, and H. M. Widmer, 1992, J. Chromatogr. A **593**, 253.
Mao, P., and J. Han, 2009, Lab Chip **9**, 586.
Marko, J. F., and E. D. Siggia, 1995, Macromolecules **28**, 8759.
Masubuchi, Y., H. Oana, T. Akiyama, M. Matsumoto, and M. Doi, 1995, J. Phys. Soc. Jpn. **64**, 1412.
Mathé, J., J. M. di Meglio, and B. Tinland, 2007, J. Colloid Interface Sci. **316**, 831.
Mayer, P., G. W. Slater, and G. Drouin, 1993, Appl. Theor Electrophor **3**, 147.
Meistermann, L., and B. Tinland, 2000, Phys. Rev. E **62**, 4014.
Mercier, J.-F., and G. W. Slater, 1998, Electrophoresis **19**, 1560.
Mercier, J.-F., and G. W. Slater, 2001, Macromolecules **34**, 3437.
Mercier, J.-F., F. Tessier, and G. W. Slater, 2001, Electrophoresis **22**, 2631.
Milne-Thomson, L. M., 1960, *Theoretical Hydrodynamics* (Macmillan, New York).
Minc, N., 2005, Ph.D. thesis (Universite Paris VI, Paris, France).
Minc, N., P. Bokov, K. B. Zeldovich, C. Fütterer, J.-L. Viovy, and K. D. Dorfman, 2005, Electrophoresis **26**, 362.
Minc, N., C. Fütterer, K. D. Dorfman, A. Bancaud, C. Gosse, C. Goubault, and J.-L. Viovy, 2004, Anal. Chem. **76**, 3770.
Minc, N., J.-L. Viovy, and K. D. Dorfman, 2005, Phys. Rev. Lett. **94**, 198105.
Mitnik, L., C. Heller, J. Prost, and J.-L. Viovy, 1995, Science **267**, 219.
Mohan, A., and P. S. Doyle, 2007a, Phys. Rev. E **76**, 040903(R).
Mohan, A., and P. S. Doyle, 2007b, Macromolecules **40**, 8794.

Morra, M., E. Occhiello, R. Marola, F. Garbassi, P. Humphrey, and D. Johnson, 1990, J. Colloid Interface Sci. **137**, 11.
Morris, C. J. O. R., 1967, Protides Biol. Fluids **14**, 543.
Morrison, F. A., Jr., 1970, J. Colloid Interface Sci. **34**, 210.
Mukhopadhyay, R., 2009, Anal. Chem. **81**, 4169.
Muthukumar, M., 1999, J. Chem. Phys. **111**, 10371.
Muthukumar, M., and A. Baumgartner, 1989a, Macromolecules **22**, 1941.
Muthukumar, M., and A. Baumgartner, 1989b, Macromolecules **22**, 1937.
Nixon, G. I., and G. W. Slater, 1994, Phys. Rev. E **50**, 5033.
Nkodo, A. E., J. M. Garnier, B. Tinland, H. Ren, C. Desruisseaux, L. C. McCormick, G. Drouin, and G. W. Slater, 2001, Electrophoresis **22**, 2424.
Noolandi, J., J. Rousseau, G. W. Slater, C. Turmel, and M. Lalande, 1987, Phys. Rev. Lett. **58**, 2428.
Noolandi, J., G. W. Slater, H. A. Lim, and J.-L. Viovy, 1989, Science **243**, 1456.
Norris, D. J., E. G. Arlinghaus, L. Meng, R. Heiny, and L. E. Scriven, 2004, Adv. Mater. **16**, 1393.
Nykypanchuk, D., H. H. Strey, and D. A. Hoagland, 2002, Science **297**, 987.
Oana, H., Y. Masubuchi, M. Matsumoto, M. Doi, Y. Matsuzawa, and K. Toshikawa, 1994, Macromolecules **27**, 6061.
Odijk, T., 1977, J. Polym. Sci., Polym. Phys. Ed. **15**, 477.
Odijk, T., 1983, Macromolecules **16**, 1340.
Odijk, T., 2008, Phys. Rev. E **77**, 060901(R).
Ogawa, R., N. Kaji, S. Hashioka, Y. Baba, and Y. Horiike, 2007, Jpn. J. Appl. Phys., Part 1 **46**, 2771.
Ogston, A. G., 1958, Trans. Faraday Soc. **54**, 1754.
Olivera, B. M., P. Baine, and N. Davidson, 1964, Biopolymers **2**, 245.
Olson, D. J., J. M. Johnson, P. D. Patel, E. S. G. Shaqfeh, S. G. Boxer, and G. G. Fuller, 2001, Langmuir **17**, 7396.
Ou, J., S. J. Carpenter, and K. D. Dorfman, 2010, Biomicrofluidics **4**, 013203.
Ou, J., J. Cho, D. W. Olson, and K. D. Dorfman, 2009, Phys. Rev. E **79**, 061904.
Panwar, A. S., and S. Kumar, 2006, Macromolecules **39**, 1279.
Parikesit, G. O. F., A. P. Markesteijn, O. M. Piciu, A. Bossche, J. Westerweel, I. T. Young, and Y. Garini, 2008, Biomicrofluidics **2**, 024103.
Patel, P. D., and E. S. G. Shaqfeh, 2003, J. Chem. Phys. **118**, 2941.
Pennathur, S., F. Baldessari, J. G. Santiago, M. G. Kattah, J. B. Steinman, and P. J. Utz, 2007, Anal. Chem. **79**, 8316.
Perkins, T. T., D. E. Smith, R. G. Larson, and S. Chu, 1995, Science **268**, 83.
Popelka, S., Z. Kabatek, J.-L. Viovy, and B. Gas, 1999, J. Chromatogr. A **838**, 45.
Randall, G. C., and P. S. Doyle, 2004, Phys. Rev. Lett. **93**, 058102.
Randall, G. C., and P. S. Doyle, 2005a, Macromolecules **38**, 2410.
Randall, G. C., and P. S. Doyle, 2005b, Proc. Natl. Acad. Sci. U.S.A. **102**, 10813.
Randall, G. C., and P. S. Doyle, 2006, Macromolecules **39**, 7734.
Redner, S., 2001, *A Guide to First-Passage Processes* (Cambridge University Press, Cambridge).
Rodbard, D., and A. Chrambach, 1970, Proc. Natl. Acad. Sci. U.S.A. **65**, 970.
Rouse, P. E., 1953, J. Chem. Phys. **21**, 1272.
Rousseau, J., G. Drouin, and G. W. Slater, 1997, Phys. Rev. Lett. **79**, 1945.
Russell, W. B., D. A. Saville, and W. R. Schowalter, 1989, *Colloidal Dispersions* (Cambridge University Press, Cambridge).
Rye, H. S., S. Yue, D. E. Wemmer, M. A. Quesada, R. P. Haugland, R. A. Mathies, and A. N. Glazer, 1992, Nucleic Acids Res. **20**, 2803.
Sakaue, T., 2006, Eur. Phys. J. E **19**, 477.
Saliba, A. E., C. Gosse, N. Minc, C. Roblin, K. D. Dorfman, and J.-L. Viovy, 2006, in *Proceedings of the 10th International Conference on Miniaturized Systems for Chemistry and Life Sciences*, edited by T. Kitamori, H. Fujita, and S. Hasebe (Transducer Research Foundation, San Diego), pp. 386–388.
Salieb-Beugelaar, G. B., J. Teapal, J. van Nieuwkasteele, D. Wijnperlé, J. O. Tegenfeldt, F. Lisdat, A. van den Berg, and J. C. T. Eijkel, 2008, Nano Lett. **8**, 1785.
Saville, P. M., and E. M. Sevick, 1999, Macromolecules **32**, 892.
Scher, H., and M. Lax, 1973, Phys. Rev. B **7**, 4491.
Schwartz, D. C., and C. Cantor, 1984, Cell **37**, 67.
Schwartz, D. C., and M. Koval, 1989, Nature (London) **338**, 520.
Schwinefus, J. J., R. W. Hammond, H. Oana, S.-C. Wang, O. de Carmejane, J. Bonadio, and M. D. Morris, 1999, Macromolecules **32**, 4625.
Sebastian, K. L., and A. K. R. Paul, 2000, Phys. Rev. E **62**, 927.
Semenov, A. N., T. A. J. Duke, and J.-L. Viovy, 1995, Phys. Rev. E **51**, 1520.
Semenov, A. N., and J.-F. Joanny, 1997, Phys. Rev. E **55**, 789.
Serwer, P., 1981, Anal. Biochem. **112**, 351.
Sevick, E. M., and D. R. M. Williams, 1994, Phys. Rev. E **50**, R3357.
Sevick, E. M., and D. R. M. Williams, 1996, Phys. Rev. Lett. **76**, 2595.
Shaffer, E. O., II, and M. O. de la Cruz, 1989, Macromolecules **22**, 1351.
Shi, J., A. P. Fang, L. Malaquin, A. Pepin, D. Decanini, J.-L. Viovy, and Y. Chen, 2007, Appl. Phys. Lett. **91**, 153114.
Shi, X., R. W. Hammond, and M. D. Morris, 1995, Anal. Chem. **67**, 1132.
Shiu, J.-Y., W.-T. Whang, and P. Chen, 2008, J. Chromatogr. A **1206**, 72.
Sischka, A., K. Toensing, R. Eckel, S. D. Wilking, N. Sewald, R. Ros, and D. Anselmetti, 2005, Biophys. J. **88**, 404.
Skolnick, J., and M. Fixman, 1977, Macromolecules **10**, 944.
Slater, G. W., 2009, Electrophoresis **30**, S181.
Slater, G. W., and H. L. Guo, 1996a, Electrophoresis **17**, 977.
Slater, G. W., and H. L. Guo, 1996b, Electrophoresis **17**, 1407.
Slater, G. W., H. L. Guo, and G. I. Nixon, 1997, Phys. Rev. Lett. **78**, 1170.
Slater, G. W., C. Holm, M. V. Chubynsky, H. W. de Haan, A. Dubé, K. Grass, O. A. Hickey, C. Kingsburry, D. Sean, T. N. Shendruk, and L. Zhan, 2009, Electrophoresis **30**, 792.
Slater, G. W., and J. Noolandi, 1985a, Phys. Rev. Lett. **55**, 1579.
Slater, G. W., and J. Noolandi, 1985b, Biopolymers **24**, 2181.
Slater, G. W., and J. Noolandi, 1986, Biopolymers **25**, 431.
Slater, G. W., and J. Noolandi, 1989, Electrophoresis **10**, 413.
Slater, G. W., J. Rousseau, and J. Noolandi, 1987, Biopolymers **26**, 863.
Slater, G. W., and J. R. Treurniet, 1997, J. Chromatogr. A **772**, 39.
Smisek, D. L., and D. A. Hoagland, 1990, Science **248**, 1221.
Smith, D. E., T. T. Perkins, and S. Chu, 1996, Macromolecules **29**, 1372.

Smith, S. B., P. K. Aldridge, and J. B. Callis, 1989, Science **243**, 203.
Smith, S. B., L. Finzi, and C. Bustamante, 1992, Science **258**, 1122.
Song, L., and M. Maestre, 1991, J. Biomol. Struct. Dyn. **9**, 87.
Southern, E., R. Anand, W. R. A. Brown, and D. S. Fletcher, 1987, Nucleic Acids Res. **15**, 5925.
Stellwagen, E., Y. Lu, and N. C. Stellwagen, 2003, Biochemistry **42**, 11745.
Stellwagen, E., and N. C. Stellwagen, 2002, Electrophoresis **23**, 1935.
Stellwagen, N. C., C. Gelfi, and P. G. Righetti, 1997, Biopolymers **42**, 687.
Streek, M., F. Schmid, T. T. Duong, D. Anselmetti, and A. Ros, 2005, Phys. Rev. E **71**, 011905.
Streek, M., F. Schmid, T. T. Duong, and A. Ros, 2004, J. Biotechnol. **112**, 79.
Strychalski, E. A., H. W. Lau, and L. A. Archer, 2009, J. Appl. Phys. **106**, 024915.
Sung, W., and P. J. Park, 1996, Phys. Rev. Lett. **77**, 783.
Tessier, F., J. Labrie, and G. W. Slater, 2002, Macromolecules **35**, 4791.
Tessier, F., and G. W. Slater, 2002, Appl. Phys. A: Mater. Sci. Process. **75**, 285.
Turmel, C., E. Brassard, G. W. Slater, and J. Noolandi, 1990, Nucleic Acids Res. **18**, 569.
Turner, S. W., A. M. Perez, A. Lopez, and H. G. Craighead, 1998, J. Vac. Sci. Technol. B **16**, 3835.
Turner, S. W. P., M. Cabodi, and H. G. Craighead, 2002, Phys. Rev. Lett. **88**, 128103.
van der Linden, H. J., L. C. Jellema, M. Holwerda, and E. Verpoorte, 2006, Anal. Bioanal. Chem. **385**, 1376.
van Oudenaarden, A., and S. G. Boxer, 1999, Science **285**, 1046.
Verneuil, E., A. Buguin, and P. Silberzan, 2004, Europhys. Lett. **68**, 412.
Viovy, J.-L., 1987, Biopolymers **26**, 1929.
Viovy, J.-L., 1988, Phys. Rev. Lett. **60**, 855.
Viovy, J.-L., 1989, Electrophoresis **10**, 429.
Viovy, J.-L., 2000, Rev. Mod. Phys. **72**, 813.
Volkmuth, W. D., and R. H. Austin, 1992, Nature (London) **358**, 600.
Volkmuth, W. D., T. Duke, M. C. Wu, R. H. Austin, and A. Szabo, 1994, Phys. Rev. Lett. **72**, 2117.
Wong, C. T. A., and M. Muthukumar, 2008, Biophys. J. **95**, 3619.
Yasui, T., N. Kaji, R. Ogawa, S. Hashioka, M. Tokeshi, Y. Horiike, and Y. Baba, 2007, in *Proceedings of the 11th International Conference on Miniaturized Systems for Chemistry and Life Sciences*, edited by J.-L. Viovy, P. Tabeling, S. Descroix, and L. Malaquin (Transducer Research Foundation, San Diego), pp. 1207–1209.
Zeng, Y., and D. J. Harrison, 2006, Electrophoresis **27**, 3747.
Zeng, Y., and D. J. Harrison, 2007, Anal. Chem. **79**, 2289.
Zeng, Y., M. He, and D. J. Harrison, 2008, Angew. Chem., Int. Ed. **47**, 6388.
Zhang, H., and M. J. Wirth, 2005, Anal. Chem. **77**, 1237.
Zhu, H. P., S. M. Clark, S. C. Benson, H. S. Rye, A. N. Glazer, and R. A. Mathies, 1994, Anal. Chem. **66**, 1941.
Zimm, B. H., 1956, J. Chem. Phys. **24**, 269.
Zimm, B. H., 1988, Phys. Rev. Lett. **61**, 2965.
Zimm, B. H., 1991, J. Chem. Phys. **94**, 2187.